Statistical Characterisation of Water Vapour Variability in the Troposphere

a height-resolved analysis using airborne lidar observations and COSMO-DE model simulations

Dissertation
an der Fakultät für Physik
der Ludwig-Maximilians-Universität
München

vorgelegt von
Lucas Fischer
aus Mannheim

München, den 14. August 2013

1. Gutachter: Prof. Dr. G. C. Craig

2. Gutachter: Prof. Dr. M. Rapp

Datum der mündlichen Prüfung: 25.10.2013

Parts of this thesis are contained in:

Fischer, L., C. Kiemle, and G. C. Craig (2012), Height-resolved variability of midlatitude tropospheric water vapor measured by airborne lidar, *G. Res. Lett., 39*, doi:10.1029/2011GL050621.

Fischer, L., G. C. Craig, and C. Kiemle (2013), Horizontal structure function and vertical correlation analysis of mesoscale water vapor variability observed by airborne lidar, *J. Geophys. Res. Atmos., 118*, doi:10.1002/jgrd.50588.

Contents

Zusammenfassung

Wasserdampf in der Troposphäre spielt eine entscheidende Rolle im Klimasystem, zum einen aufgrund seines direkten Einflusses auf den Strahlungshaushalt und zum anderen durch seine Wechselwirkungen mit dynamischen Prozessen, wie z.B. Kumulus Konvektion. Die räumliche Verteilung des Wasserdampfes in der freien Atmosphäre ist dabei sehr komplex aufgrund von Quellen und Senken, sowie aufgrund von konvektiven Wolken, die auf der Kilometerskala bis hin zu Wolkensystemen auf Skalen von 1000 Kilometern und mehr agieren. Ein weiterer Vorgang, der die Verteilung maßgeblich beeinflusst, ist die Advektion bzw. der Transport von Wasserdampf als passiver Tracer außerhalb von konvektiven Einflüssen. Während die großskalige Advektion von Wasserdampf in Wetter- und Klimamodellen gut abgebildet ist, führt das unzureichende Verständnis der kleinskaligen physikalischen Vorgänge des Wasserdampfes in der Troposphäre zu starken Einschränkungen in Modellsimulationen von lokalen Phänomenen (z.B. Wolken, Niederschlag). Dabei kommt insbesondere der Parametrisierung von kleinskaligen Prozessen aufgrund ihrer zeitlichen und räumlichen Variabilität eine immense Bedeutung in Wetter- und Klimamodellen zu. Trotz ihres erheblichen Einflusses sowohl auf die Entwicklung von Wolken als auch auf Niederschlagsprozesse, ist die Wasserdampfvariabilität im Bereich der höchsten Auflösung von Wetter- und Klimamodellen bislang nicht ausreichend präzise untersucht und charakterisiert worden.

In dieser Dissertation wird daher ein großer Datensatz von horizontal und vertikal hoch aufgelösten flugzeuggetragenen Lidarbeobachtungen analysiert, mit dem Ziel, die kleinskalige (< 100 km) Wasserdampfvariabilität statistisch zu charakterisieren. Strukturfunktionen, d.h., statistische Momente basierend auf absoluten räumlichen Inkrementen, werden von der 1. bis zur 5. Ordnung berechnet und hinsichtlich ihres Power-law Verhaltens in einem Skalenbereich von 5 km - 100 km untersucht. Die im Rahmen dieser Arbeit gefundenen Power-law Exponenten bzw. Steigungen der Strukturfunktionen fallen unterschiedlich groß aus, je nachdem, ob die Beobachtungen aus Luftmassen mit konvektiven Wolken stammen oder aus wolkenfreier Luftmasse. Die Ergebnisse sind konsistent hinsichtlich eines nicht-konvektiven Regimes, das von großskaligen advektiven Prozessen dominiert ist. Dies führt zu monofraktalen Skalenabhängigkeitseigenschaften in der Variabilität des Wasserdampffeldes. Im Gegensatz dazu ist das konvektive Regime von starken, lokalen Inputs kleinskaliger Variabilität charakterisiert, die durch konvektive Zirkulationen entstanden sind und zu einer starken Intermittenz beitragen.

Diese aus Lidarbeoachtungen gewonnene Statistik dient zur Validierung des operationellen hochaufgelösten Wettermodells COSMO-DE des Deutschen Wetterdienstes. Basierend auf einer Simulation während der COPS/ETReC Kampagne mit 2.8 km Auflösung, wird mit Hilfe von Strukturfunktionen gezeigt, dass im Modell zwei Regimes vorhanden sind, abhängig von der Luftmasse. Das COSMO-

DE Modell ist somit in der Lage, in teilweise bewölkten und wolkenfreien Gebieten, die Variabilität auf kleinen Skalen gut zu simulieren. Weiter konnte mit Hilfe der Modelldaten gezeigt werden, dass ein Flugabschnitt statistisch ausreicht um die Statistik der Power-law Exponenten abzubilden. Außerdem konnte der lückenlose Modelldatensatz dazu beitragen, den Einfluss von Datenlücken in den Beobachtungen (z.B. Wolken) abzuschätzen. Dieser Fehler liegt in der Größenordnung von wenigen Prozent.

In dieser Arbeit wird gezeigt, dass neuartige flugzeuggetragene Lidarbeoachtungen von Wasserdampf wertvoll sind, um eine höhenaufgelöste statistische Beschreibung der Variabilität basierend auf Strukturfunktionen zu gewinnen. Diese hat, neben der Unterscheidung von physikalischen Prozessen, die zur Wasserdampfverteilung in der Troposphäre führen auch das Potenzial als Basis für stochastische Parametrisierungen zu dienen. Außerdem dient die höhenaufgelöste Statistik aus Lidarbeobachtungen als Realitätscheck des hochaufgelösten numerischen Wettermodells COSMO-DE.

Abstract

Tropospheric water vapour plays an important role in thermodynamic and radiative processes which have an immediate impact on the weather and climate system. However, the processes that determine the distribution of water vapour remain poorly understood. The complexity arises out of a range of source and sink processes from convective clouds on the kilometre scale to cloud systems associated with motions on scales of a thousand or more kilometres, as well as advection of water vapour as a passive tracer outside of clouds. While large-scale advection of water vapour is well represented in general circulation models, the simulation of small-scale moist processes that are of central importance to the representation of clouds are heavily dependent on parameterisations. However, observations as well as processes that determine the distribution of the water vapour field are insufficiently explored, leading to constrained parameterisations and therefore contributing significantly to the uncertainty of numerical weather and climate predictions. Hence, a more accurate description of the inhomogeneous water vapour field based on high-resolution observations is required.

This thesis investigates a comprehensive data set of two-dimensional airborne water vapour observations in the free troposphere collected by a Differential Absorption Lidar (DIAL) in order to gain a height-resolved statistical characterisation of the inhomogeneous water vapour field. Structure functions, i.e., statistical moments up to the fifth order of absolute increments over a range of scales, are investigated and power-law behaviour or scale dependence is identified over horizontal distances from about 5 km to 100 km. The slope of the power-law fit, the so-called scaling exponent, is found to take different values, depending on whether or not the observations were taken in an air mass where convective clouds were present. These results are consistent with a non-convective regime that is dominated by large-scale advective processes, leading to monofractal scaling, but strong localised input of small-scale variability by convective circulations leading to intermittent fields.

Further, the observed power-law statistics are used to evaluate the high-resolution numerical weather prediction model COSMO-DE of the German weather service with regard to the small-scale water vapour variability. The results of the scaling exponent analysis of cloud-free and partly cloudy scenes suggest, that the small-scale variance is modeled quite well in comparison with the lidar observations. By using the advantage of the model simulation where data is not limited to a specific flight path, the influence of sampling limitation is estimated and is found to be not significant. Further, the simulation provides humidity data in and beneath clouds which allows for an estimation of the uncertainty of data gaps in the lidar observations due to optically thick clouds. The error is identified to be in a range of only few percents.

This thesis demonstrates that airborne DIAL observations are useful to build up

a height-resolved statistical characterisation of tropospheric water vapour variability that allows to distinguish physical mechansims that are responsible for the water vapour distribution, to get new insights into stochastic parameterisations and further to use the structure function method as a suitable reality check of the numerical weather model COSMO-DE.

Chapter 1

Introduction

The spatio-temporal variability of the Earth's weather events ranges over many orders of magnitude and poses a significant challenge to numerical weather prediction (NWP) models and global climate models (GCM) as in any computationally tractable model the range of scales that can be explicitly resolved is limited. Unresolved small-scale processes such as cumulus clouds, convection, turbulence and radiation may, however, be very important in producing an accurate weather forecast (Stevens and Bony, 2013a). Therefore, processes smaller than the model resolution (also called subgrid-scale processes) are parameterised, i.e., the effects of physical processes that cannot be represented directly in a model are statistically or algorithmically related to model variables (Warner, 2011). In principle, parameterisations are useful in order to avoid high computational costs for directly represented small-scale physical processes and also in order to represent processes that are insufficiently explored. Based on the fact that separation between resolved and parameterised phenomena depends highly on the actual atmospheric state, the contribution of parameterisations to an accurate weather or climate simulation is afflicted with a large uncertainty (Stensrud, 2007).

As water vapour plays a key role on several subgrid-scale processes (e.g., convection, clouds, radiation) it represents a key factor for parameterisation of these processes in weather and climate models. Despite large progress in this research area within the last decades, the complex dynamics of the tropospheric moisture field are still not fully explored owing mainly to the fact that the water vapour distribution is controlled by complex atmospheric motions varying over a wide range of scales (Schneider et al., 2010; Sherwood et al., 2010).

Current NWP models resolve atmospheric processes at a scale of few kilometres, i.e., large structures of convection can be resolved but single updrafts and

downdrafts are still to be parameterised (Doms et al, 2011; Bryan et al., 2003). In principle, the simulation of clouds and precipitation is highly dependent on the coupling between unresolved boundary layer or shallow convective processes with larger scale convective circulations. Linking parameterised sub-grid scale processes with resolved larger scale processes in simulations carries a large potential error source that is affecting the forcast skill of NWP models.

State of the art GCMs have resolutions larger than 50 km, i.e., effects due to clouds are approximated over a grid box even though clouds exhibit variability at scales much smaller than GCM resolutions (see Figure 1.1). Current parameterisations of clouds are responsible for a major source of uncertainty in climate models, especially concerning the cloud feedbacks (Soden and Held, 2006; Webb et al., 2006). Due to the fact that clouds are reflecting solar radiation back to space and trapping infrared radiation emitted by the surface, even small differences in modelling cloud feedbacks can have strong influence on climate simulations (e.g., Zhang, 2004; Yokohata et al., 2005).

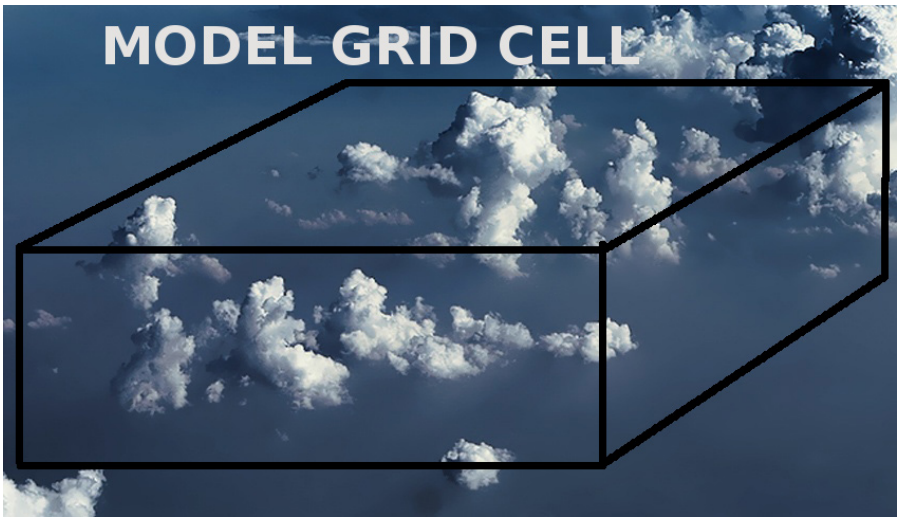

Figure 1.1: Exemplary NWP model or GCM grid box (solid black lines) which demonstrates the subgrid-scale variability of clouds and especially the moist processes within them (both horizontally and vertically)

Cloud properties are strongly dependent on the humidity of the ambient air, which in nature varies significantly over distances corresponding to a model grid box. Since this dependence is strongly nonlinear over distances corresponding to a model grid box (see also Figure 1.1), a better understanding of atmospheric motions and variability on scales around the model resolution is inalienable to improve existing parameterisations. The design and testing of such schemes de-

pends on an accurate characterisation of small-scale water vapour variability in nature. This thesis presents new insights based on a statistical characterisation of water vapour variability on scales around the resolution of NWP and climate models.

Relevance of improving the characterisation of small-scale water vapour variability

A variety of studies investigated the influence of small-scale water vapour variability on convection, clouds and precipitation, and highlight its importance for weather and climate prediction models:

A correct simulation of convective and severe precipitation events depends strongly on an accurate depiction of the humidity distribution throughout the troposphere (Andersson et al., 2007; Ebert et al., 2003). Indeed, it is known that water vapour in the troposphere plays a significant role in determining the location and structure of clouds and precipitation (Sherwood et al., 2010; Wang et al., 2010). Several studies have shown, that the lack of understanding of the small-scale dynamical effects (e.g., heating and cooling) of water vapour throughout the troposphere leads to strong limitations in predicting localised phenomena in weather and climate models (Cusack et al., 1999; Tompkins, 2002). It is known, for example, that forecasting the initiation of deep convection in a cloud-resolving model is highly dependent on high-quality water vapour observations (e.g. Kottmeier et al., 2008). Furthermore, Tompkins and Berner (2008) and Zhang et al. (2003) have shown that the lack of knowledge of water vapour fluctuations on subgrid scales leads to errors in the modeling of deep convection.

Parameterisations of small-scale moist processes in current GCMs are represented by spatially averaged or constant values of the subgrid scale convective elements. However, many of these 'constants' are in fact dependent on the subgrid-scale variability of moisture within a grid box, and will vary with the local synoptic conditions (see Figure 1.1). Therefore, an important pre-requisite for improving the representation of moist processes in weather and climate models is an accurate characterisation of tropospheric small-scale water vapour variability, including subgrid-scale humidity fluctuations, which is presented in this thesis.

Status quo of the literature on observed water vapour scale dependencies and their limitations

In general, the problem of parameterisations is one of scale dependence, in that

it seeks to couple processes acting on scales that cannot be directly resolved by GCMs or NWP models to large-scale motions. The power spectrum or structure function methods are often used to connect small-scale variability to large-scale variability. Numerous studies of atmospheric wind, energy and temperature have presented observations of the scale dependence, computed with the Fourier power spectrum or with the second-order structure function (e.g., Nastrom and Gage, 1985; Lu and Koch, 2008). These methods have been proven extremely useful to evaluate model simulations (Skamarock, 2004; Hamilton et al., 2008) and to constrain cloud parameterisation (Cusack et al., 1999) by expressing a variance scale-dependence of dynamical tracers in an atmospheric flow. Further, the spectral information can be used for the development of cascade-based stochastic down-scaling methodologies (Harris et al., 2001; Rebora et al., 2006).

Despite the relevance of water vapour variability on the dynamics of clouds and precipitation, only few observational studies have been made to characterise the scaling properties of water vapour throughout the troposphere. This is not surprising as collecting water vapour measurements which could be helpful to characterise spatial variability in the free tropospere is quite complex. Until now, scaling properties gained from only two measuring systems have been presented: aircraft in-situ and satellite systems. Aircraft in-situ provides high resolution measurements at one height but is limited in measuring height variability of the water vapour field. In contrast, satellite measurements provide globally, horizontal and vertical resolved data but the resolution is limited to 3 km in the vertical and 50 km in the horizontal, i.e., the resolution is also coarser than the grid scale of most weather and climate models for which one would like to have data.

In the late 1980's, Nastrom et al. (1986) computed power spectra of water vapour mixing ratio airborne insitu measurements at heights from 9 km to 14 km. They found a range of power-law exponent values β from $\beta = 5/3$ (the predicted value for a passive tracer in three-dimensional turbulence) up to $\beta = 2$ from 150 km to 1500 km in horizontal range. In the 1990's, Tjemkes and Visser (1994) analysed satellite measurements of specific humidity and found exponents similar to those of Nastrom and Gage. Cho et al. (1999 and 2000) enlarged the set of mesoscale scaling exponents (6 km - 60 km and 0.05 km - 100 km) in two aircraft studies with in situ measurements, suggesting that the values of the exponents differ between the boundary layer, the tropical free troposphere and the extratropical free troposphere. They found values from $\beta = 5/3$ up to values

larger than $\beta = 2$. Within the last four years, three studies have been published where satellite data for water vapour from AIRS (Atmospheric Infrared Sounder) was analysed (Kahn and Teixeira, 2009; Kahn et al., 2011; Pressel and Collins, 2012). In particular, Pressel and Collins (2012) have shown the presence of two distinct scaling regimes, one which characterises the spatial variability of water vapour in the boundary layer and one in the free troposphere. Boundary layer exponents in the horizontal range from 50 km to 500 km are found to be near $\beta = 5/3$, while free tropospheric scaling exponents are found to be generally greater than $\beta = 2$.

Observed tropospheric water vapour scaling exponents are highly variable over spatial scales and heights. However, no quantitative theory exists about the processes that are responsible for the observed variability. Based on the analysis of a unique height-resolved airborne DIAL (Differential absorption lidar) water vapour data set, this thesis allows new insights into the processes responsible for water vapour variability on small scales. For the first time, scaling exponents on horizontal scales from 5 km up to 100 km and with a vertical resolution of about 150 m are calculated and analysed in order to allow for a better characterisation of the small-scale water vapour field which is necessary for improved parameterisations. A height-resolved scaling law statistic, as it is given for the first time in this thesis, can be of practical use for improving stochastic parameterisations that attempt to explicitly describe water vapour variability around the grid mesh size of GCMs and NWP models.

Small-scale water vapour variance scaling has not been evaluated in regional NWP models to date

The observed scaling laws of kinetic energy and water vapour are further useful to evaluate the skill of atmospheric models by comparing them to scale dependencies of weather and climate models (Skamarock, 2004; Hamilton et al., 2008; Kahn et al., 2011; Bierdel et al., 2012). In terms of kinetic energy, the evaluation is used to gain insights into the model physics and to determine how well the observed scaling regimes are represented. In terms of water vapour, the study of Kahn et al. (2011) is unique with respect to use observational benchmarks of scaling exponents to evaluate global NWP and climate models. They showed, that the spectral slopes of the climate and NWP models are generally too steep on horizontal scales from about 100 km to 500 km, i.e., model simulations tend

to underestimate the small-scale variance of water vapour. While convective processes are acting on scales smaller than the resolution of global NWP and climate models, regional NWP models with horizontal resolution of few kilometres resolve these convective processes for the most part. Thus, the evaluation of high-resolution regional NWP models is required to get an estimation of how well small-scale variance of water vapour is simulated. This thesis investigates for the first time the water vapour variability of a high-resolution regional NWP model by means of observed benchmarks of scaling exponents.

Research objects and modus operandi

This thesis addresses the need for a better characterisation of tropospheric water vapour variability which is linked to complex atmospheric motions (e.g., moist convection, clouds) transporting water vapour throughout the atmosphere. The study profits from the availability of unique height-resolved lidar water vapour observations from several airborne field campaigns performed with a state-of-the-art Differential Absorption Lidar (DIAL). Simulations of the regional COSMO-DE model from the DWD are used to analyse the model's small-scale specific water vapour variability and compare the height-resolved scaling exponent statistics to the observed.

In summary, this thesis is intended to provide an answer to the following scientific questions:

1 **Does the data set of water vapour observations, collected by an unique airborne DIAL, allow for an improvement of the characterisation of small-scale water vapour variability required for improving parameterisations in numerical weather and climate models?**

2 **Does the analysis of height-resolved airborne DIAL data provide any new theoretical insights into the physical mechanisms, responsible for the observed variability of water vapour throughout the troposphere?**

3 **Does the high-resolution regional NWP model COSMO-DE capture the observed small-scale variability?**

This study is part of the DFG Schwerpunktprogramm (SPP) 1294 HALO with the overall goal to investigate cloud and precipitation processes and the transport

and dynamics in the troposphere and lower stratosphere. Therefore, several flight campaigns were planned but due to organisation delay the data set used in this study is provided by three earlier campaigns which took place in 2007 and 2008. The data was collected by the DIAL system onboard the DLR Falcon aircraft. In detail, COPS/ETReC took place in middle Europe during summer 2007, T-IPY was a flight campaign in northern Europe during winter 2008, especially around Spitzbergen, and T-PARC took place around Japan in late summer 2008. The analysis presented here was processed at the Meteorological Institute of the Ludwig-Maximilians-University Munich, located in Germany.

The thesis is structured as follows. **Chapter 2** addresses the significant role of water vapour in the Earth's troposphere. It further emphasises the role of the spatial water vapour distribution in understanding cloud-forming and precipitation processes, specifically considering the complex dynamical effects acting on different ranges of scales. Further, a short overview on water vapour observation methods is presented, followed by a list of findings from observational and modeling water vapour studies concerning the mechanisms responsible for water vapour variability.

Chapter 3 gives a detailed overview on the data and the methodology underlying the following analysis. This includes a description of the general functioning of the lidar system by which the observational data was collected, respectively the model set up of the NWP model COSMO-DE by which the model data was generated. As regards the applied methodology, the structure function method serving as the main analysis tool for the height-resolved water vapour observations and simulations is introduced. Explaining and discussing the physical meaning of structure function scaling exponents of different orders is a further aspect of Chapter 3.

In **Chapter 4**, results of the height-resolved structure function analysis of the water vapour data set collected during the COPS/ETReC field campaign in summer 2007 are shown. Based on the observed vertical variability of scaling exponents, a hypothesis is introduced, assuming that scaling exponents depend on the physical properties of the underlying air mass.

Chapter 5 validates the hypothesis given in Chapter 4 by analysing a larger water vapour data set collected with airborne DIAL, capturing a greater diversity of meteorological and geophysical conditions due to seasonal, latitudinal and height variations.

Based on the observed scaling statistic, presented in Chapter 4 and 5, the high-resolution weather model of the DWD, called COSMO-DE, is evaluated concerning the spatial water vapour variability down to the effective model resolution (≈ 11 km) in **Chapter 6**.

By providing the main conclusions drawn by this thesis and a brief outlook, **Chapter 7** is to synthesise the impact of the findings presented in this thesis on the statistical characterisation of observed and modelled tropospheric small-scale water vapour variability and further to analyse these findings critically within the current state of research.

Chapter 2

The roles of water vapour in the atmosphere

The impact of tropospheric water vapour on weather and climate can not be overstated as it has essential importance for the development of cloud and precipitation processes through latent heat release when it condenses. Furthermore, as a short-lived atmospheric constituent it plays an important role in planetary radiative balance, influences the surface fluxes and interacts with soil moisture via evaporation. Although water vapour is a very small fraction of the atmospheric constituents its dynamical and radiative effects are controversial discussed in literature (e.g., Elliott, 1995; Trenberth et al., 2005; Stevens and Bony, 2013b). Figure 2.1 gives an overview of these various interactions of water vapour including also the chemical processes which are not specified in this thesis. The mechanisms, which couple atmospheric water with circulation on different ranges of scales are not yet fully understood, but there has been considerable progress in recent years in various key issues, driven also by enhanced observing techniques (e.g., satellite or airborne lidar measurements).

The purpose of Section 2.1 is to demonstrate that the tropospheric water vapour distribution is influenced by several non-trivial processes varying over a wide range of spatial scales. Section 2.2 gives a physical background on the water cycle based on the laws of thermodynamics. In detail, the Clausius-Clapeyron relation, which describes the behaviour of humidity phase changes and its temperature dependency in the weather and climate system, is introduced. The effort to improve the understanding of the complex dynamical effects of water vapour in the troposphere has pushed the development of observation techniques. The main observing systems are described in Section 2.3. In Section 2.4, a literature review

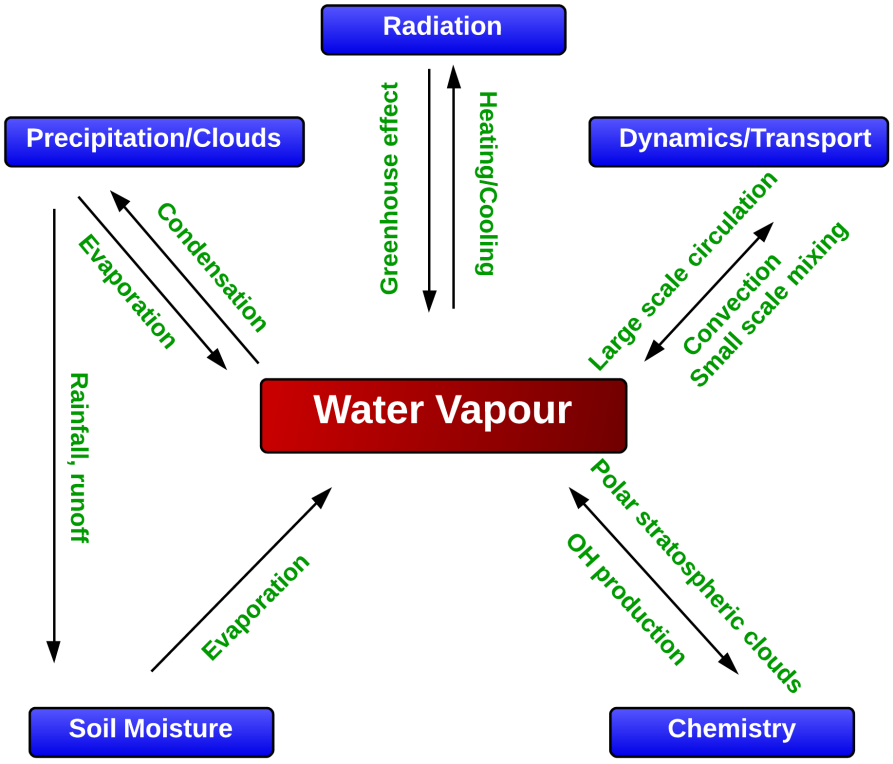

Figure 2.1: The role of water vapour and its interactions in the climate system (adapted from Garand et al. (2002)).

on observational and modeling studies analysing the impact of water vapour on the weather and climate system with a special view on the scale dependence between large-scale circulation and small-scale moist processes, is presented.

2.1 Variability across various spatial scales

The water cycle of the troposphere is characterised by multiscale behaviour, i.e., the water vapor field is affected by processes on many scales. In particular, the dynamical effects are extremely complicated, owing to the fact that the tropospheric water vapour distribution is controlled by both cloud microphysical processes and by large-scale dynamical processes (Emanuel and Pierrehumbert, 1996). Further, it has been identified that even small changes in the amount of water vapour on all scales produce significant changes in cloudiness and radiation (Chahine, 1992).

In the boundary layer the specific humidity distribution is directly related to evaporation from the surface (Schneider et al., 2006) and turbulent mixing plays a key role in the vertical exchange of water vapour and heat. The further water

vapour upward transport is controlled by large-scale eddies, and especially in the tropics by moist convection where vertical motions are driven by latent heat release (Zelinka and Hartmann, 2009). These convective processes act on several spatial scales with narrow convective updrafts and downdrafts, broader mesoscale drafts, and eddies at convective and smaller scales. In principle, convective processes are affected locally by humidity variations, whereas large-scale processes play an essential role in regions sufficiently far away from regions of moist convection or at heights above convection. The large-scale motions are dominated by advection of air by mean circulation and large-scale eddies (Sherwood et al., 2010).

In the large-scale circulation, water vapour generally follows the local velocity of the fluid, i.e., it behaves as a passive tracer which is forced at large scales, dissipated at small scales, and transported by the velocity field. However, water vapour undergoes phase changes in clouds and is added to the atmosphere through surface evaporation respectively removed through precipitation. Sink or source processes, latent heat transport and radiative effects influence the water vapour field in a nonpassive way, i.e., water vapour interacts with atmospheric circulations in a multiplicity of ways. Generally, water vapour acts as a passive tracer on large scales, but is interacting as a nonpassive scalar with atmospheric motions on smaller convective scales. In this thesis, the focus lies on the water vapour variability acting on spatial scales where cumulus clouds are active, i.e. water vapour is not expected to behave as a passive tracer. While the theory of a passive tracer is well explored and represented in models, the non-passive nature of water vapour and its nonlinear coupling with the atmospheric flow at all scales are not yet sufficiently explored.

Summarised, it can be said that the interaction of small-scale moist processes with the large-scale circulation is of high importance in weather and climate simulations but remains still an outstanding question. For a better understanding of how the motions on various spatial scales influence the water distribution, it should therefore be investigated how humidity is affected by the aspects of convection including energetic and dynamic transport processes within the atmosphere (Sherwood et al., 2010).

2.2 Relevance on the weather and climate system

As water cycles through vapour and condensate, the laws of thermodynamics place important constrains on the humidity structure of the atmosphere (Stevens and Bony, 2013b). It is common for all phase changing substances that the maximum partial pressure of water vapour, also known as saturation specific humidity q_s, is a strongly increasing function of temperature which is governed by the Clausius-Clapeyron relation:

$$\frac{dq_s(T)}{dT} = \frac{Lq_s(T)}{R_v T^2}. \tag{2.1}$$

L is the latent heat of the appropriate phase transition and R_v the gas constant for water vapour. Equation 2.1 describes the physical relation that the removal of liquid water to the vapour phase requires the effort of energy at constant pressure. Whenever the specific humidity q exceeds q_s, condensation which is linked to latent heat release occurs. The Clausius-Clapeyron relation provides a powerful constraint on the behaviour of water vapour, inter alia to relate the interaction of saturated water vapour pressure and latent heat transport through condensation and evaporation as well as with dependency of temperature. While this constraint gives only an upper bound on the water content dependent on any temperature, it is not straightforward to get out its implications for weather and climate because water vapour is mostly unsaturated in the atmosphere (Pierrehumbert et al., 2007). Nevertheless, the second thermodynamic law can help to understand weather and climate through water. The dynamical effects of radiation and convection provide a foundation for understanding broad characteristics of the atmospheric circulation, particularly in the tropics, where water is often saturated (Stevens and Bony, 2013b).

Influence on convective processes

Water is unique among atmospheric molecules because it changes phase at terrestrial temperatures (Maurellis and Tennyson, 2003). During moist convective processes which are responsible for cloud-forming mechanisms, water undergoes several phases: gas (vapour), liquid and ice (droplets and ice crystals). The evaporation of liquid water into water vapour needs a lot of energetic input. Once

water vapour condenses to liquid water, it releases that amount of heat into the environment. This property of water makes it an outstanding atmospheric energy transferring constituent.

Among horizontal large-scale advection processes, the small-scale motions often interact with the water vapour field via convection. A process is called convection whenever a parcel rises on itself in an unstable atmosphere. The first law of thermodynamics dictates the changing temperature for adiabatic displacements. When an air parcel is lifted up, it expands and cools at the dry adiabatic temperature lapse rate (-9.8 K/km) and simultaneous its saturation vapour pressure q_s will decrease. If the environmental lapse rate is higher than the adiabatic lapse rate, the parcel continues to rise until it reaches its dew point temperature and condensation occurs, i.e., a cloud is forming. As long as the parcel is warmer than the environment, air continues to rise and therefore water vapour continues to condense. The process steadily releases latent heat which reduces the adiabatic cooling of the parcel. Therefore, moist convection strongly contributes to the vertical transport of heat, moisture and momentum on various scales.

Water vapour influences the weather and climate since it is chief controller of latent heat exchange both in horizontal and vertical and therefore principal for energy transports throughout the troposphere (Pierrehumbert et al., 2007). Thereby, water vapour variability is a key element for the development of clouds and precipitation.

Influence on radiation budget

Water vapour further has a significant effect on the radiation budget of the atmosphere (Elliott and Gaffen, 1995). As an absorber of infrared radiation it has a large influence on the greenhouse effect, i.e. much infrared radiation from the earth is stored in the atmosphere and helps to stabilise the temperature around the earth. About 60% of the greenhouse warming process can be attributed directly to water vapour, i.e., the global average temperature would be $21K$ lower without water vapour in the atmosphere. As the effect of water vapour on outgoing longwave radiation (OLR) is approximately logarithmic in specific humidity, the relatively small amount of water vapour has a great influence on the radiation budget (Held and Soden, 2000). Pierrehumbert (1999) found out that the water vapour absorption of OLR is 50 % greater than the sensitivity of OLR to CO_2. Further, the logarithmic dependence avoids the exact calculation of the

radiative effect based on the mean specific humidity alone. Pierrehumbert et al. (2007) argued that small-scale fluctuations in specific humidity affect the OLR, i.e., fluctuations at scales smaller than resolved by climate models increase the OLR and have a cooling effect.

Survey of literature on the influence of water vapour variability on weather and climate

In literature, several studies exist that demonstrate the heavy impact of tropospheric water vapour variability on weather and climate. While a lot of attention has been paid to the variability of moisture in the boundary layer, there exist also several studies that indicate the sensitivity of free tropospheric water vapour to moist convective processes (Malkus, 1954; Brown and Zhang, 1997; Sherwood, 1999; Bretherton, 2004). It is found that the tropospheric low- and midlevel distribution of water vapour is strongly relevant for convective initiation and evolution. The study of Keil et al. (2008) has clearly shown by simulations that boundary layer and mid-tropospheric humidity plays an important role for quantitative precipitation forecasts. Sherwood et al. (2010) further argued that the midlevel humidity dynamics are highly complex as a high concentration of water vapour - against expectations - does not always result in convective growth. That is, amongst others, one reason why the processes leading to the water vapour distribution in boundary layer and mid-troposphere are still a research field to be further explored.

Several studies have shown that small-scale variations in the moisture field can be significant for the development of convection (e.g., Weckwerth et al., 2000; Wakimoto and Murphey, 2008; Buban et al., 2007; Roberts et al., 2008). Crook (1996) for instance found that small-scale variations in boundary layer temperature and moisture can make a difference between no initiation of convection and intense convection. Once convection is active, its intensity has further been found to be even more sensitive to moisture variations. A positive correlation between the 'premoistening' of the free troposphere by congestus clouds and the subsequent 'superclustering' of tropical deep convection was observed by Raymond and Torres (1998).

In the present section, the impact of water vapour variability on cloud processes and radiative effects is carved out, but the mechanisms that determine the spatial variability need to be further explored.

2.3 Observing systems

For a better understanding of the mechanisms by which water vapour influences atmospheric circulation on various spatial scales, it's essential to gain observations of humidity throughout the troposphere. Water vapour is highly variable in space and time because of its interactions with convection, microphysical processes, advection and mixing by the large-scale flow, and its strong links to temperature (Emanuel and Pierrehumbert, 1996; Sherwood, 1996). It is a major challenge for observing this variability over a large temporal and spatial range. However, the distribution of humidity is poorly observed by the current observing systems (e.g., Bengtsson et al., 2004; Andersson et al., 2005). In particular, it is difficult to obtain generalised and accurate information from observations concerning variability down to small scales (Lohmann et al., 1999). In this section, the main observing systems are introduced (see also Figure 2.2) in order to demonstrate how their observations could help to clarify various water vapour processes, acting over different spatial scales.

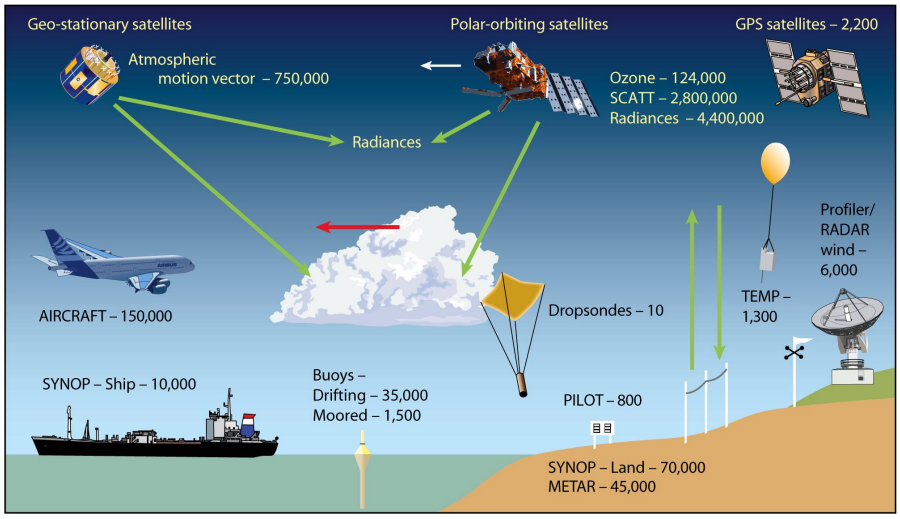

Figure 2.2: Some of the different types of systems for observing water vapour. Figure taken from Hagedorn (2010).

Humidity is routinely measured at landbased surface observing stations, at upper air mountain stations and also on ships but the database is rather used for data assimilation in NWPs than for analyses concerning the variability of humidity on spatial scales. In contrast to the near-surface observations, radiosondes provide vertical profiles with high resolution and low uncertainty, typically a few percent (Elliot and Gaffen, 1991) which allows the analysis of vertical variability.

Satellite humidity observations which date back to the late 1970s, provide additional information on water vapour with near-global coverage and thus including data also over oceans where e.g. radiosonde observations are scarce. There exist several passive satellite instruments inter alia the Atmospheric Infrared Sounder (AIRS), the Advanced Microwave Sounding Unit (AMSU-A, AMSU-B) sounders and the High Resolution Infrared Sounder (HIRS), which provide information on humidity indirectly by observing radiation emitted from the atmosphere. Although these instruments were recently improved, leading to a vertical resolution of a few kilometres in the case of AIRS (Maddy and Barnet, 2008), the data sets are still affected by cloud cover (Aumann et al., 2003). Further, retrieval of water vapour mixing ratio requires auxiliary temperature information. An alternate method which is less affected by clouds is Microwave radiation, e.g. the Special Sensor Microwave Imager (SSMI), but these imagers can only be used to estimate the column-integrated water vapour. In principle, the horizontal (> 50 km) resolution of satellite data is not sufficient in order to resolve the water vapour variability near the grid mesh size of current climate models, not to mention of high-resolution weather models. Further, satellite data is not suitable for vertically resolving water vapour structures as it does not allow for a vertical resolution that is below 3 km.

Most recently, Global Positioning Systems (GPS) technology has been developed as another source of humidity information (e.g., Healy and Thepaut, 2006; Zus et al., 2008; Poli et al., 2007), but especially occultations measure means over paths of 100 km or more which smears out convective or even mesoscale variations.

Aircraft in situ measurement of humidity is a common method during field campaigns and also onboard commercial aircrafts (see also Marenco et al., 1998). High quality sensors are used to collect data in the free troposphere with high horizontal resolution, but despite the progress that has been made in the last 20 years, measurement uncertainties and limitations are still remaining (Baumgardner et al., 2012). In particular, aircraft measurments only provide for a one-dimensional (1D) path, possibly leading to undersampling problems.

Two-dimensional water vapour fields can be collected by ground-based active remote lidar sensors via Raman backscattering and differential absorption lidar (DIAL), and have shown robustness and low uncertainty in long-term monitoring sites (e.g., Ferrare et al., 2006; Leblanc et al., 2012). However, small-scale and

fast-developing features (e.g., small-scale convective currents) cannot be captured. A combination of a high-resolution DIAL installed onboard an aircraft has been developed to collect water vapour with high horizontal (< 1 km) and vertical ($<$ 200 m) resolution (please refer to Chapter 3 for more details) including water vapour fluctuations on the kilometre scale throughout the troposphere but with limitations due to optically thick clouds.

2.4 Observational and modeling studies

A complete analysis of the processes influenced by moisture variability is beyond the scope of this study. Instead, here, a review of major essential studies that examine the interaction of water vapour with convective currents and large-scale transport processes is provided, specifically focussing on the mechanisms responsible for the variability. One challenge for studying the impact of atmospheric motions on tropospheric water vapour variability, arises from the large difference in spatial scales between small-scale convective and large-scale synoptic motions. E.g., the multitude of observing methods are individually limited by measuring based on different spatial resolutions and by covering different geographical regions which makes it difficult to derive a consistent understanding of the scale interactions. The same challenge applies also to numerical weather and climate models which have difficulties to capture the coupling between parameterised small-scale moist processes and the resolved large-scale circulation. These difficulties may be summarised as scale dependence problem (Pressel and Collins, 2012).

The complex effects of interactions between water vapour and air circulation in the troposphere includes a range of source (e.g., evaporation) and sink (e.g., precipitation) processes from convective clouds on the kilometre scale to cloud systems associated with motions on scales of a thousand or more kilometres, as well as advection of water vapor as a passive tracer outside of clouds (Emanuel and Pierrehumbert, 1996). While large-scale advection of water vapour is well represented in GCMs, the simulations of small-scale moist processes by means of parameterisations require further effort. Especially, poorly characterised processes such as evaporation or detrained precipitation in convective regions, represent a potential source of modelling errors (IPCC, 2007). Even high-resolution convection-resolving models suffer from uncertainties concerning a correct simula-

tion of the water vapour distribution (Sherwood et al., 2010; Zhang et al., 2008). Therefore, determining the mechanisms responsible for the observed variability may be helpful to reach a better understanding of interacting complex motions.

In the last decade of research, the advection-condensation or so called 'large-scale control' paradigm which provides for a limited perspective on the factors of influence that determine the water vapour distribution in the troposphere, has been developed (Pierrehumbert et al., 2007). This concept implies that water vapour behaves as a conservative tracer with respect to large-scale air motions. Mixing effects of convection are neglected and to first order, the water vapour distribution is predicted by taking into account only the large-scale wind and temperature fields without considering the water condensate in clouds (Yang and Pierrehumbert, 1994). Contrary to the general expectation, this paradigm produces fairly adequate results but especially at the regional scale the underlying trivial assumptions do not appear sufficient.

The troposphere is a thermodynamic system with forcing processes that vary due to effects from e.g., radiation, convection or ororgraphic effects, leading to large- and small-scale circulation patterns. E.g., Salby et al. (2003) showed that upper tropospheric clouds are a significant source of small-scale humidity fluctuations. In general, tropospheric humidity variability can be understood as the balance between the large-scale circulation and effects of convection on small scales. Zhang et al. (2003) have found that errors in the subgrid-scale thermodynamic fluctuations rapidly cascade upscale and affect the synoptic scale. Therefore, the intensity of convection can be determined as a major factor of influence on the water vapour variability not only on small spatial scales but also on large scales. In the tropics, the balance between outflow from upward convective motions and large-scale subsidence is responsible for the water vapour variability (Sherwood, 1996). Thereby, deep convection is a source of localised moist air mass including small-scale fluctuations arising from cloud processes. Other sources of fluctuations are vertical motions in form of gravity waves in stably stratified air that exceed the background fluctuations. Further, tropopause folds that intrude dry air deeply into the troposphere serve as a source of humidity fluctuations based on air mass boundaries that contribute to larger fluctuations, but also due to convection that causes turbulence extending into the fold (Dotzek and Gierens, 2008).

Owing to their nonlinear interactions with the resolved scales, subgrid-scale features (e.g., convection, small-scale turbulence and thermodynamic fluctuations) are key aspects of numerical weather and climate simulations. Tompkins and Berner (2008) emphasised that neglecting humidity variability on unresolved spatial scales has a large impact on forecasts. In general, parameterisations seek to couple the resolved processes to processes operating at scales that cannot be directly resolved by the model. Traditionally, deterministic parameterisation schemes are used to provide an average description of the effects of unresolved processes such as cumulus convection on the larger scales (e.g., Arakawa and Schubert, 1974; Zhang and McFarlane, 1995). However, there remains much uncertainty on how to capture convection in models, especially concerning the variability of subgrid-scale processes (e.g., fluctuations of temperature and humidity). Several studies suggest to represent convective processes in stochastic schemes using higher-order moments (e.g., the variance) (Buizza et al., 1999; Lin and Neelin, 2002). In principle, modeling of processes smaller than the model grid size can be addressed with the use of stochastic parameterisations that attempt to explicitly describe variability near the model grid length (e.g., Craig and Cohen, 2006; Kärcher et al., 2008; Plant and Craig, 2008). However, the design and testing of such schemes depends on an accurate characterisation of small-scale variability in nature, and especially subgrid-scale humidity fluctuations have not yet been empirically explored throughout the troposphere in detail (Pressel et al., 2010).

As shown in this section, several studies reveal that focusing on understanding the large-scale circulation patterns is insufficient in order to model the atmospheric water vapour variability accurately. Therefore, further investigations are required concerning the link between small- and large-scale circulation patterns in order to determine the predominant mechanisms influencing water vapour variability. In literature, the scale-dependent variability of an atmospheric field is often described by calculating power spectra or structure functions.

Observed scale dependence of water vapour

Spatial scale dependence of the tropospheric water vapour field expressed by power-law behaviour of water vapour Fourier power spectra or structure functions offers a direct means of connecting small-scale variability to large-scale variability (Pressel and Collins, 2012). The associated power-law exponents provide insight into the physical processes which play an important role in determining the variability of water vapour. In other words, such a diagnostic can be used to get an impression of the scale-resolved water vapour variance. Determining the nature and extent of scale dependence is important because the prognostic equations for probability density function (pdf) moments require estimates of the unresolved statistics (Lewis et al., 2004). In literature, several water vapour scaling exponent studies exist which are based on data sets collected by means of different observation methods, mainly via in-situ aircraft or satellite measurements. The overview of all published scale dependence studies of water vapour in the troposphere is listed in Table 2.1, showing a variety of scaling exponent values β that suppose different mechanisms acting on various spatial scales of the water vapour field.

In literature, the studies from Nastrom and Gage (1985) and Nastrom et al. (1986) are fundamental concerning the spectral analysis of kinetic energy, temperature and water vapour. For the underlying water vapour measurements, a chilled mirror dew/frost hygrometer placed on commercial aircraft provided a data set between heights of 9 km and 14 km. The water vapour spectra derived therefrom follow approximately a $\beta = 5/3$ slope at horizontal spatial scales of about 150 km to 500 km and a slope of $\beta = 2$ for scales from 500 km to 800 km. I.e., these results can not be explained by means of the theory of a passive tracer.

Mannes and Stanford (1990) analysed upper tropospheric water vapour data from the temperature-humidity infrared radiometer (THIR) by Fourier power spectra over Europe. The power-law determined for horizontal scales from 60 km to several hundred of kilometres suggests that when convective cloud energy sources are not present the enstrophy-cascading process ($\beta = 3$) may hold to much smaller scales than previously thought.

Tjemkes and Visser (1994) analysed specific humidity spectra based on the TIROS-N operational vertical sounder (TOVS) data set. They found power-laws from $\beta = 5/3$ to $\beta = 3$ but their interpretation is ambiguous.

Cho et al. (1999) found a height-dependent variability of power-laws on horizontal scales from 6 km to 60 km but did not provide a clear explanation of the

mechanisms leading to the observed vertical variability. In 2000, Cho et al. (2000) showed in a further aircraft study that power-laws from structure functions on spatial scales smaller than 100 km reveal differing characteristics for different categories of data, i.e., boundary layer results were markedly different from those of the free troposphere. In addition, they successfully applied higher-order structure functions to the data set and found higher intermittency in tropical air mass compared to extratropical airmass, possibly caused by localised wet plumes.

In 2009, the first scaling analysis of AIRS data was published by Kahn and Teixeira (2009). The study revealed highly varying power-law behaviour in the height-resolved water vapour field on scales from 150 km to 1300 km ($\beta = 1.4 - 3.0$). Similar to the study of Kahn and Teixeira (2009), Lovejoy et al. (2011) also made no definite assumption on the physical mechanisms responsible for the observed vertical and horizontal variability. While tower measeurements analysed by Pressel et al. (2010) generally confirm the observed difference between boundary layer and free troposphere (Cho et al., 2000), Kahn et al. (2011) found increasing scaling exponents with increasing height from the analysis of one-dimensional aircraft data on scales from 10 km to 100 km. The recent study of Pressel and Collins (2012), based on AIRS data with horizontal resolution of 50 km and vertical resolution of about 3 km, reveals power-laws on horizontal scales from 50 km to 500 km with a slope of $\beta = 5/3$ in the lower troposphere (925 hPa) as well as a significantly steeper slope ($\beta = 2.1$) at about 5 km height (500 hPa). They suggest that a value of $\beta = 5/3$ is a relatively universal characterisation of boundary layer structure function scaling in contrast to a value of $\beta > 2$ determined for the free troposphere which is explained by the generation of filamentary structures as the result of chaotic mixing processes. A further discussion of these research findings is included in Chapters 4 and 5.

2.5 Summary and discussion

Water vapour is the atmosphere's most important greenhouse gas and its radiation feedback has strong influence on the climate change. Therefore the relentless pursuit for a better understanding of its variability is inalienable. The role of water vapour is in particular very important to small-scale dynamical processes, such as convective currents, where it conduces as an activator, but a profound

Table 2.1: Literature review of all observed water vapour scale dependence studies. Observing systems: (S) satellite, (A) aircraft in situ, (T) tower in situ; β: slope of the power law.

Study	**Date**	**Obs. method**	**Scaling range [km]**	**Vertical range [km]**	$\boldsymbol{\beta}$
Nastrom et al.	(1986)	A	150 - 500	9 - 14	≈ 1.66
			500 - 1500	9 - 14	≈ 2
Mannes and Stanford	(1990)	S	60 - 400	upper trop.	2.7 - 3.0
Tjemkes and Visser	(1994)	S	250 - 2000	900 - 300 hPa	1.66 - 2
Cho et al.	(1999)	A	6 - 60	< 1.0	1.98
			6 - 60	1.0 - 5.0	2.25
			6 - 60	5.0 - 11.0	1.90
Cho et al.	(2000)	A	0.05 - 100	< 1.5	1.46
			0.05 - 100	< 3.5	1.63
			0.05 - 100	> 3.5	1.79
Kahn and Teixeira	(2009)	S	150 - 400	850 - 300 hPa	1.4 - 2.2
			800 - 1300	850 - 300 hPa	2.0 - 3.0
Lovejoy et al.	(2010)	A	4 - 40	12 - 14	1.99
Pressel et al.	(2010)	T	1 - 5	< 0.5	1.4 - 2.0
Kahn et al.	(2011)	A	10 - 100	< 0.3	1.64
			10 - 100	0.3 - 0.7	1.64
			10 - 100	0.7 - 1.5	1.58
			10 - 100	1.5 - 3.0	1.80
			10 - 100	> 3.0	1.90
Pressel and Collins	(2012)	S	50 - 500	925 hPa	1.66
			50 - 500	500 hPa	2.1

theory which links cloud microphysical and macrophysical behaviour to cloud condensation, heating and precipitation is still missing (Sherwood et al., 2010).

New observation techniques and improvement of existing systems enlarge the tropospheric water vapour data set continously, particularly enhancing the spatial resolution range and coverage of humidity observations. This allows to investigate the behaviour of so far poorly understood water vapour processes especially below the grid mesh size of numerical weather and climate models, more frequently. The observed small-scale variability of water vapour which is highly significant for the development of cloud-forming processes can be helpful to evaluate the small-scale variability in weather and climate models which is still a major source of uncertainty.

Despite many studies showing the enormous influence of tropospheric water vapour on clouds and precipitation, its interaction between the small-scale moist processes and the large-scale circulation, i.e., the mechanisms responsible for the observed scale dependence in the water vapour field, remains an open question. Power-law scaling of water vapour spectra or structure functions offers a direct means of connecting small-scale variability to large-scale variability (Pressel and Collins, 2012). Further, scaling can serve as a way to estimate subgrid variability as a basis for stochastic parameterisations. I.e., this knowledge can be directly applied, for example, to the design of stochastic or pdf-based parameterisations for clouds and convection by using the spectral information to construct realisations of the small-scale moisture field.

As outlined in Section 2.4, there already exist a few studies that have investigated the water vapour variability by means of computing scaling exponents of power-laws. While these studies reveal highly variable scaling exponents throughout the troposphere, a clear explanation of the underlying mechanisms leading to the different power-laws is still missing. The present thesis adds new insights to the existing results by means of a statistical characterisation of the water vapour variability, based on a unique airborne lidar data set with high horizontal and vertical resolution that allows for distinguishing the predominant physical processes responsible for water vapour variability.

Chapter 3

Data and methodology

Within the previous chapter it has been demonstrated that there is a need for accurate observations of humidity variability for purposes of evaluating NWP and climate models and improved cloud parameterisations, especially on subgrid scales. An investigation of mesoscale water vapour structures throughout the troposphere observed with the remote sensing airborne DIAL is therefore presented initially in this thesis. The water vapour observations with high horizontal and vertical resolution are used to explore a height-resolved statistic of scale dependencies of the water vapour variability. Further, specific humidity data simulated by the local NWP model of the DWD, called COSMO-DE, are analysed and compared with the observed scaling statistic.

In Chapter 3, the operation mode of lidar, specifically the differential absorption lidar, is explained. Furthermore, general information on the COSMO model and the analysis methods are outlined. In detail for purposes of the following analysis, Section 3.1 is to provide an overview of the lidar history, the underlying physical

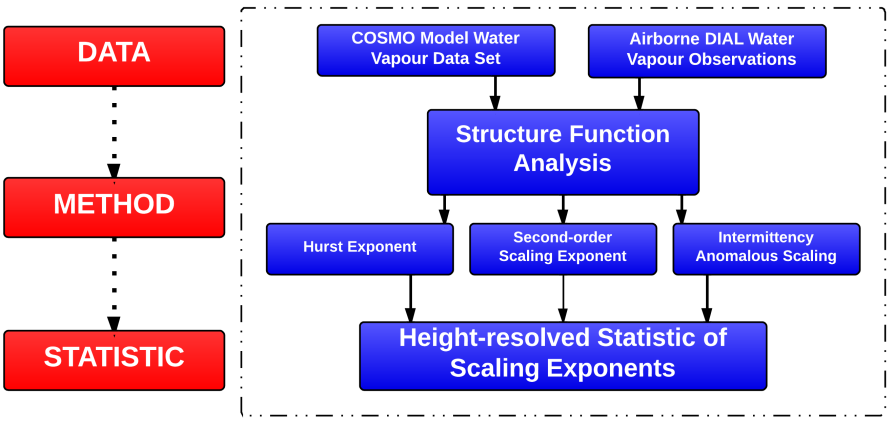

Figure 3.1: Overview on the analysis steps: Data, method and statistic.

principles (see Section 3.1.1) and the airborne DIAL developed at the DLR (see Section 3.1.2). Section 3.2 is to generally describe the high-resolution COSMO model and to define the scopes of the data set in the following analysis. Finally, in Section 3.3, the structure function analysis method is explained in detail. A brief theoretical overview of the whole analysis process beginning with data selection, followed by the determination of the applicable evaluation method and resulting in the unique statistic is shown in Figure 3.1.

3.1 Lidar observations

History

Airborne differential absorption lidar (DIAL) instruments for water vapour observations are developed at the Deutsches Zentrum für Luft- und Raumfahrt (DLR) since the mid 1980's (Ehret et al., 1993). The classical research of such laser systems has its origin in the 1960's, but for a long time the measurements were constricted by large uncertainty due to the maturity of the laser technology, mainly the lack of wavelength stability and spectral purity. Hence, with the progress in optical and electronic technology the development of lidar technology has been pushed. In principle, the lidar has been developed to make use of several specific interaction processes of the emitted laser beam with the atmospheric constituents which are elastic-backscatter lidar, Raman lidar, fluorescence lidar, Doppler lidar and differential absorption lidar (see also Figure 3.2). For purposes of this study the focus is laid on the differential absorption lidar (DIAL).

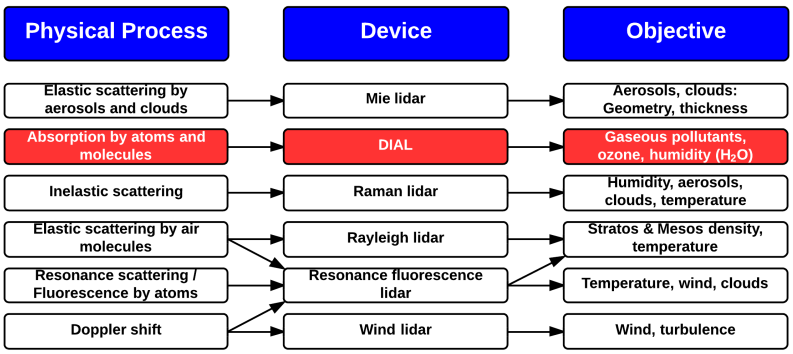

Figure 3.2: Overview of physical processes leading to different lidar applications.

Only few years after the invention of laser by Maiman (1960), Richard M. Schotland collected the first water vapour measurements by using DIAL (Schotland, 1966). He measured vertical profiles of water vapour by thermally tuning a ruby laser on and off the water vapour absorption line at 694.38 nm. In 1981, Browell made the first airborne DIAL measurements of water vapour profiles in the troposphere (Browell, 1983). Since 1985, the lidar department at the DLR Institute for Atmospheric Physics has developed and applied airborne water vapour DIALs. Great strides were made both in the development of lidar technologies and instrumentation resulting in improved measurement accuracy, availability, range and resolution. In 2007, a unique system has been developed at the DLR which uses a four-wavelength/three-absorption line measurement scheme in the 935 nm H_2O absorption band (Wirth et al., 2009). Problems of the two-wavelength systems, such as the lacking coverage of profiling, are solved by this high performance airborne DIAL. Data from this system were used in this thesis.

3.1.1 Physical picture of lidar

In principle, lidar (light detection and ranging) uses laser light in the sensing. Typically, light is reflected via backscattering and received by the lidar detector (see Figure 3.3). To relate the received light power with the transmitted laser power the fundamental lidar equation is introduced:

$$\underbrace{P_s(\lambda, R)}_{1} = \underbrace{P_L(\lambda_L)}_{2} \cdot \underbrace{\beta(\lambda_L, \lambda, R)}_{3} \cdot \underbrace{\frac{A}{R^2}}_{4} \cdot \underbrace{[T(\lambda_L, R) \cdot T(\lambda, R)]}_{5} \cdot \underbrace{[\eta \cdot G(R)]}_{6} \tag{3.1}$$

P_s is the returned power detected at wavelength λ and distance R, and P_L is the transmitted laser power. The backscatter coefficient β stands for the scatter probability back to the lidar under an angle of 180°. The 4th term is the ratio of the receiving telescope area at the range R, and the 5th term describes the atmospheric transmission at outgoing wavelength λ_L and return signal at wavelength λ, given by the Lambert-Beer-Bouguer law:

$$T(\lambda_L, R) = exp[-\int_{R_0}^{R} \alpha(\lambda_L, R)\, dR]. \tag{3.2}$$

(for the returned signal wavelength λ_L is replaced by λ). α is the extinction coefficient and the integration goes from the location of the lidar R_0 to the distance

R. The 6th term of Equation 3.1 describes the optical efficiency η that considers losses by mirrors and filters, detector etc. and the geometrical form factor of the overlap between the laser beam and the telescope field of view.

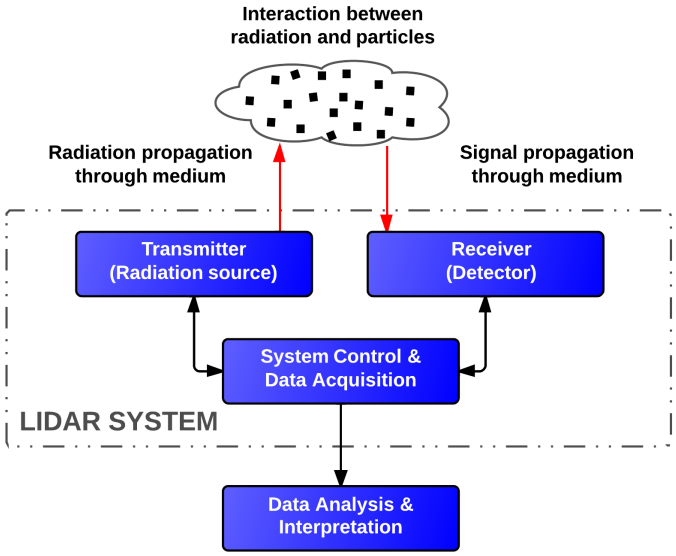

Figure 3.3: Physical picture of lidar remote sensing.

Equation 3.1 is based on the physical picture of active remote sensing (see Figure 3.3) where radiation propagates in a medium, interacts with the particles and finally is scattered back into the receiver. The equation is based on the following two assumptions. First, the scattering processes are independent which means that particles are separated adequately and undergo random motion. Secondly, only single scattering occurs. The latter assumption implies that a photon is scattered only once, which is true in cloud free situtations. There are several physical processes which interact between light and particles leading to different applications of lidars (see Figure 3.2). The focus in this thesis is exclusively on the differential absorption process handled by DIAL.

3.1.2 Differential absorption lidar concept

Methodology

The DIAL technique makes use of laser probing of the atmosphere at two distinct wavelengths, including an online wavelength which is placed at an absorption line of water vapour and an off-line wavelength positioned outside of the absorption line to serve as a reference. Figure 3.4 shows the measurement principle of DIAL

with the typical absorption line dependent on wavelength λ. While it can be applied to remotely measure several atmospheric gases, e.g. H_2O, O_3, SO_2, CH_4, CO_2, the focus in this study will be on water vapour measurements only. The identification of the water vapour density is based on the Equations 3.1 and 3.2.

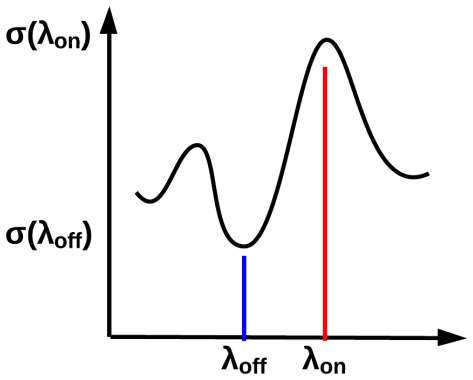

Figure 3.4: Absorption cross section σ with dependency as function of wavelength λ.

By making use of the fact that the extinction α (m^{-1}) is linearly proportional to the trace gas molecule number density n(R)

$$\alpha(\lambda, R) = n(R) \cdot \sigma(\lambda, R) \tag{3.3}$$

the trace gas molecule number density n at range R is finally obtained from the ratios of on- λ_{on} and offline λ_{off} return signals on the basis of the lidar equation (see Equation 3.1). The differential form of the DIAL equation results in the following formula (Schotland, 1974):

$$n(R) = \frac{1}{2\Delta\sigma(R)} \frac{d}{dR} ln[\frac{P_s(\lambda_{off}, R)}{P_s(\lambda_{on}, R)}] \tag{3.4}$$

with $\Delta\sigma(R) = \sigma(\lambda_{on}, R) - \sigma(\lambda_{off}, R)$. $\Delta\sigma$ is the effective cross section of the molecular absorption line which is a relevant factor in the DIAL equation (see Figure 3.4). Note that the absorption cross section may change due to its temperature and pressure dependence.

As shown by two examples in Figure 3.5, the selection of appropriate absorption lines is stringent for DIAL. The two plots demonstrate two extreme cases for the relation of on- λ_{on} and offline λ_{off} return signals dependent on the distance R from the DIAL. If the absorption is too strong (narrow shape in Figure 3.4) the online signal gets attenuated too quickly and the useful profiling range will be too short

(see Figure 3.5(a)). If, in contrast, the absorption is too weak, differentiation of the on- and offline signals will only give noise (see Figure 3.5(b)) (Kiemle, 2008). Further, temperature dependency which varies for different absorption lines should be minimised and a high quality of laser and detector technology is required. Equation 3.4 is valid under the assumption that the overlap function

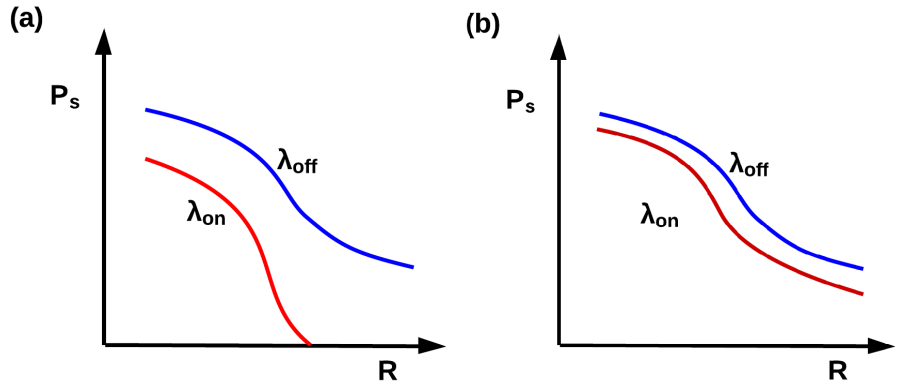

Figure 3.5: The received power P_s vs. distance R from the DIAL is plotted for two examples in which the extinction of online wavelength due to absorption is (a) too strong and (b) too weak.

G(R) (see 6th term of Equation 3.1) is identical for on- and offline wavelengths. Further, it is important that the online wavelength is spectrally very narrow and stable. Before calculating the humidity from the number density n (see Equation 3.4) a lower instrumental noise, i.e. a higher signal-to-noise-ratio (SNR), can be achieved by horizontal and vertical averaging of the received power P_S. For the data employed in this study, the horizontal resolution varies from 5 - 25 s (1 - 5 km) and the vertical resolution is about 150 m. By using the ideal gas law the specific humidity q is computed from n as follows:

$$q(R) = \frac{R_{air}}{R_{H_2O}} \frac{n(R)kT(R)}{p(R)} \tag{3.5}$$

The first term describes the ratio of the specific gas constant of dry air R_{air} and water vapour R_{H_2O} which is 0.622. k is the Boltzmann constant and in general, the temperature T and the pressure p are obtained from profiles of the standard atmosphere or NWP models.

Additionally, the offline wavelength λ_{off} contains information about the aerosol concentration and cloud cover of the probed atmosphere. In this thesis aerosol measurements collected from the unused pump radiation at 1064 nm and 532 nm

which is transmitted to the atmosphere are used to detect the cloud top height in the two-dimensional aerosol backscatter field.

Airborne water vapour DIAL

The water vapour data set underlying the following analysis (see Chapter 4 and 5) was collected by the airborne DIAL with the WALES demonstrator, developed at the DLR and successfully tested in 2007 (details of the system are listed in Table 3.1). The aircraft as a mobile platform makes it possible to participate on many field campaigns, to choose regions which are otherwise hard to access, and to cover large areas for investigating various phenomena throughout the troposphere. By using four different wavelengths in the 935 nm absorption band of H_2O, a large range of different water vapour concentrations is covered and therefore water vapour profiles from the lower stratosphere down to the boundary layer are collected with high accuracy.

The system consists of two transmitters generating pulsed radiation on four selectable wavelengths between 935 and 936 nm having a total average optical power of 8 W (see also Table 3.1). In principle, the radiation from an Nd:YAG pump laser is frequency doubled and then converted to a wavelength of 935 nm by an optical parametric oscillator (OPO). OPOs are tunable laser crystals which are chosen to optimise the wavelength choice. Each transmitter sends two spectrally narrow pulses with 40 mJ energy at different wavelengths.

Table 3.1: Characteristics of the DLR airborne water vapour lidar system

	WALES DIAL
Wavelengths	3 on- and 1 offline
Wavelength tuning range	920 - 950 nm
Pulse energy	40 mJ
Pulse rate	200 Hz
Output	H_2O concentration
Vertical/horizontal resolution (H_2O)	150 m / 2000 m
Precision (noise)	0.4 g/kg
Accuracy (bias)	2 %

With the old two-wavelengths DIAL, the aircraft had to fly repeatedly at different levels, optimising the absorption line at every level to acquire profiles throughout the troposphere. In contrast, with the new four-wavelengths DLR DIAL with its three online wavelengths for absorption lines of different strength

a single aircraft overpass is sufficient to obtain full tropospheric profiles of water vapour. In principle, the DIAL noise increases with distance from the lidar and with decreasing optical depth, i.e. water vapour density. The fact that water vapour density increases towards the ground, i.e. the extinction increases as well (see Equation 3.3), nearly compensates the signal loss and enlarges the profiling range. Further, the accuracy of the new system is improved by a higher output power (40 mJ), a larger telescope aperture (0.48 m) and less detector noise. For further technical details, please refer to Wirth et al. (2009).

Using the DIAL technique for narrow absorption lines onboard an aircraft is technically demanding but very powerful for water vapour profiling. In principle, airborne DIAL has been applied to atmospheric phenomena that range from the boundary layer up to the stratosphere. Several studies have demonstrated the applicability of airborne DIAL measurements to investigate the tropospheric water vapour field with high spatial and temporal resolution (e.g., Bhawar et al., 2011; Kiemle et al., 2008). In this thesis, data from the field experiments COPS/ETReC in 2007, THORPEX-IPY in 2008 and T-PARC in 2008 are analysed to make a unique contribution to the research of small-scale water vapour variability whose knowledge is essential for parameterising moist convective processes in weather and climate models.

3.2 COSMO-DE model data

In this thesis, data from the local numerical weather model COSMO-DE of the German meteorological service (DWD) is compared to DIAL observations. In principle, the model is evaluated by comparing the simulated water vapour variability, expressed by scaling exponents, with the DIAL observations for the nearby same spatial scales (10 km to 100 km). Thereby, it is tested, if the high-resolution model COSMO-DE captures the observed small-scale variance under similar meteorological situations.

Operational setup

The COSMO model is the operational, limited-area numerical weather prediction model of the DWD and is designed as a nonhydrostatic atmospheric prediction model which is based on primitive hydro-thermodynamical equations (Baldauf et al., 2011). This model version became operational in April 2007 and is used

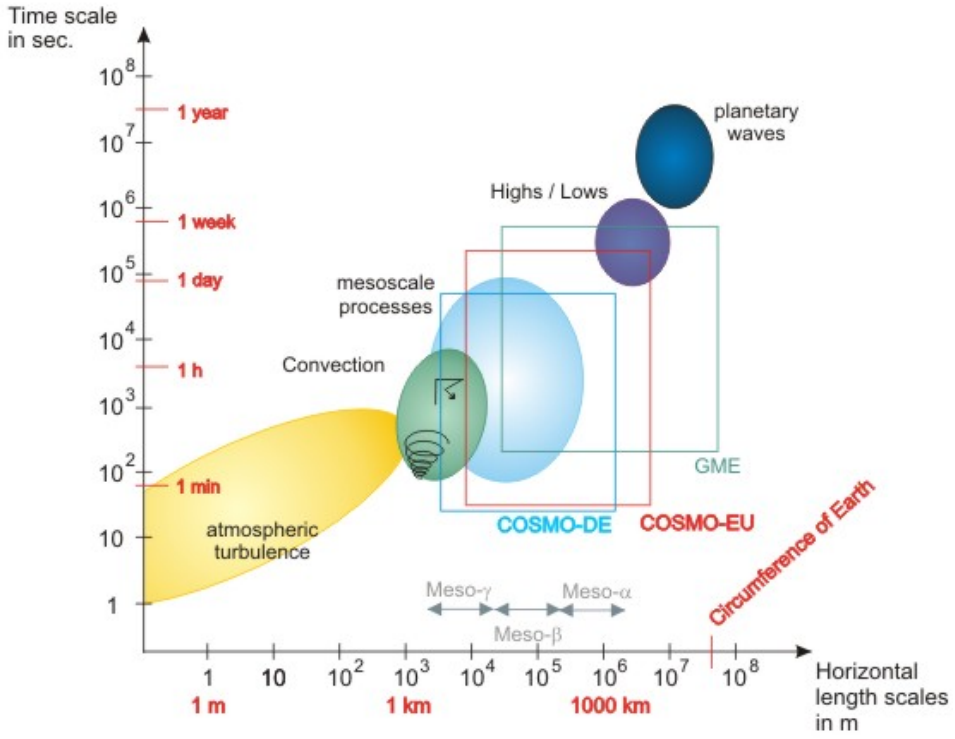

Figure 3.6: Scales and related physical processes resolved by the different COSMO-DE in comparison with COSMO-EU and the global model GME. (Source: www.dwd.de)

at the DWD for short range weather forecasts over Germany. The operational COSMO-DE simulations consist of high-resolution three-dimensional simulations on a grid of 421 x 461 x 50 points over a region covering the whole of Germany and some surrounding states, including Benelux countries, Austria and Switzerland in their entirety. The horizontal grid spacing is about 2.8 km and the time-step is 25 s. While deep moist convection and the associated feedback mechanisms to the larger scales of motion are explicitly resolved, shallow and midlevel convection is still required to be parameterised with the Tiedtke scheme (Tiedtke, 1989) (see also Figure 3.6). Precipitation processes are explicitly described using a bulk-type cloud micro-physical scheme. The parameterisation of cloud cover is highly affected by small-scale moisture fluctuations, in particular the calculation of fractional cloud cover presumes information of the inhomogeneous humidity distribution. The COSMO model uses a relative humidity based scheme in the radiation scheme and a pdf-based scheme within the turbulence model to parameterise boundary layer clouds.

Chapter 3 Data and methodology

Simulation setup

For purposes of the analysis of water vapour variability, the official domain of COSMO-DE (421 x 461 gridpoints) is enlarged up to 2481 x 1521 gridpoints (about 7000 km x 4250 km), which includes a lager area over sea. The operational horizontal grid spacing of about 2.8 km is used. The local model is driven by IFS (the global NWP model of the ECMWF) analysis and forecasts which provide the lateral boundary conditions for the COSMO-EU. The COSMO-DE with a resolution of about 2.8 km is nested into the COSMO-EU with a horizontal grid spacing of 7 km.

In the vertical, the COSMO-Model offers 50 irregularly distributed layers, starting from 10 m and going up to 21500 m above ground. The model levels are orographically-following at the lower levels but smoothly changing into isobaric-following levels in the upper troposphere. To avoid artificial signals from interpolation, the analysis of the water vapour field in this thesis is performed on the terrain-following σ-levels. Furthermore, data was analysed only over flat terrain or over sea and the lowest model data level used is at about 1.5 km height. Therefore the σ-levels can be assumed as constant referring to height. Skamarock (2004) has found that it has no significant influence for the spectral analysis of the data, if constant model, pressure or height surfaces are used.

The distribution of water vapour in the troposhere is highly variable and affected by complex motions on various ranges of scales. In this thesis, the interest of investigation is laid on the mesoscale starting with a few kilometres up to about 100 km on the horizontal range. By applying a grid spacing of 2.8 km it is expected that deep convection can be simulated without using a parameterisation scheme (Doms et al., 2011), i.e., the total life cycle of such local weather systems can be described in more detail by the model. Understanding the distribution of water vapour is of central importance to the representation of clouds in weather models which are important for quantitative precipitation forecasts. Further, due to their radiative impact, clouds play a fundamental role in weather and climate modeling (IPCC, 2007). The COSMO-DE model uses parameterisations for subgrid-scale clouds, grid-scale clouds and precipitation. The cloud microphysical schemes provide the latent heating rates for the dynamics and represent a central part of every atmospheric model.

In this study, a 3-day-period from the COPS field campaign was simulated. The simulation with the IFS analysis starts on 00 UTC July 19th in 2007 and

then the three hourly deterministic forecast is used to further simulate. The run encompasses 75 hours, where the water vapour field, i.e. the specific humidity model output, is available every hour. The weather situation during this period was characterised by an almost stationary low pressure system over Great Britain which caused heavy and strongly forced convection over middle Europe.

3.3 Structure functions and scale dependence analysis

Why using structure functions?

In literature, the variability of an atmospheric field is often described by calculating the variance or scale resolved the power spectrum. Without a doubt, the power spectral method has proven extremely powerful and has been successfully applied to identify aspects of turbulence such as energy cascades, but in terms of identifying structures, the method is ambiguous, i.e. different looking processes can lead to identical spectral slopes. For example, randomly distributed Dirac delta functions and white noise yield both a flat power spectrum, even though their intermittency is totally different (Marshak et al., 1997). Structure functions of different orders provide additional information to distinguish between these different structures in time series. Figure 3.7 demonstrates, that the slope of the second-order structure function ζ_2 (which is equivalent to the Fourier power spectrum under certain circumstances) yields flat slopes for both white noise and randomly distributed Dirac delta functions. While the power spectrum method and the second order structure function would suggest the same spatial variability for such different looking processes, the calculation of higher order structure functions allows a more accurate description. In fact, the intermittency of these two synthetic time series is totally different, i.e. randomly distributed Dirac delta functions show high intermittency, white noise shows no intermittency. Further, structure functions are real space analyses based on fluctuations at a given scale defined by differences which simplifies the performance and the interpretation in contrast to the Fourier frequency or wavenumber analysis.

In principle, the obvious advantage of the power spectrum is to identify distinct spectral peaks for dominant, periodic occurent scales in stationary time series (see e.g., Hsu et al., 2011). The data set used in this thesis is definitely characterised

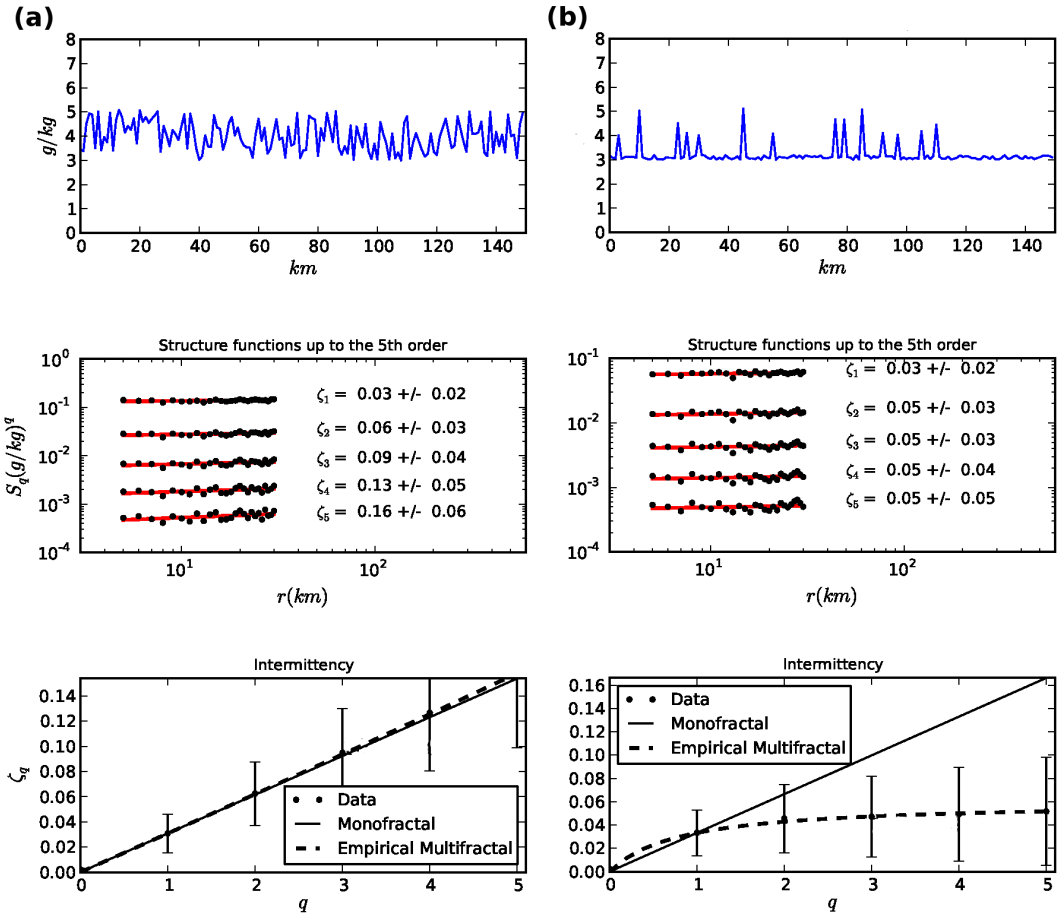

Figure 3.7: Structure function analysis of (a) white noise and (b) randomly distributed Dirac delta functions. Synthetic time series (top); Structure functions of the time series up to fifth order (middle); Average slopes ζ_q versus order q (bottom).

by non-periodic time series, with fluctuations and nonstationary increments. For such aperiodic fluctuations specifically those including random events, the power spectrum approach loses some of its appeal (Musial et al., 2011).

Furthermore, optical thick clouds lead to gaps in the DIAL signal, i.e. the time series are not provided on a regular time grid anymore. Usually these gaps have to be filled by a certain approach. Zhan et al. (1996) have shown that filling the gaps by linear interpolation reduces the power of the spectrum at high frequencies, which increases the magnitude of the slope. To avoid gap filling and to handle unevenly spaced data, the Lomb-Scargle method has been developed by Lomb (1976) and Scargle (1982, 1989) and recently updated by Hocke and Kämpfer (2009). Even though the Lomb-Scargle method was specifically designed to retrieve the periodogram of unequally spaced data, it is particularly

appropriate to process strongly periodic signals, but less apt to deal with aperiodic time series (Musial et al., 2011). In contrast, the structure function method profits from being unaffected by data gaps (Linfield et al., 2001; Do et al., 2009) while increments formed to gaps are discarded.

For the reasons mentioned above, this thesis focuses on calculating structure functions up to the fifth order, i.e., identifying scale invariance over horizontal ranges and extracting more structural information of the water vapour field by calculating the intermittency.

The structure function method

As a basis for the analysis of the observed and the modeled water vapour field the one-dimensional horizontal structure function (e.g., Davis et al., 1994)

$$S_q(r) = \langle |f(x_i + r) - f(x_i)|^q \rangle \tag{3.6}$$

is calculated for different orders q. $\langle\rangle$ denotes an ensemble mean over all pairs of points separated by a distance r. In detail, the calculation of structure function is started by using a distance $r = 1$, which is, in matters of the lidar observations, the flight distance covered by the DLR Falcon between two adjacent elements of the time series $f(x_i)$ with a total of N equidistant elements.

Therefore, the hypothesis of Taylor (Taylor, 1938) is invoked for transforming the intervals from time to space using the aircraft speed. In detail, if the aircraft speed $v_{aircraft}$ is much higher than the target movements, temporal measurements can be transformed to spatial patterns with the transformation

$$r = v_{aircraft} \cdot t_{DIAL}. \tag{3.7}$$

In the applied data set the aircraft speed varies between 160 - 240 m/s which can be assumed to be much faster than changes in water vapour structures. In other words, under Taylor's hypothesis, water vapour structures can be considered frozen in time as they are overflown by airborne lidar. Although water vapour structures do evolve with time, the duration of the structures is long enough in comparison to the DIAL scanning time t_{DIAL} so that the Equation 3.7 can be applied to examine the spatial structures and variability of water vapour.

Relating to the NWP model COSMO-DE, the distance r stands for the horizontal grid mesh size of 2.8 km. In general for a separation r, the absolute values

of $N - r$ pairs of points, the so called increments, are calculated. Because of the finite size of flight segments respectively of the model domain, the ensemble mean is approximated by the arithmetic mean in practice:

$$S_q(r) = \frac{1}{N-r} \sum_{i=1}^{N-r} |f(x_i + r) - f(x_i)|^q \tag{3.8}$$

This routine is repeated for increasing r from 1 up to $N - 1$ and for higher orders q, ending with $q = 5$. Finally, scaling behavior as a power-law dependence of structure functions on length scale is identified which is represented by the relation

$$S_q(r) \propto r^{\zeta_q}. \tag{3.9}$$

Power-law fitting is done by first converting Equation 3.10 to a linear equation and then fitting a set of N data points ($x_i = log(r_i)$, $y_i = log(S_q(r_i))$) to a straight line, i.e.

$$S_q(r) = a \cdot r^{\zeta_q} \tag{3.10}$$

is converted to

$$log(S_q(r_i)) = log(a) + \zeta_q \cdot log(r_i). \tag{3.11}$$

For estimating the uncertainties of the slope ζ_q, the variance of the slope ζ_q is calculated by using the chi-square merit function (Press et al., 2007). Therefore, the individual errors σ_i in the measurement y_i which are unknown, are set to 1:

$$S \equiv \sum_{i=0}^{N-1} \frac{1}{\sigma_i^2}, S_x \equiv \sum_{i=0}^{N-1} \frac{x_i}{\sigma_i^2}, S_y \equiv \sum_{i=0}^{N-1} \frac{y_i}{\sigma_i^2}, S_{xx} \equiv \sum_{i=0}^{N-1} \frac{x_i^2}{\sigma_i^2}, S_{xy} \equiv \sum_{i=0}^{N-1} \frac{x_i y_i}{\sigma_i^2}. \tag{3.12}$$

The slope of the linear regression is calculated as

$$\zeta_q = \frac{SS_{xy} - S_x S_y}{SS_{xx} - (S_x)^2} \tag{3.13}$$

and $log(a)$ as:

$$log(a) = \frac{S_{xx} S_y - S_x S_{xy}}{SS_{xx} - (S_x)^2} \tag{3.14}$$

and the probable uncertainty (variance) in the estimate of ζ_q:

$$\sigma_{\zeta_q}^2 = \frac{S}{SS_{xx} - (S_x)^2} \cdot \sqrt{\chi^2/(N-2)}. \tag{3.15}$$

χ^2 is computed by

$$\chi^2(log(a), \zeta_q) = \sum_{i=0}^{N-1} (y_i - log(a) - \zeta_q x_i)^2 \tag{3.16}$$

using the fitted parameters $log(a)$ and ζ_q.

In this study, the structure function exponent ζ_q is determined by fitting a straight line in the log-log space to the structure functions of all orders between ranges of about 5 km to 100 km for the lidar observations. Concerning the effective resolution of the COSMO-DE which incorporates a factor of about 4 to 5 of the horizontal grid spacing corresponding to 11 km to 14 km (Bierdel et al., 2012), the scaling analysis of the model data set ranges from 11 km to 100 km.

To check whether the power law fit is exact enough to indicate scaling, Pressel and Collins (2012) introduced an ad hoc lower bound on the coefficient of determination R^2. This method is also known as R-square and can be interpreted as the goodness of fit of a linear regression. R^2 is the square of the correlation between the structure function values and the values of the predicted fit and is defined as

$$R^2 = 1 - \frac{\sum_{i=1}^{n}(S_q(r_i) - f_i)^2}{\sum_{i=1}^{n}(S_q(r_i) - \overline{S_q(r)})^2} \tag{3.17}$$

where $S_q(r_i)$ is the structure function value, f_i is the predicted value from the fit and $\overline{S_q(r)}$ is the mean of the structure function value. R-square can take on any value between 0 and 1, with the latter indicating that the regression line perfectly fits the data. In this thesis the lower bound on R^2 of 0.95 is adopted for the scaling analysis.

Figure 3.8 (middle) shows two examples of structure functions up to the fifth order, computed as described above. The red lines are the least square fit results, with slope ζ_q, the variance of the slope and the goodness of fit R^2.

Since for increasing values of r, the number of increments $|f(x_i + r) - f(x_i)|$ decreases, the weighting goes linearly in favour of the smaller scales. On the other hand, Figure 3.8 (middle) shows that for increasing values of r, the density of sampling points increases exponentially in the log-log plot, giving more robustness to the linear fit and the scaling exponent in the larger scales. Also apparent is the increasing uncertainty of the scaling exponent and of the linear fit for increasing order q.

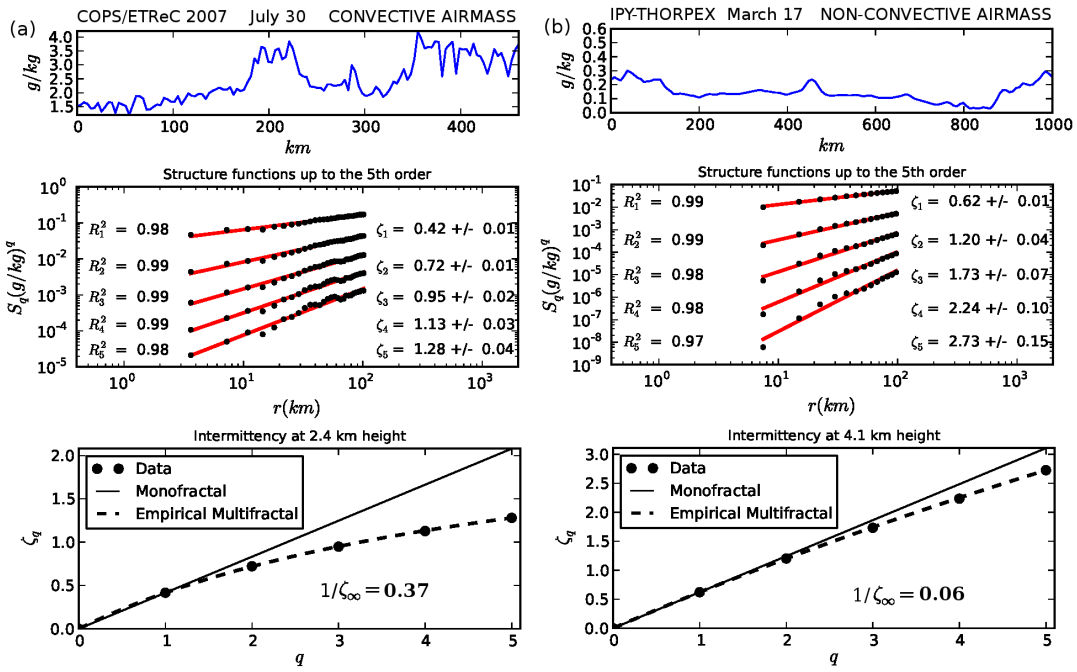

Figure 3.8: Structure function analysis of two example time series in the convective (a) and non-convective regime (b) at (a) 2.4 and (b) 4.1 km height. Representative specific humidity data samples (top); Structure functions of the time series up to fifth order (middle); Average slopes ζ_q versus order q (bottom). The intermittency $1/\zeta_\infty$ is calculated using a parameterisation of Pierrehumbert (1996); Lower values indicate lower intermittency. See Chapter 5 for description of the data.

In the following sections the characteristics of the different orders of the structure function method are discussed in detail.

3.3.1 First-order structure function

The scaling exponent of the first-order structure function ζ_1, often called Hurst exponent H or 'smoothness', characterises the nonstationarity of the data (Marshak et al., 1997). It can be used to quantify power-law scaling and to characterise the spatial correlative structure of an atmospheric field (Pressel and Collins, 2012). The range of ζ_1 is from zero to one, with values near zero characterising rough, nearly stationary signals and values near one characterising smooth, nonstationary signals (Tuck et al., 2003). Following the original work of Hurst (1956), a value of $H = 0.5$ indicates an uncorrelated random process whereas random processes with a value of $H < 0.5$ indicates anticorrelation. I.e. each data value is more likely to have negative correlation with preceding values and values of $H > 0.5$ can be taken to indicate persistence or long range correlations. The

Hurst exponent influences also the fractal dimension which measures to what extent the random process fills space. The measure for the fractal dimension is D with $D = 2 - H$. By this definition, smaller Hurst exponents would indicate processes that are more space filling.

For illustrating the different processes, depending on whether the Hurst exponent H is smaller or larger than 0.5, two examples of synthetic time series with different Hurst exponents ($H = 0.3$ and $H = 0.65$) are shown in Figure 3.9. These sample paths of a fractional Brownian motion with Hurst exponent H in (0,1) were simulated by using the circulant matrix method for generating stationary Gaussian processes with known covariance function (Wood and Chan, 1994; Coeurjolly, 2001). The two series clearly display differences in smoothness and spikyness. While smaller Hurst exponents lead to rough and spiky time series (see Figure 3.9 left), time series showing larger Hurst exponents are smoother (see Figure 3.9 right).

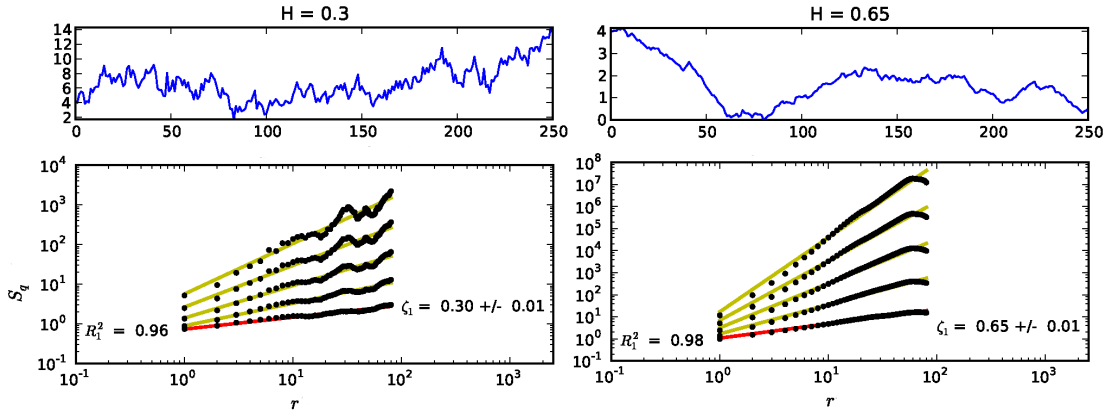

Figure 3.9: Two synthetic time series (top) having Hurst exponents of (left) $H = 0.3$ and (right) $H = 0.65$. The bottom plots show the fitted lines to the first order (red line) up to the fifth order (yellow lines) structure function computed from the Gaussian random process. The Hurst exponent ($H = \zeta_1$) and the R-square value are also denoted.

3.3.2 Second-order structure function

The second-order structure function S_2 is well known because of its Fourier duality with the power spectrum. Based on the one dimensional second-order structure function,

$$S_2(r) = \langle |f(x_i + r) - f(x_i)|^2 \rangle \tag{3.18}$$

and by using $f(x_i) = f_1$ and $f(x_i + r) = f_2$, Equation 3.18 is equivalent to:

$$S_2 = \langle |f_2 - f_1|^2 \rangle = \langle f_2^2 \rangle + \langle f_1^2 \rangle - 2\langle f_2 f_1 \rangle. \tag{3.19}$$

For stationary time series $\langle f_2^2 \rangle = \langle f_1^2 \rangle$.
By using the covariance $cov(r) = \langle f(x+r)f(x) \rangle = \langle f_2 f_1 \rangle$, Equation 3.19 becomes:

$$S_2 = 2(cov(0) - cov(r)). \tag{3.20}$$

Finally, with the use of the Wiener-Khinchin theorem

$$cov(r) = \int_{-\infty}^{\infty} e^{-ikr} E(k)\, dk \tag{3.21}$$

the second-order structure function can be written as

$$S_2(r) = 2 \int_{-\infty}^{\infty} (1 - e^{-ikr}) E(k)\, dk. \tag{3.22}$$

If we put $E(k) \propto k^{-\beta}$ into Equation 3.22 and integrate the whole term, the relation between the second-order scaling exponent and the slope of the power spectrum is approximately

$$S_2(r) \approx k^{-\beta+1} \approx r^{-\zeta_2} \tag{3.23}$$

Under the assumption that power-law relations are satisfied for all encompassed scales a relation between the scaling exponent of the second-order structure function ζ_2 and the spectral exponent β

$$\zeta_2 = \beta - 1 \tag{3.24}$$

can be derived (Lewis et al., 2004). Fourier spectra are insufficient insofar as they only fully reproduce stationary time series. In the case at hand, two water vapour fields with identical second-order statistics may still display substantially different variability. On the other hand, structure functions of higher order can provide additional information (Marshak et al., 1997). Indeed, only in the case of so-called ordinary scaling (constant ratio ζ_q/q), second-order structure functions provide the same information about the signal as power spectra. If the structure functions of higher order show anomalous scaling (ζ_q/q variable), the deviation

from linear (ordinary) scaling describes the degree of intermittency, with larger deviations from linear scaling indicating increased intermittency (Pierrehumbert, 1996) (please refer to Section 3.3.3).

Figure 3.10 shows an example of computing second-order structure function (left) and power spectrum (right) of one exemplary time series (see Figure 3.8 top left). The calculated exponents from the two methods are not identical, but similar. The least-squares fit of the calculated power spectrum gives a slope of $\beta = 1.49$ which would by the use of Equation 3.24 result in a second-order structure function exponent of $\zeta_2 = 0.49$. The result of the structure function method is indeed 0.25 larger ($\zeta_2 = 0.74$) which could have several reasons. First, the Wiener Khinchin theorem is only valid under the assumption that the atmospheric field is stationary. And second, the comparison of both methods shows that the structure

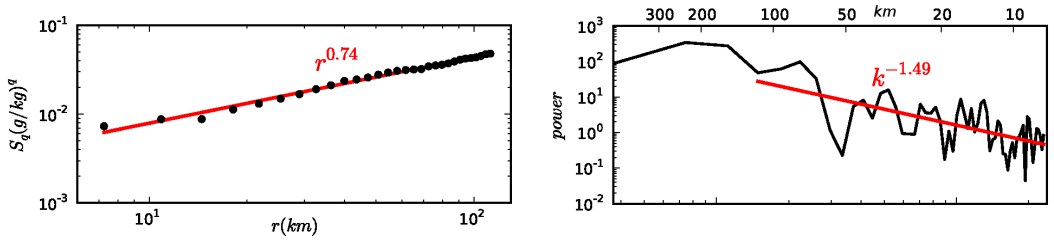

Figure 3.10: Comparison of (left) the second-order structure function and (right) the power spectrum of the time series shown in Figure 3.8 (top left).

function is more regular than the spectrum (Deschamps et al., 1981). Therefore, the fitting procedure of the slope of the power spectrum is afflicted with larger uncertainty than the one of the structure function. To sum up, it can be said that the differing slopes calculated via power spectrum and second-order structure function could be caused by both, the uncertainty of the fit (technical effect) and the consequence of intermittency (physical effect).

Nevertheless, studying the slope of the structure function is generally limited by the noise level at the smallest scales. In principle, the signal to noise ratio of the airborne water vapour DIAL is critical for small-scale features and large distances from the instrument. Figure 3.11 shows an exemplary power spectrum (left) and the corresponding second-order structure function (right) of one time series. They are both dominated by white noise in the small scales, i.e. the atmospheric variability is weaker than the instrumental noise. The spectrum is characterised by a flat part in the higher frequencies with a clear transition to atmospheric variability. The level of the white noise depends on the amount of water vapour

in the troposphere and the distance from airborne lidar (Kiemle et al., 2011). The data set used in this thesis has white noise thresholds varying from 2 km to 7 km in the horizontal range. Both the spectrum and the structure function are characterised in this frequency region by a noise constant, which precludes the exponent determination at these scales and smaller scales. Therefore the data set used in this thesis is smoothed spatially to reduce the noise (Deschamps et al., 1981; Murphy, 1989).

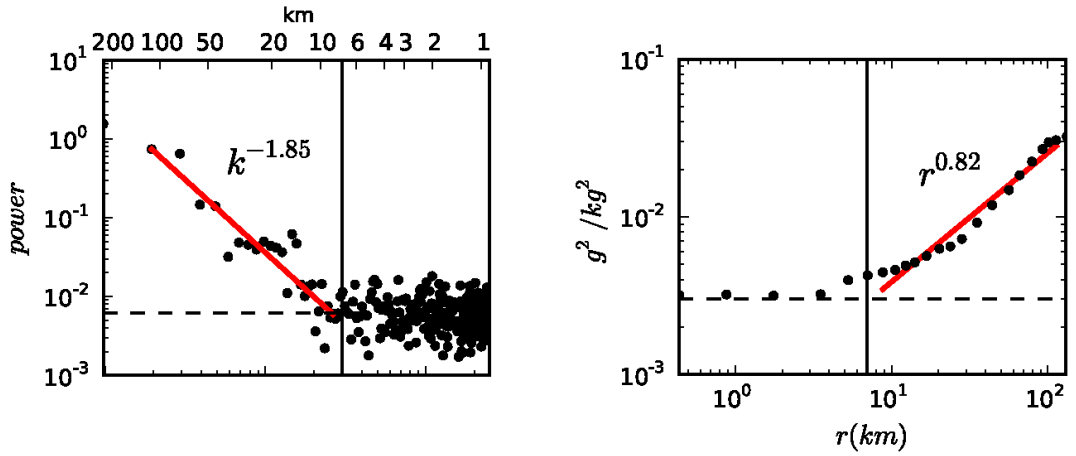

Figure 3.11: Comparison of (left) the power spectrum and (right) the second-order structure function concerning the behaviour of noise in the data. The example is from the COPS data set on 8 July in 2007.

3.3.3 Higher-order structure functions and intermittency

For higher orders, the scaling exponents can deviate from a linear increase with order q. These deviations are known as multifractal or anomalous scaling and imply that the form of the probability distribution will vary, such that their 'tails' will be increasingly flared out (Shraiman and Siggia, 2000). Intermittency is a measure of this phenomenon, since higher orders emphasize increasingly larger humidity excursions.

Structure functions of higher orders are necessary to fully characterise nonstationary time series. The intermittency can be calculated from the variation of the scaling exponents ζ_q with q. Figure 3.8 (left bottom) shows a typical case of high intermittency in the lower troposphere (at 2.4 km height) using the data of Figure 3.8 (top left). The log-log slopes (ζ_q) were calculated by a least-squares fit, as displayed in Figure 3.8 (middle). The dashed curve in Figure 3.8 (left bottom) is

calculated by an empirical two-parameter function introduced by Pierrehumbert (1996) which is as follows

$$\zeta_q = \frac{aq}{1 + a\frac{q}{\zeta_\infty}}. \tag{3.25}$$

The parameters a and ζ_∞ are evaluated by requiring Equation 3.25 to match the data exactly at $q = 1$ and $q = 5$. The coefficient $a \approx \zeta_1$ measures smoothness and $1/\zeta_\infty$ measures multifractality or intermittency. $1/\zeta_\infty \to 0$ represents simple scaling, with increasing values of $1/\zeta_\infty$ corresponding to larger probabilities that the field contains jump discontinuities (Pierrehumbert, 1996; Lewis et al., 2004).

In principle, the concavity of the function ζ_q (see Figure 3.8 bottom) is a characteristic of the intermittency, the more concave the curve is, the more intermittent the process (Calif and Schmitt, 2012). Intermittency describes the tendency of passive tracers to concentrate in localised, intermittent structures (Shraiman and Siggia, 2000; Tuck et al., 2003). Calif and Schmitt (2012) define intermittency as the property of having large fluctuations at all scales, with a correlated structure. By calculating the intermittency of the two humidity time series of Figure 3.8 (top) we find $1/\zeta_\infty = 0.37$ at 2.4 km, and $1/\zeta_\infty = 0.06$ at 4.1 km. The former indicates strong and the latter weak intermittency, confirming the visual impression from Figure 3.8 (top).

3.4 Summary and discussion

The data set underlying the thesis at hand is derived from DIAL water vapour observations and COSMO-DE model simulation data, whereas the lidar data is primary source. In the last years, the fast-moving development of the DIAL remote sensing technique has made it possible to install the DIAL on an airplane collecting tropospheric water vapour profiles with high vertical and horizontal resolution and high accuracy. Within the last two decades, the numerical weather models were substantially improved in regard to their resolution leading to cloud-resolving and better convection-permitting simulations. This breeds the question, how well the high-resolution COSMO-DE model reproduces the atmospheric water vapour variability. For purposes of this thesis, data sets of DIAL water vapour observations and modelled water vapour fields are used to analyse the height-resolved spatial variability from horizontal scales of 100 km down to about 10 km for the first time by means of structure functions.

Chapter 3 Data and methodology

The observed and modeled water vapour fields analysed in this thesis indicate scale invariance and intermittency. The focus of the discussion in the following chapters is on the first-order scaling exponent ζ_1 for two reasons. First, the first-order structure function is more robust than higher order structure functions with respect to outliers in the increment $|f(x_i + r) - f(x_i)|$. Second, the first-order structure function allows for scaling relations that are naturally connected to the Hurst exponent H in the theory of turbulence which aids the physical interpretation.

Under the assumptions of stationarity and monofractality, the second order scaling exponent can be related to the slope of the Fourier power spectrum. In literature, scaling exponents from the second-order or the power spectrum are often used to explore scale-invariance of atmospheric variables over a range of scales, but the single scaling exponent is only sufficient for monofractal fields. Many atmospheric fields are known to be multifractal or, synonymously, are said to exhibit anomalous scaling, i.e., the scaling exponents of increasing orders have a nonlinear relationship. This strengthens the needfulness of a clear description of higher-order structure functions. For the sake of completeness and to permit comparisons with previous studies, the second-order structure function scaling exponent of water vapour is included in this thesis.

Further, this thesis focuses also on the investigation of anomalous scaling behaviour of the tropospheric water vapour field concerning the intermittency measure $1/\zeta_\infty$, i.e., the deviation of the scaling exponents of higher order structure functions from linear behavior with increasing order q (Pierrehumbert, 1996). This value provides a compact proxy for the evolution of the scaling exponents of structure functions of orders higher than three.

Chapter 4

Height-resolved scaling exponent statistics of water vapour variability

In this chapter, structure function analysis of a unique tropospheric water vapour data set obtained from airborne lidar is presented for the first time. Section 4.1 is to introductorily provide a short literature review of the relevant aircraft studies based on one-dimensional in situ measurements, that investigate the water vapour variability on spatial scales smaller than 100 km by means of power spectra or structure functions (with exception of Nastrom et al. (1986)). The subsequent analysis of two-dimensional lidar observations with a unique vertical resolution of about 150 m, collected during the COPS/ETReC campaign in 2007, provides a height-dependent scaling exponent statistic (see Section 4.2) that allows to relate the observed exponents to the meteorological conditions at different levels in the atmosphere (see Section 4.3).

4.1 Introduction

The research of dynamical tracers in the atmosphere is essential for gaining the required information for a better understanding of the physical processes which link small-scale motions with large-scale circulation. The power spectrum or the structure function method are suitable to study the relationship between the scale-resolved variance and the atmospheric circulation and structure (Nastrom et al., 1985; Lu and Koch, 2008), i.e., different power-law exponents or scaling behaviours indicate different predominant physical processes.

Table 4.1: Average second-order scaling exponents $\zeta_2 = \beta - 1$ of the second-order structure function of moisture time series measured during aircraft studies as a function of height h.

	Nastrom et al. (1986)	Cho et al. (1999)	Cho et al. (2000)	Kahn et al. (2011)	COPS data
Scaling	150 - 500 km	6 - 60 km	0.05 - 100 km	10 - 100 km	10 - 100 km
h < 1.5		0.94	0.46 ± 0.13	0.58	
h < 3.0				0.80	0.63 ± 0.17
h > 3.0		0.90	0.79 ± 0.17	0.90	0.81 ± 0.31
h >10.0	0.66				

Scale dependencies of the water vapour variability in the free troposphere, expressed by power-law exponents, have so far been investigated in the course of only four aircraft studies (Nastrom et al., 1986; Cho et al., 1999 and 2000; Kahn et al., 2011). In each of these studies the analysis is based on in situ measurements, i.e. measuring only one height for predefined flight segment. Table 4.1 shows the average results obtained for each of these studies, with their standard deviations where available. With the exception of the study from Nastrom et al. (1986), all aircraft in situ measurements allow for investigating the variability on horizontal spatial scales smaller than 100 km, thereby including small-scale convective currents.

Nastrom et al. (1986) obtained an averaged variance power spectrum with a slope ($k^{-\beta}$) of $\beta = 5/3 = \zeta_2 + 1$ in the upper troposphere. While Cho et al. (1999) found a wide range of scaling exponent values throughout the troposphere, Cho et al. (2000) separated the atmosphere into three different regimes - marine boundary layer (a), tropical free troposphere (b), and extratropical free troposphere (c) - and obtained different spectral slopes (a: $\beta = 1.46$, b: $\beta = 1.63$, c: $\beta = 1.79$) for each of these predefined regimes. By using structure functions of higher orders Cho et al. (2000) further found that the tropical free troposphere has a more intermittent water vapour field than the extratropical free troposphere. Kahn et al. (2011) further detected increasing spectral slopes with height, finding a minimum of $\beta = 1.58$ at a height of 1.5 km and a maximum of $\beta = 1.90$ at heights above 3 km.

The layer-averaged results of scaling exponents (see Table 4.1) confirm a high vertical variability of the water vapour field but do not allow for further assumptions on the physical processes responsible for the observed variability.

While Table 4.1 indicates that the water vapour variability changes with height, a clear tendency can not be obtained. Over all studies, the layer-averaged scaling exponents vary from $\beta = 1.46$ up to $\beta = 1.98$. In detail, the three studies that investigated water vapour variability up to a horizontal range of 100 km have a tendency of increasing exponents with increasing height. It is worth mentioning, that the spectral analysis made in the study of Nastrom et al. (1986) includes also stratospheric regions, where water vapour is a conservative tracer. Further, the examined spatial scales of Nastrom et al. (1986) are much larger than for the other studies. In addition, the slope of the spectra is based on a comparison to reference spectra rather than explicitly computed scaling exponents. As such the results of Nastrom et al. (1986) should be handled with care when comparing them to the other studies. Nevertheless, the range of values shown in Table 4.1 suggests that different mechanisms influence the water vapour variance in the underlying data sets. Slopes steeper than $\beta = 5/3$ suggest the importance of downscale transfers of scalar variance, while a slope of $\beta = 5/3$ could also be a consequence of upscale transfers. Identifying the physical mechanisms responsible for the statistics of water vapour variability in different parts of the atmosphere is a key factor for improving parameterisations of cloud processes, but is complicated due to the lack of available high-resolution data.

4.2 Height dependency of scaling exponents

The COPS data set

In contrast to the in situ measurements, airborne DIAL data sets provides water vapour profiles with a vertical resolution of 150 m, leading to a unique height-resolved scaling exponent statistic. The data set, investigated in the course of this study, were collected by means of 8 flights during the COPS/ETReC field experiment, conducted from June to August 2007. The DLR Falcon plane flew over middle and south-west Europe, between 41°N - 49°N and 7.5°W - 10°E. Six of the 14 flights of this campaign had to be removed due to low lidar signals or large data gaps caused by clouds, aircraft turns or lidar adjustment phases. After

performing a horizontal averaging to a resolution of 2-3 km in order to obtain a high signal to noise ratio, and linear interpolation over small data gaps, flights with a length between 225 km to 700 km and a vertical extent from 2.0 km to 9.8 km could be analysed, the majority of flight segments showing a length of about 300 km and a vertical range of about 4 km. The signal to noise ratio was subsequently estimated by using a lagged autocorrelation method to seperate instrumental noise from atmospheric variability (Kiemle et al., 1997). The average statistical uncertainty over all 8 flights is about 3 % and shows no systematic height dependency, since the usual lidar signal decreasing with range is compensated here by aerosol and water vapour densities that increase towards the ground. Given the vertical DIAL resolution of 150 m, a total of 98 time series were analysed using the structure function method, corresponding to a total length of about 38 000 km.

Results of the COPS data set

In a first step, the second-order scaling exponents ζ_2 of the COPS data set, which can be related to the slope of the power spectrum β by computing $\zeta_2 = \beta - 1$ (see also Chapter 3), were presently layer-averaged (see Table 4.1). The averaged exponents below and above a height of 3 km are $\zeta_2 = 0.63$ and $\zeta_2 = 0.81$, respectively. This result is broadly consistent with the earlier studies of Cho et al. (2000) and Kahn et al. (2011). However, the present data set, collected by airborne lidar, allows for investigating the vertical variability in more detail, i.e., the vertical analysis is performed based on steps of 150 m. Therefore, an unique height-resolved statistical characterisation of water vapour variability, based on the calculation of structure functions up to the fifth order, is presented and an attempt is made to relate the obtained results to the meteorological conditions at different height levels in the atmosphere.

First- and second-order structure function scaling exponents ζ_1 and ζ_2 have been calculated for the 98 moisture time series described above. Figure 4.1 shows the values of ζ_2 plotted against height. The exponent derived therefrom varies from $\zeta_2 = 0.29 \pm 0.10$ to $\zeta_2 = 1.68 \pm 0.10$, with a tendency towards higher values at higher heights. The individual uncertainties vary between ± 0.05 and ± 0.15 and show no height dependency. As listed in Table 4.1, the few existing aircraft studies on water vapour scale dependence have found average scaling exponents ζ_2 ranging from 0.46 to 0.94 (Nastrom et al., 1986; Cho et al., 1999 and 2000; Kahn

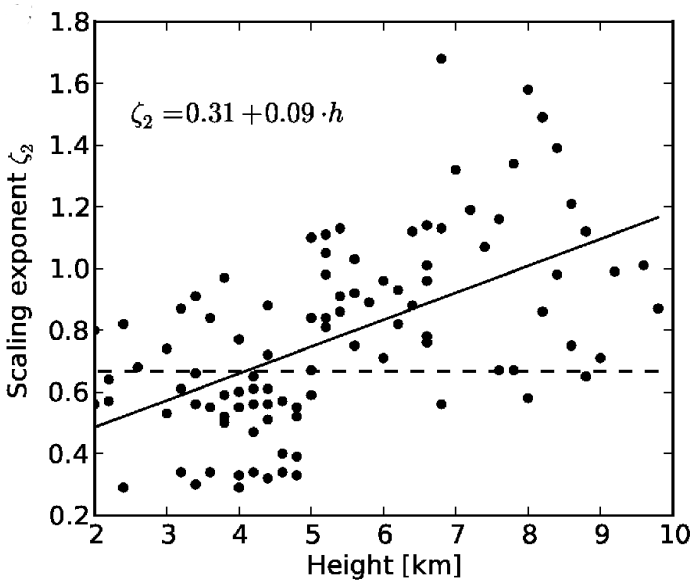

Figure 4.1: Scaling exponent ζ_2 versus height for 98 segments from eight flights during the COPS campaign. The solid line is computed by a least-squares regression with a fit parameter uncertainty of 0.013; the dashed line represents $\beta = 5/3$.

et al., 2011). However, the high vertical resolution ($\sim$ 150 m) of the presently analysed DIAL observations allows for a more detailed analysis of the scale dependence of the water vapour field throughout the troposphere. Figure 4.1 shows increasing exponents with increasing height. Further, a jump is seen at a height of about 5 km, with lower exponent values ζ_2 beneath the 5 km height. Interestingly the values in the lower levels scatter around the theoretical $\beta = 5/3$ or $\zeta_2 = 2/3$ predicted for homogeneous turbulence or alternatively upscale transfer from convection, while the slope at upper levels is steeper, suggesting a downscale influence. Based on these results, it could be assumed that different physical processes are responsible for different scaling regimes. In the following section, a hypothesis therefore is introduced that makes the testing of the physical background processes of the detected scale dependence regimes in the water vapour field over horizontal spatial scales from 10 km to 100 km possible.

4.3 Hypothesis: Air mass dependency of scaling exponents

In principle, a spectral slope of $\beta = 5/3$ is predicted by the classical Obukhov-Corrsin theory of three-dimensional homogeneous turbulence (Corrsin, 1951) for both kinetic energy and the variance of a passive tracer (e.g., water vapour in the absence of clouds). This is, however, not likely to be a correct description of the atmosphere on scales of tens or hundreds of kilometres as water vapour is interacting with atmospheric motions in various ways. Sherwood et al. (2010) for example illustrated the non-passive scalar behaviour of water vapour based on its role in large-scale latent heat transport, its influence on radiative impact and its enhancement of vertical motions through latent heat release. A $\beta = 5/3$ slope in kinetic energy may also occur through gravity waves, or through upscale transfer from a small-scale source of variance such as cumulus convection (Vallis et al., 1996; Xu et al., 2011; Waite and Snyder, 2012), but the link of these processes to the spectral slope of water vapour is still not sufficiently explored.

In the present study, the two dimensional lidar cross sections provide valuable additional information. On 1 August in 2007 for example, for the time series shown in Figure 4.2 (top left), a warm, moist air mass of Mediterranean origin was found below a height of 5 km $\pm$ 1 km. The boundary between this air mass and the air above is clearly visible in the lidar backscatter ratio (Figure 4.2 bottom). As seen in the backscatter and humidity cross sections in Figure 4.2, moist convection occurred in numerous times and places in the lower level air mass, penetrating to a stable layer at its upper boundary. Above the boundary, air of Atlantic origin can be found that shows substantially less small-scale variability, which is consistent with the observed steeper spectral slope of humidity variance. This pattern of two layers occurred frequently during the period of the COPS campaign, and has been examined in detail for the 1 August 2007 case study by Schäfler et al. (2010). As an alternative to examining the change in structure functions with geometric height, the time series may further be classified into two groups, depending on whether or not they occured in an air mass influenced by cumulus convection. The classification was performed by determining the cloud top height from the lidar backscatter signal of the corresponding flight (see examplary case in Figure 4.2). The relevant time series were assigned to the convectively influenced category (R_{conv}) if located below that height, and to

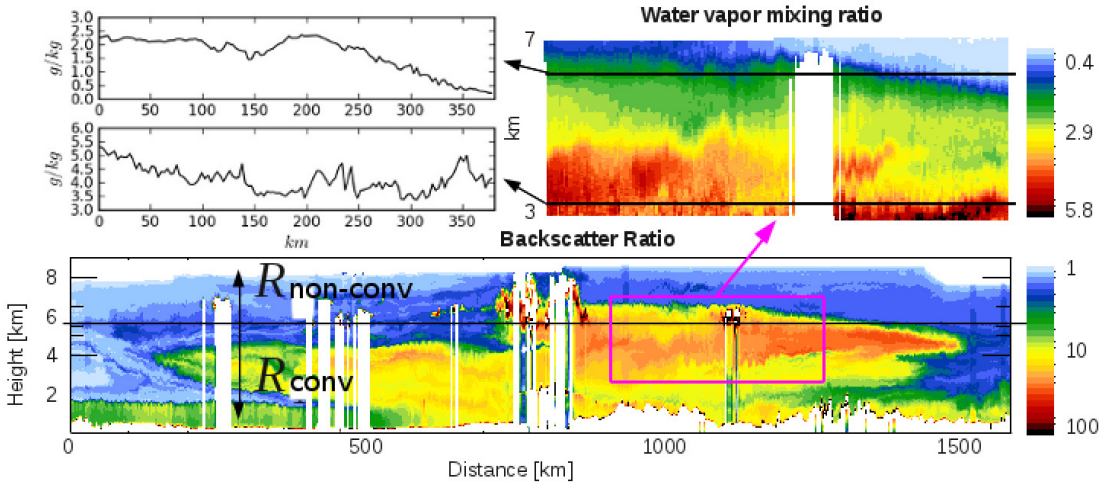

Figure 4.2: (top left) Representative specific humidity data samples from 1 August 2007 at 6.0 km (top) and at 3.2 km height (bottom); and lidar measurements of (top right) specific humidity (g/kg) for the analyzed 370 km flight segment; and (bottom) atmospheric backscatter ratio at 1064 nm wavelength for the whole flight. The black horizontal line at 5.7 km height marks the level of cloud base. R_{conv} and $R_{non-conv}$ indicate the two air mass regimes defined in Section 4.3.

the second category ($R_{non-conv}$) if located above. By applying this procedure, a number of 43 time series was assigned to R_{conv}, and 55 time series to $R_{non-conv}$. As shown in Table 4.2, the boundary between the two regimes occurred between 4 and 6 km in height during the COPS experiment. Table 4.2 shows first- and second-order scaling exponents (ζ_1 and ζ_2) for the two regimes for each of the 8 flights (note that both regimes were present in the same flight segment for only half of the flights.) R_{conv} indicates height levels with dominating moist convective influences, $R_{non-conv}$ indicates height levels with dry and cloud free air masses likely advected by the large-scale flow. L is the length of the time series, N is the number of time series. The average Hurst exponent for the convective regime R_{conv}, $\zeta_1 = 0.36$, is smaller than for the non-convective regime $R_{non-conv}$, where it takes the value $\zeta_1 = 0.53$. This indicates that the humidity time series at lower, more convective levels are rougher and have longer range correlations (Tuck et al., 2003) than at higher heights. The two timeseries at heights of 3.2 km (bottom) and 6.0 km (top), shown as an example in Figure 4.2 (top left), clearly display these differences in smoothness.

The difference in the second-order structure function exponent ζ_2 between the two regimes shows up clearly, with average values of $\zeta_2 = 0.61$ in the convectively-influenced region R_{conv}, and $\zeta_2 = 0.97$ in $R_{non-conv}$. The value in R_{conv} is close

Table 4.2: Characteristics and statistical properties of the two regimes R_{conv} and $R_{non-conv}$ found in the dataset of the COPS campaign in 2007.

R_{conv}	L [km]	h [km]	N	ζ_1	ζ_2	$1/\zeta_\infty$
18.07.	225	3.4 - 4.8	5	0.41	0.72	0.57
19.07.	250	3.2 - 4.6	6	0.27	0.49	0.58
20.07.	340	3.0 - 5.0	9	0.35	0.64	0.29
26.07.	360	2.0 - 2.4	3	0.31	0.57	0.49
30.07.	500	2.0 - 4.0	8	0.33	0.58	0.43
01.08.	370	3.2 - 5.6	12	0.39	0.66	0.57
Averages				0.36 ± 0.11	0.61 ± 0.19	0.49 ± 0.42
$R_{non-conv}$	L [km]	h [km]	N	ζ_1	ζ_2	$1/\zeta_\infty$
08.07. I	700	6.6 - 9.8	15	0.65	1.19	0.15
08.07. II	300	4.2 - 6.0	10	0.47	0.86	0.22
18.07.	225	5.0 - 6.6	3	0.56	0.98	0.22
19.07.	250	4.8 - 9.0	16	0.40	0.75	0.22
20.07.	340	5.2 - 5.8	3	0.57	1.05	0.12
01.08.	370	5.8 - 7.0	8	0.55	1.01	0.16
Averages				0.53 ± 0.15	0.97 ± 0.25	0.18 ± 0.12

to the classical value of 2/3, corresponding to a spectral slope of $\beta = 5/3$, while the larger value in $R_{non-conv}$ corresponds to a steeper slope.

Structure functions of higher orders are necessary in order to fully characterise nonstationary time series. The intermittency can be calculated from the variation of the scaling exponents ζ_q with q (see Figure 4.3). In this study, intermittency is calculated by the empirical two-parameter function introduced by Pierrehumbert (1996). By calculating the intermittency of the two humidity time series of Figure 4.2 (top left) we find $1/\zeta_\infty = 0.43$ at 3.2 km, and $1/\zeta_\infty = 0.13$ at 6.0 km. The former indicates strong and the latter weak intermittency, confirming the visual impression from Figure 4.2 (top left). Increasing intermittency values correspond to larger probabilities that the field contains jump discontinuities.

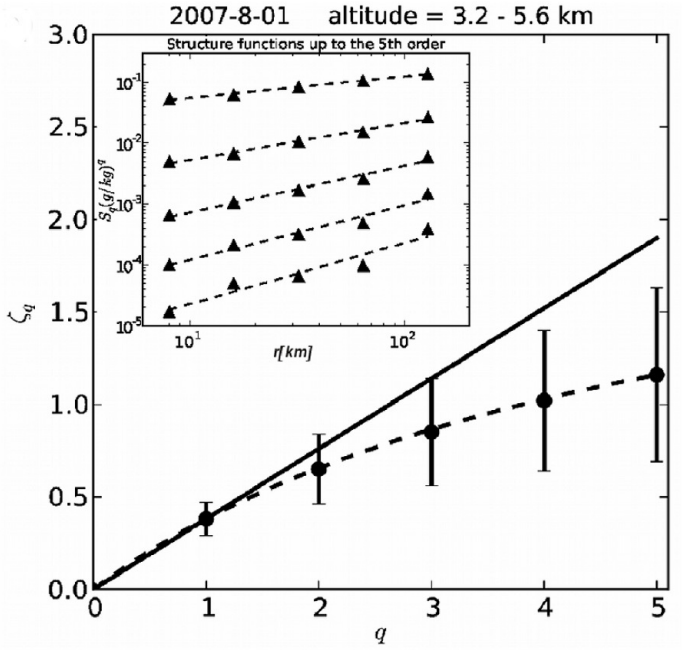

Figure 4.3: Structure functions up to the fifth order at 3.2 km height (inset). The order increases in unity steps from top to bottom. Straight lines are fitted to the structure functions from $r = 8$ km to $r = 120$ km (triangles). The average slopes calculated from the fits are plotted versus order q for twelve 370 km flight segments from 3.2 – 5.6 km height (main). The dashed curve is calculated by the parameterisation of Pierrehumbert (1996). The error bars are the standard deviations; the solid line represents hypothetical monofractal behaviour for comparison.

Values of $1/\zeta_\infty$ for the complete data set are listed in Table 4.2, and again show a clear difference between the two regimes R_{conv} and $R_{non-conv}$. R_{conv} is characterised by higher values and thus higher intermittency than $R_{non-conv}$ (0.49 vs. 0.18). The mean of $1/\zeta_\infty$ for R_{conv} of 0.49 lies around the value calculated for the tropical troposphere (0.43) by Cho et al. (2000), while the mean for $R_{non-conv}$ is lower than the value calculated for the extratropical troposphere (0.21) by Cho et al. (2000). A more precise comparison is difficult, since the values provided by Cho et al. (2000) are averaged throughout the free troposphere.

4.4 Summary and discussion

In order to characterise the variability of tropospheric humidity, airborne DIAL water vapour measurements gained from eight flights on seven days of the COPS experiment have been analysed. The structure functions, calculated for the 98 time series of tropospheric water vapour showed power law scaling between hor-

izontal spatial scales of about 10 km to 100 km. The scaling exponents (ζ_1 and ζ_2) and intermittency values ($1/\zeta_\infty$) are significantly dependent on height with a tendency of increasing scaling exponents respectively decreasing intermittency at increasing heights.

Using the additional information of two dimensional lidar backscatter cross sections, the change in variability statistics could be associated to an air mass boundary separating low-level air where cumulus convection was occurring from higher-level air above the convective cloud tops. The convectively influenced air masses, present at some level in five of the eight flights, showed consistently shallower spectral slope (smaller ζ_2), greater roughness (smaller Hurst exponent ζ_1), and significantly higher intermittency (departure from mono-fractality shown by larger $1/\zeta_\infty$).

The value of the second-order structure function in the convective regime, $\zeta_2 = 0.61$ is consistent with the classical $\beta = 5/3$ spectral slope. Mechanisms for producing this slope have been proposed based on both downscale cascade of tracer variance and upscale transfers from a small-scale source such as convection. The higher order structure functions presented here, as well as the subjective classification of time series based on the presence of convection, provide strong evidence for a small-scale source of moisture variability. Note however that the analysis does not exclude the presence of downscale transfers of variance. On the other hand, theories for the steeper spectral slope found above the convectively-influenced air masses all rely on downscale transfers.

It is probably not significant that the air mass boundary during the aircraft deployment in July 2007 consistently occurred at a height of around 5 km, and it will be interesting to compare this period with other data sets. Provided that the two regimes are taken into account, it appears that the structure function exponents supply a compact statistical description of moisture variability on scales just below the resolution of weather and climate models. The universality of the two regimes will be proven in Chapter 5 of this thesis with regard to a wider geographical and seasonal extent.

Chapter 5

Air mass dependency of scaling exponents and vertical correlation in the water vapour field

5.1 Introduction

This chapter focuses on the particular strengths of airborne lidar data, namely the high horizontal and vertical resolution, to characterise the scaling behaviour of water vapour in different air masses. The preliminary results of Fischer et al. (2012) (please refer to Chapter 4) who identified different scaling laws for convective and non-convective air masses sampled during a field campaign over western Europe in summertime, are consequently extended. The analysis is enlarged by including data from sub-tropical and polar regions in autumn and winter respectively. This increases the total amount of data by a factor of five, but more importantly, samples different atmospheric regimes. The conclusion of Chapter 4, i.e., that the scaling exponents derived from the water vapour structure functions as well as the intermittency show two regimes (convective and non-convective), often separated by a sharp boundary in height, will be re-assessed and tested by means of this larger data set. Thereby the primary scientific objective will be to determine whether these two regimes are universal, or whether additional or diverse behaviours are found for other meteorological situations. A preliminary analysis of vertical correlations for two flight segments will additionally be presented, in order to test the hypothesis if vertically coherent injections of moisture

in convective air masses will lead to stronger vertical correlations than those found in non-convective air masses where advection shears out vertical structures.

After giving an overview on the airborne lidar data set in Section 5.2, which includes details on the signal processing and the three flight campaigns, several meteorological situations will be discussed by means of two dimensional water vapour cross sections in Section 5.3. The results received from analysing the three campaigns in different regions of the world and at different times of the year are subsequently presented in Section 5.4. Section 5.5 presents a height-correlation analysis of airborne lidar observations. Finally, the results of the three campaigns are discussed and conclusions are stated in Section 5.6.

5.2 Water vapour data sets from three campaigns

The water vapour data sets analysed in this chapter have been derived from three campaigns (COPS/ETReC midlatitude summer, T-PARC subtropical autumn and IPY-THORPEX polar winter), and were generated by the WALES DIAL which was installed nadir-viewing on board the DLR Falcon research aircraft. The details of the DIAL measurements including the signal processing are explained in the following.

Signal processing

While the basic principles of airborne DIAL are explained in Chapter 3, this section provides further details on the signal processing of the observations. The data sets are collected 600 m below the aircraft where full overlap between the laser beam and the telesope field of view is given. Spectral impurity of the laser (Wirth et al., 2009) is corrected taking advantage of all three on-line wavelength return signals. Profiles with ambiguous results between the different on-line signals or with unstable laser operation, which is monitored and recorded together with the data, were discarded at this stage. Before calculating the humidity profiles from the DIAL equation (see also Chapter 3), uncorrelated instrumental noise was reduced by averaging the returned on- and off-line signals. In this study, measurements are horizontally averaged to a length of 2-7 km. Due to the fact that the DIAL cannot perform measurements under optically thick clouds, small data gaps had to be filled by linear interpolation. The resulting data set

Table 5.1: Overview of the three campaigns COPS/ETReC, T-PARC and IPY-THORPEX.

	COPS/ ETReC	**T-PARC**	**IPY-THORPEX**	**Total**
Lat/Lon	41-49°N/ 7.5°W-10°E	24-40°N/ 129-152°E	53-81°N/ 2-25°E	
Date	8.7. - 1.8.07	1.9. - 1.10.08	25.2. - 17.3.08	
Number of flights	7	6	7	20
Segments	97	265	160	522
Height range	2.0 - 9.8 km	2.0 - 10.4 km	1.5 - 9.3 km	
Segment length	225-700 km	350-1300 km	330-800 km	
Total length of time series [km]	44,560	190,560	134,010	369,130

comprises 20 flights with lengths ranging from 225 km to 1300 km. The DIAL equation is applied with an effective vertical resolution of 150 m and the vertical range of water vapour profiles starts from 1.5 km up to a maximum of 10.4 km of height. Considering all levels of all flights, we analysed 522 water vapour time series with a total length of about 370,000 km throughout the troposphere (see also Table 5.1). The measurements of specific humidity are of high accuracy, with errors expected to be less than 5-7 % (Bhawar et al., 2010).

In principle, the signal quality decreases with increasing distance from the aircraft. By using the lagged autocorrelation method (Kiemle et al, 1997; Lenschow et al., 2000) by which fictitious variance can be separated from natural variance, we have found that the signal quality decrease is almost fully compensated by increasing water vapour and aerosol densities in the analysed vertical range between 1.5 km and 10.4 km of height, as observed in earlier studies (cf. Kiemle et al., 2011). On average the statistical uncertainty caused by uncorrelated instrumental noise lies around 5% for all 20 flights and shows only a weak height dependency.

During the COPS/ETReC flights only three out of four possible wavelengths could be used for water vapour measurements (Schäfler, 2011). In contrast, during T-PARC and T-IPY the WALES demonstrator was fully functional and operated at four wavelengths.

Chapter 5 Air mass dependency of scaling exponents and vertical correlation in the water vapour field

COPS/ETReC 2007 midlatitude summer

The aim of the Convective and Orographically-induced Precipitation Study (COPS), which took place in summer 2007 in middle and southwest Europe, was to improve the skill to forecast convective precipitation over complex mountainous terrain in the summer season (Wulfmeyer et al., 2011). Therefore, the influence of small-scale inhomogeneities of humidity, temperature and wind on convection initiation was observed and investigated. For this study, we use the water vapour measurements performed during flights of the DLR Falcon equipped with nadir-pointing water vapour lidar (see also Kiemle et al., 2011). The 7 flights analysed in this study, were performed over Germany, France and Spain in the period from 8 July to 1 August 2007 (see also Figure 5.1). The typical weather situations during the campaign included cases with surface forced convection in high pressure air masses and synoptically forced convection in warm advected air masses ahead of an upper-level trough.

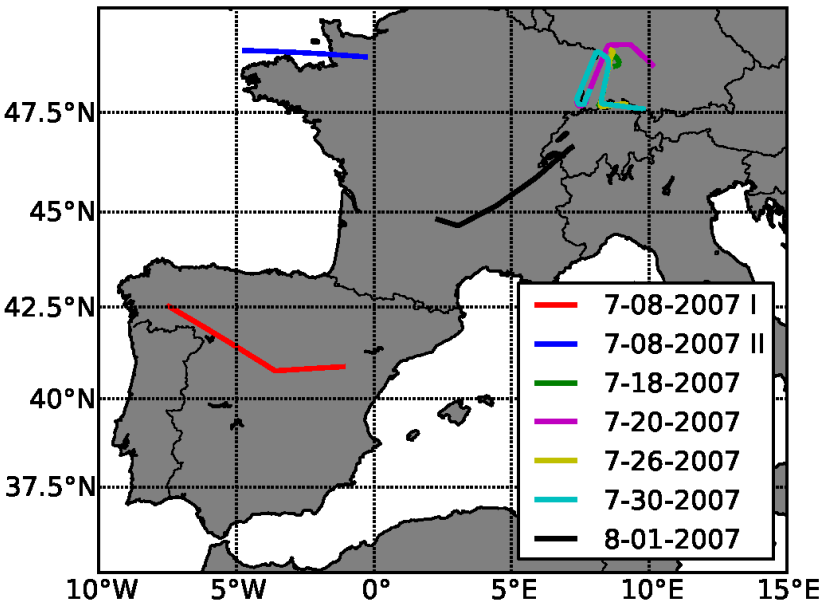

Figure 5.1: DLR Falcon flight paths of the analysed segments of the COPS/ETReC campaign in 2007.

IPY-THORPEX 2008 polar winter

The 3-week Norwegian IPY-THORPEX campaign which was part of the International Polar Year (IPY) took place between 25 February and 17 March 2008

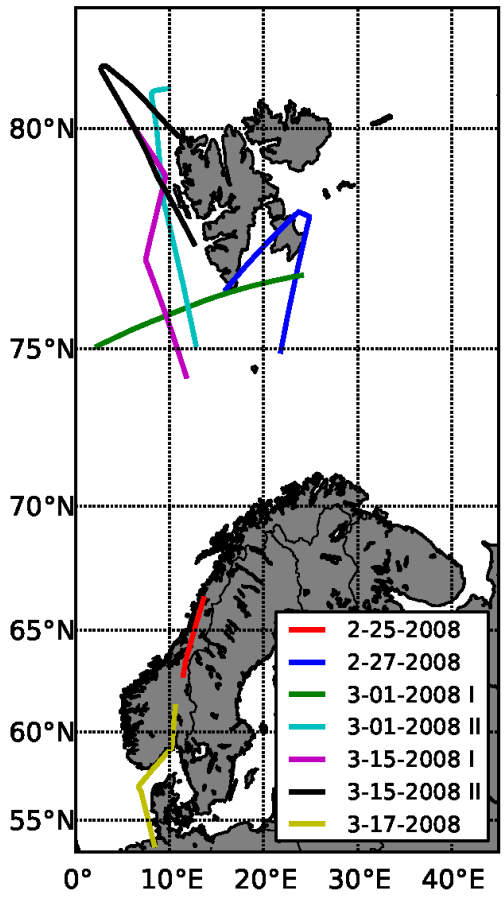

Figure 5.2: DLR Falcon flight paths of the analysed segments of the IPY-THORPEX campaign in 2008.

with the DLR Falcon as the main measurement platform of the field campaign (see also Wagner et al., 2011). The majority of flights took place over Scandinavia and near Spitzbergen (see Figure 5.2). The aim of this campaign was to yield detailed observations of polar lows, Arctic fronts and orographic low-level jets near Spitzbergen, the coast of northern Norway and the east of Greenland (Kristjansson et al., 2011). In particular, the DIAL system on board the DLR Falcon served for investigations of Arctic humidity structures. The 7 analysed flight segments with 160 time series have a total length of 134,010 km and cover a vertical range from 1.5 km to 9.3 km (see also Table 5.1).

T-PARC 2008 subtropical summer

During the THORPEX (The Observing System Research and Predictability Ex-

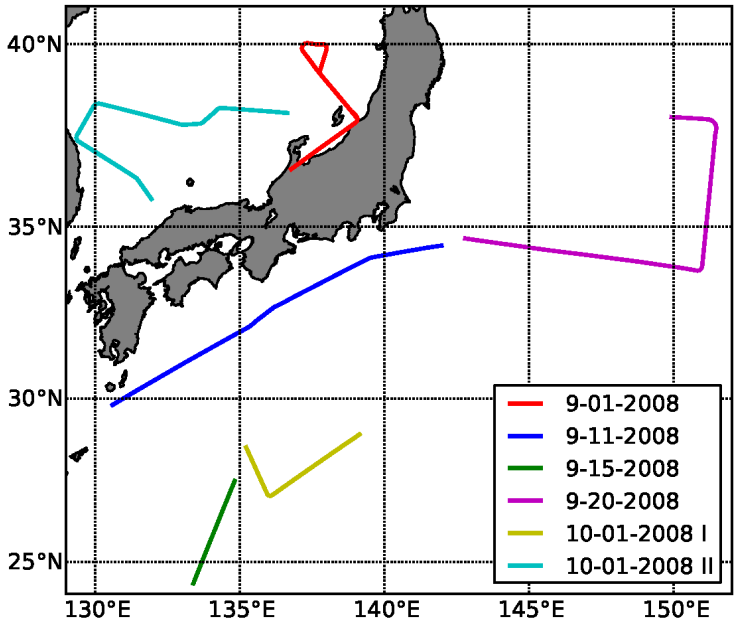

Figure 5.3: DLR Falcon flight paths of the analysed segments of the T-PARC campaign in 2008.

periment) Pacific Asian Regional Campaign (T-PARC), which took place in the area of the western North Pacific basin during the period from August to October 2008, the WALES demonstrator collected a unique set of water vapour profiles (see also Harnisch et al., 2011). T-PARC focused on various aspects of typhoon activity, including formation, intensification, structure change, motion and extra-tropical transition. During the period 26 August to 1 October 2008 a number of 25 research flights was undertaken. However, most of the flights either focused on tropical air masses or suffered from high cloud coverage which prevented a substantial amount of DIAL observations. Therefore, only six flights (Figure 5.3) with largest horizontal and vertical observational coverage were selected for the present study, i.e., representing 267 time series with a total length of 173,480 km and a vertical range from 2 km to 10.4 km (see Table 5.1).

5.3 Factors influencing the scaling exponents

The two-dimensional water vapour lidar cross sections of 20 flights collected in different regions of the world and during different seasons of the year represent a multitude of meteorological weather situations. The complex dynamics of water vapour in the troposphere are linked to the weather situations in terms of

source and sink processes from convective clouds on the kilometre scale to cloud systems associated with motions on scales of thousand or more kilometres, as well as advection of water vapour as a passive tracer outside of clouds (Emanuel and Pierrehumbert, 1996). In Figure 5.4 a variety of tropospheric water vapour structures can be seen in the two-dimensional water vapour scans made by the DIAL on board the DLR Falcon. Figure 5.4 (a) shows a very dry polar air mass with a shallow convective layer underneath a stable stratified troposphere. In contrast, the water vapour cross section in Figure 5.4 (b) shows the influence of a tropical cyclone, with large and variable moisture content throughout the troposphere. Figure 5.4 (c) was observed in midlatitude summer over land, and shows large, vertically coherent moisture anomalies. A final example is shown in Figure 5.4 (d), where a filament of dry air extends from the upper troposphere to the boundary layer in a subtropical region. Such a large range of behaviours is not surprising given the various latitudes, seasons and orographic conditions of the field campaigns where the measurements were performed. The large data set allows to re-examine the conclusion of Chapter 4 that there is a clear distinction of the scaling exponents between air masses with and without convective clouds as well as to analyse the possibility that other differences and influences between the campaigns could have an equal or even more decisive impact on the analysis of tropospheric water vapour variability. Further, Figure 5.4 shows highly variable water vapour fields characterised by fluctuations differing in spatial occurence and amplitude. Such fluctuations are called intermittent (Dotzek and Gierens, 2008) and can be quantified by using structure functions up to the fifth order. In the broader sense, assumptions on possible local physical processes that arise fluctuations in the water vapour field are consequently made.

5.4 Distribution of scaling exponents

In a first step, air masses are classified into convective or non-convective categories using the lidar backscatter intensity (Fischer et al., 2012). Therefore, the cloud top level is identified by using the off-line reference wavelength. In a second step, the observed water vapour time series are divided into two categories. One category contains all time series below and the other all time series above the top of the highest cloud (note that some lidar cross sections contain only one category). Figure 3.8 (top) shows typical examples of time series from each of

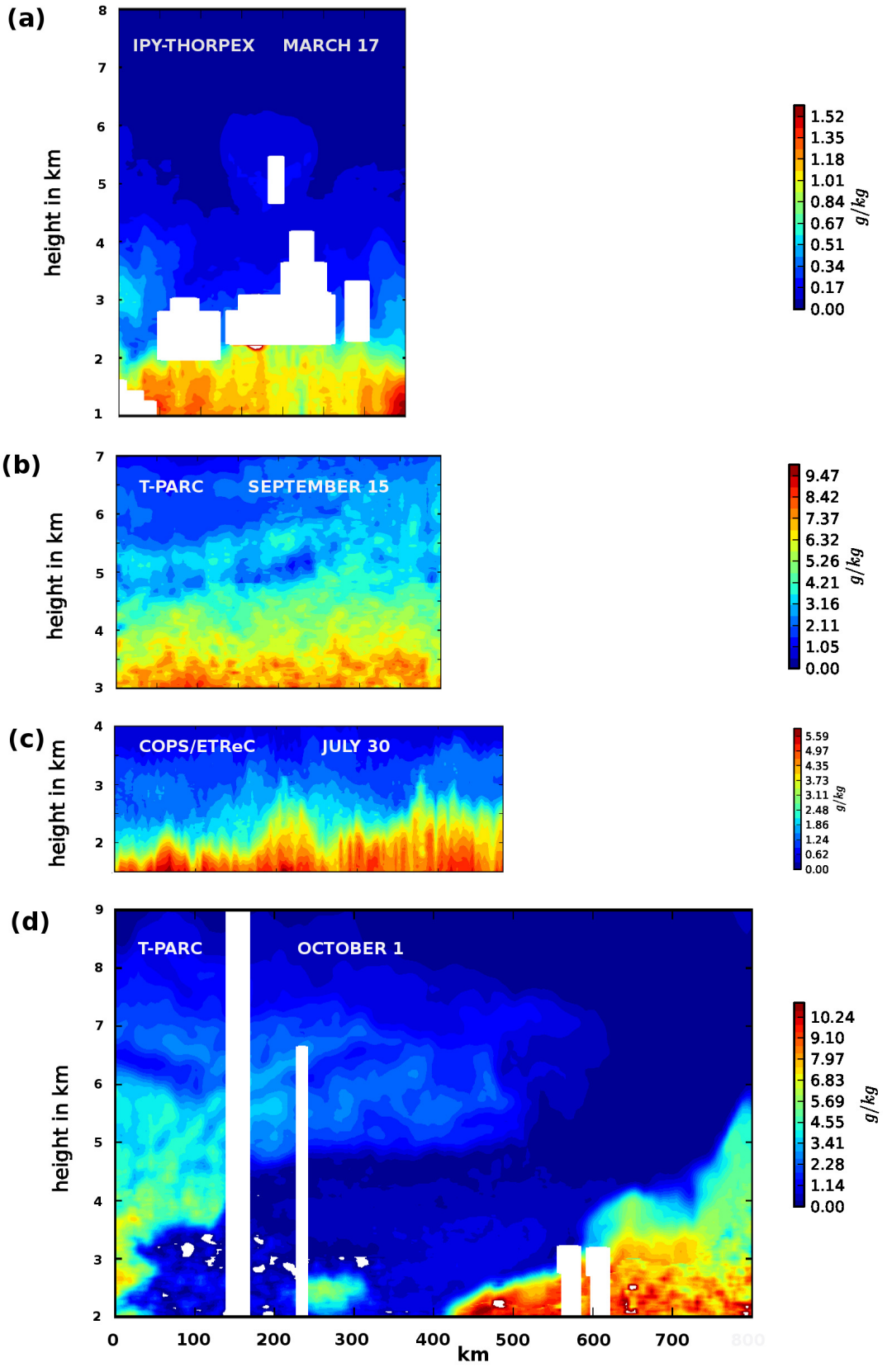

Figure 5.4: Lidar measurements of the water vapour field of four different flight segments from three campaigns.

the two regimes. The qualitatively different appearance of the two series in the top panels is confirmed by smaller scaling exponents and larger intermittency for the convective air mass (left panels). Note that the number of time series in non-convective air masses (411) is almost four times higher than in convective air masses (111) because the flight campaigns intentionally avoided cloudy regions and because the vertical range of convection is often much smaller than the vertical range of the non-convective air masses.

The distribution of values for the scaling exponent H (Hurst exponent) of the first order structure function over a range of scales from 5 km to 100 km is shown in Figure 5.5 (top). The x-axis shows the height relative to cloud top level where negative values stand for the convective layers and positive values for the layers above convection. In case of a clear sky, the surface height was used as the cloud top height. Figure 5.5 (top left) represents all scaling exponents in convective air masses, while Figure 5.5 (top right) plots all scaling exponents in non-convective air masses. The mean value in the convective regime, $H = 0.35 \pm 0.11$, is smaller than that of the non-convective regime, $H = 0.63 \pm 0.10$, i.e., the mesoscale variability of water vapour on horizontal scales from 5 km to 100 km is clearly different from the observed universal scaling law behaviour on larger scales (e.g., Nastrom et al., 1986). It can be hypothesised that the water vapour fluctuations in convective airmasses result from convective plumes and turbulent motions. Therefore, a smaller Hurst exponent as expression of a rougher water vapour field with higher small-scale variance can be expected. On the other hand, in free-tropospheric layers without convection, water vapour can be regarded as an advected, conservative tracer which leads to a drop off of small-scale humidity variance and thus steepens the spectrum and structure function slopes. The fact that the change in mean value occurs abruptly at the cloud top height is also significant. There is no evidence of a gradual transition in these high-resolution data sets. This supports the hypothesis that the different Hurst exponents are caused by different physical mechanisms.

Difference of means of two distributions

There is some overlap in the distributions between the two regimes, raising the question of whether the difference is statistically significant (Press et al., 2007). A difference of means can be very small compared to the standard deviation, and yet very significant, if the number of data points is large. Conversely, a difference

may be moderately large but not significant, if the data is sparse. The F-test and the Student T-test are calculated to decide if the mean values of both distributions are significantly different. Before the difference in means - using the Student's T-

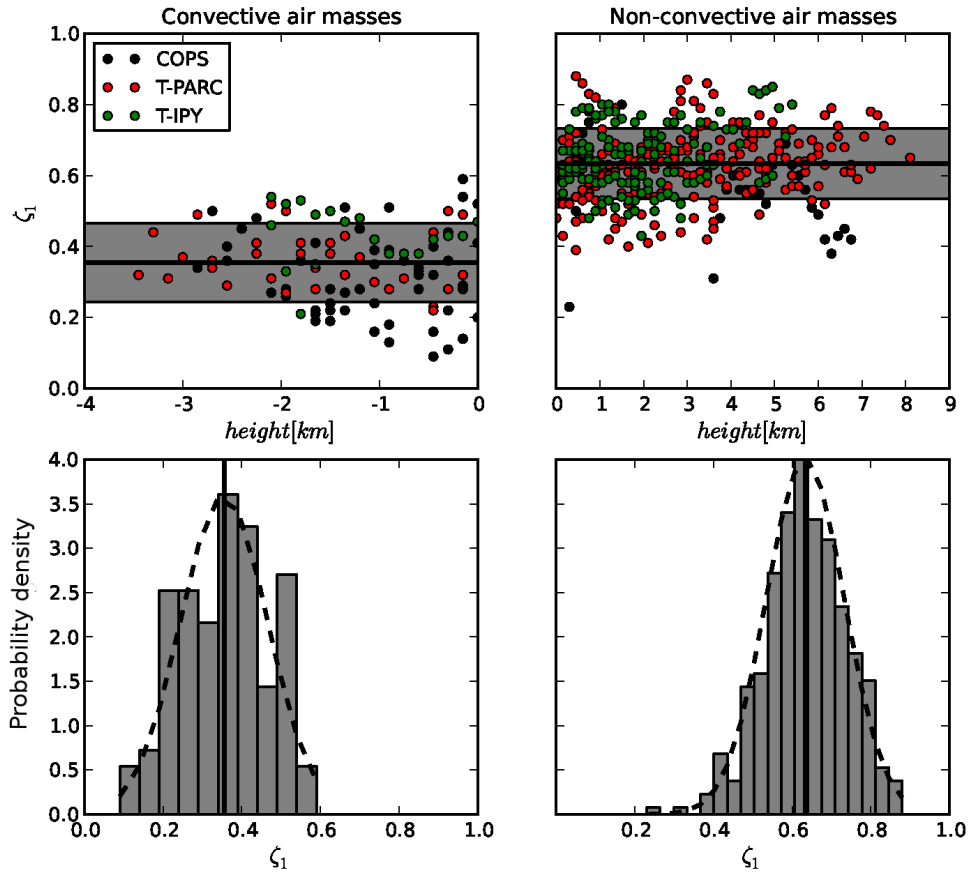

Figure 5.5: (Top) First-order scaling exponents of convective (left) and non-convective (right) time series of all three campaigns. The x-axis is the height relative to cloud top height. Horizontal line is the mean value with the standard deviation (shadowed area). (Bottom) The associated histograms for the two regimes. Vertical solid line is the mean value; dashed line is the fitted normal distribution.

test - can be started, a check, that the two distributions have the same variance, is essential. To find out whether the two data sets have significantly different variances the F-test was computed where the null hypothesis that their variances are actually consistent, is rejected. The statistic F is the ratio of one variance to the other, so values clearly larger or smaller than one will indicate significant differences. The F-test will provide two values, the calculated F-value and the p-value, i.e., the probability of observing the given result, or one more extreme,

by chance if the null hypothesis is true. Small p-values (< 0.1) stand for the invalidity of the null hypothesis (unequal variances).

The two distributions of the second-order scaling exponent are thought to have the same variance, but possibly different means, leading one to the Student's T-test which is computed in a first step by estimating the standard error of the difference of the means:

$$SE = \sqrt{\frac{Var_1 + Var_2}{N_1 + N_2 - 2}\left(\frac{1}{N_1} + \frac{1}{N_2}\right)} \tag{5.1}$$

Var_1 and Var_2 are the variances and N_1 and N_2 are the numbers of points in the first and second samples. In a second step t is computed by

$$t = \frac{\overline{x_1} - \overline{x_2}}{SE} \tag{5.2}$$

In a last step, the p-value or significance of this value t for Student's distribution is evaluated. If the p-value is smaller than the threshold, e.g. 0.01 or 0.001, then the null hypothesis of equal averages is rejected, i.e., the observed difference is very significant.

In the resulting distribution of first-order scaling exponents the high p-value (0.86) of the F-test means that the two distributions have the same variances. The Student T-test gives a very low p-value ($<< 0.001$) which means that the difference of the means of the first-order structure function is highly significant.

Testing the significance of the difference between the scaling exponents of the two regimes has been accomplished successfully up to the fifth order function. For completeness, the mean value of the second order scaling exponent ζ_2 which is the equivalent of the slope of the power spectrum is presented for the two regimes. The mean exponent value in the convective regime is found to be close to $\zeta_2 = 2/3$. In contrast, the mean value in the non-convective air masses is approximately twice that value ($\zeta_2 = 1.19$) (see also Tables 5.2 and 5.3).

The distribution of the observed intermittency is also found to be significantly different between the two regimes: high intermittency prevails in convective air masses ($\zeta_\infty = 0.30$) and low intermittency in non-convective air masses ($\zeta_\infty = 0.11$). These results give evidence that in convective air mass injection of humidity plumes leads to a highly intermittent water vapour field, in contrast to the more monoscaling behaviour found in non-convective air mass where cascad-

ing to smaller scales does homogenise the water vapour field on scales up to 100 km.

Table 5.2: Characteristics and statistical properties (arithmetic mean with standard deviation) of the time series in convective air masses. L is the total length of the time series, N is the number of time series.

Campaign	L [km]	N	ζ_1 (H)	ζ_2	$1/\zeta_\infty$
COPS/ETReC	21,975	58	0.32 ± 0.12	0.61 ± 0.22	0.34 ± 0.19 ($N = 34$)
T-PARC	22,630	34	0.36 ± 0.08	0.67 ± 0.15	0.25 ± 0.12 ($N = 19$)
IPY-THORPEX	10,110	19	0.43 ± 0.08	0.74 ± 0.16	0.23 ± 0.09 ($N = 12$)
Total/Averages	54,715	111	0.35 ± 0.11	0.65 ± 0.20	0.30 ± 0.16 ($N = 65$)

Table 5.3: Characteristics and statistical properties (arithmetic mean with standard deviation) of the time series in non-convective air masses. L is the total length of the time series, N is the number of time series.

Campaign	L [km]	N	ζ_1 (H)	ζ_2	$1/\zeta_\infty$
COPS/ETReC	22,585	39	0.57 ± 0.13	1.04 ± 0.25	0.12 ± 0.09 ($N = 33$)
T-PARC	167,930	231	0.63 ± 0.10	1.20 ± 0.19	0.09 ± 0.07 ($N = 132$)
IPY-THORPEX	123,902	141	0.65 ± 0.09	1.20 ± 0.18	0.13 ± 0.11 ($N = 87$)
Total/Averages	314,417	411	0.63 ± 0.10	1.19 ± 0.19	0.11 ± 0.09 ($N = 252$)

5.4.1 Structure functions in convective air mass

The histogram of the first-order scaling exponents H of the convective air masses (see Figure 5.5 bottom left) has a maximum near the mean value of $H = 0.35 \pm 0.11$. Splitting up the scaling exponent into the three campaigns shows that the values observed for IPY-THORPEX ($H = 0.43 \pm 0.08$), T-PARC ($H = 0.36 \pm 0.08$) and COPS/ETReC ($H = 0.32 \pm 0.12$) are very similar (see Table 5.2). There is only a very small tendency (approximately as large as the standard deviation) for larger scaling exponents during winter in polar regions (IPY-THORPEX) in contrast to T-PARC and COPS/ETReC in summer, but

it is not clear if this has a seasonal, latitudinal or even topographical (difference between land and ocean) origin (see also Figure 5.5 top left). Pressel and Collins (2012) showed in a global analysis of AIRS water vapour data that there is little seasonal variability in the scaling exponents. The results of the present study suggest that latitudinal, seasonal and topographical influences on the scaling exponents are small in comparison to the impact of the different dynamical processes in convective and non-convective air masses. Such influences could exist, but the present data set does not allow their verification. Apparently, the physical mechanism of convection in different environments produces very similar power-laws with a Hurst exponent H of about $\frac{1}{3}$. Interestingly, the low value of the scaling exponent H found for the convective regime R_{conv} is similar to values observed for mesoscale variability in the convective boundary layer (Cho et al., 2000; Kahn et al., 2011; Pressel and Collins, 2012). It is unlikely that the data set analysed in this study contains any significant contribution from the boundary layer, since the lowest 2-3 km of the troposphere are generally excluded due to low data quality and the top of the boundary layer is usually characterised by shallow convective cumulus. It appears, however, that the dynamics of convective clouds in the free troposphere generate water vapour structures similar to the boundary layer, resulting in a similar scaling exponent.

The structure function method has the potential to describe the intermittency of water vapour distributions, as $1/\zeta_\infty$ quantifies the intermittency, whereby the full hierarchy of exponents ζ_q is necessary to qualify the intermittency further (Davis et al., 1994). In principle, intermittency has been used as a description of the tendency of passive tracers to concentrate in localized structures separated by jump discontinuities (Shraiman and Siggia, 2000; Tuck et al., 2003). Similarly, Calif and Schmitt (2012) define intermittency as a property exhibiting large fluctuations at all scales, with correlated structure. Such properties would be expected as a result of injection of moisture by coherent vertical plumes in a region of convection. On the other hand, if intermittency is low, the water vapour field has monoscaling behaviour which is expected for a passive tracer advected by a spatially smooth flow (Chertkov et al., 1995; Pierrehumbert, 1994).

By using the parameterisation of Pierrehumbert (1996) (see Chapter 3), intermittency $1/\zeta_\infty$ could be calculated for 65 time series of the convective regime. Note that this is only about 60 % of the available time series because the remaining 40 % did not achieve the lower bound on R^2 of 0.95 which was defined

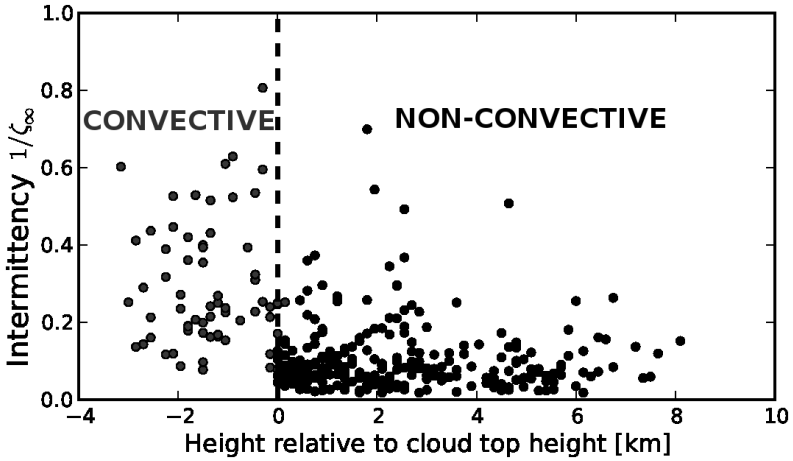

Figure 5.6: The intermittency of convective and non-convective time series of all three campaigns. The x-axis is the height relative to cloud top height.

to identify power-law scaling. The mean value of intermittency in the convective regime, which is nearly identical in all three campaigns, is 0.30 ± 0.16 (see Table 5.2). In Figure 5.6, some outliers in the convective regime with values lower than 0.1, i.e. low intermittency, become apparent, although the majority of the time series are described by high intermittency ($1/\zeta_\infty > 0.2$) or anomalous scaling. Note that despite the appearance of larger scatter in Figure 5.6 for the convective cases, the relative standard deviation is only 10 % larger than for the non-convective cases. In summary, these results show that the water vapour field in convectively influenced air mass in three very different geographical regions behaves similarly with respect to intermittency on horizontal scales up to 100 km.

5.4.2 Structure functions in non-convective air mass

The distribution of first-order scaling exponents for the time series of non-convective air masses, shown in Figure 5.5 (bottom right), is unimodal with a peak occurring very near to $H = 0.6$. Averaged over the whole data set of the non-convective regime we find a mean value of $H = 0.63 \pm 0.10$. As for the convective regime, the observations derived from the three campaigns show similar uncertainty ranges (see Table 5.3). These results confirm that there is remarkably little regional variation in the observed exponents. Furthermore, the Hurst exponents found in this study are consistent with the results of Pressel and Collins

(2012), who report values around 0.55 in the free troposphere (500 hPa level) over horizontal scales from 50 to 500 km. The findings of this thesis are therefore consistent with the hypothesis that the absense of small-scale convective sources in the non-convective regime leads to fewer small-scale water vapour fluctuations, generating smoother time series and therefore higher scaling exponents.

The intermittency is very small in the non-convective regime ($1/\zeta_\infty = 0.11 \pm 0.09$)(see also Figure 5.6). A fraction of 40 % of the calculated fifth-order structure functions does not exhibit power law dependence according to the criterion of $R^2 \geq 0.95$ (see also Chapter 3). Approximately 75 % of the intermittency values are smaller than 0.2. Nevertheless, there are some outliers with values larger than 0.3 (see Figure 5.6), but a physical explanation is still not evident. At least, it can be excluded that these measurements are derived from inside the boundary layer. In principle, the observed intermittency values are mostly lower (less intermittent time series) than the values found by Cho et al. (2000) for the extratropical free troposphere ($1/\zeta_\infty = 0.21$). It should be noted however, that Cho et al. (2000) investigated only 11 free tropospheric extratropical time series, which may have partly been influenced by convection.

5.5 Vertical correlation length of water vapour structures

Taking advantage of the high vertical resolution ($\sim$ 200 m) and accuracy (5 − 7 %) of the water vapour observations from DIAL, the focus of this section lies on the analysis of vertical structure of humidity. In principle, the correlation between water vapour time series at varying heights is quantified, comparable to the method used by Thurai et al. (2004). Therefore, the vertical correlation length of vertically adjacent levels is calculated, i.e., the depth over which the correlation coefficient of water vapour time series in separate levels falls to e^{-1} (Hogan and Illingworth, 2002). Note that the exponential decay of humidity in the vertical would tend to dominate the computed length scale even in the presence of convectively induced vertically coherent structures. This problem is countered by subtracting the mean humidity value from each horizontal time series before correlating it. From simple physical reasoning, it can be hypothesised that water vapour features are correlated over longer vertical distances in the vicinity of convective clouds where vertical up and downdrafts dominate. In

contrast, in regions without convective clouds, the water vapour field might have short vertical correlation lengths due to vertical shear in the large-scale advecting winds.

The analysis of the vertical correlation length between time series at different heights of the three campaigns (COPS/ETReC, T-PARC, T-IPY) is carried out for the convective and non-convective regimes. The average correlation length for the convective regime ($L_{conv} = 0.39 \pm 0.14$ km) is longer than that of the nonconvective regime ($L_{non-conv} = 0.31 \pm 0.12$ km), but with low significance. This may mean that vertical coherent water vapour structures caused by convection have only weak influence on the vertical correlation length in the water vapour field. On the other hand, the given technical restriction that DIAL water vapour observations may not be measured directly below optically thick clouds might have an influence insofar as the observed water vapour field does consequently not fully describe the exisiting vertical coherences, despite the fact that convective turbulence with up- and downward motions of water vapour is also active in the atmosphere around convective clouds (Kottmeier et al., 2008), where the water vapour field is observed by the DIAL. It is also possible that the reduction of vertical coherence by advection in a flow with vertical shear, which is also active in convective regions, may act rapidly enough to reduce the correlation length to values similar to those found in non-convective air masses (see also Cho et al. 2003). The results might be clearer by using data in and beneath the clouds, where correlation should be strongest. For that reason, a future campaign with additional flight-level aircraft data could help to further develop the results of this study.

While the difference in vertical correlation length between convective and non-convective air masses is small when averaged over the entire data set, it can be more apparent when comparing individual case studies, such as the examples shown in Figure 3.8 and Figure 5.7. On July 30 in 2007 (see Figure 5.4 (c)) the DLR Falcon measured water vapour over southwest Germany. The weather during the flight was characterised by shallow cumulus up to a height of 3.5 km. Figure 5.4 (c) shows the two-dimensional water vapour field after interpolating the gaps caused by clouds and after horizontal averaging to about 5 km resolution. Figure 5.7 (left) shows the mean correlation coefficient between water vapour time series at varying heights. On March 17 in 2008 (see Figure 5.4 (a)) the DLR Falcon collected data between South-Norway and North-Germany. The

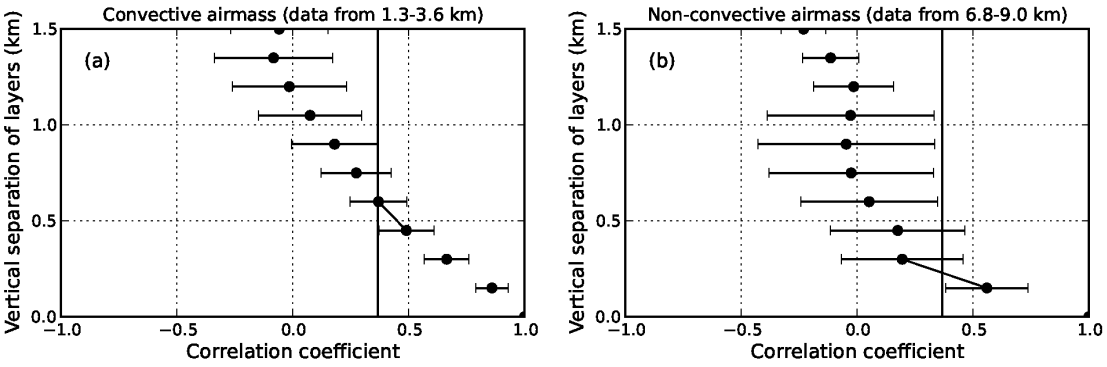

Figure 5.7: Dots depict the mean correlation coefficient of water vapour vs. vertical separation. (left) Results for a 250 km segment on July 30 in 2007 between 1.3 and 3.6 km of height (convective case). (right) Results for a 250 km segment on March 17 in 2008 between 6.8 and 9.0 km of height (non-convective case). The error bars indicate the standard deviation of the raw data. The vertical solid line shows the e^{-1} threshold value. The correlation length is calculated by the linear fit between two points above and below the threshold value.

weather situation was one of shallow cumulus above very dry air is advected. As shown in Figure 5.7 (right) the correlation decreases rapidly with height in this non-convective air mass. To facilitate comparison, we consider data over a vertical range of 2.25 km in both cases. The correlation lengths L_{conv} and $L_{non-conv}$ estimated from these figures are 0.60 and 0.23 km, showing a much longer vertical correlation length for the convective case which confirms the above made hypothesis.

5.6 Summary and discussion

In this chapter, structure functions throughout the troposphere (from 1.5 km up to 10.4 km of height) are computed from spatial increments of the instantaneous water vapour field observed by an airborne DIAL throughout the different campaigns. Water vapour structures of wintertime polar, summertime midlatitude and subtropical regions are analysed. The high horizontal (2 km - 7 km) and vertical resolution (0.15 km) is sufficent to show horizontal structure function scaling from about 5 km to 100 km. By using scaling exponents up to the fifth order, intermittency, which serves as a means of measuring local fluctuations in the water vapour field, is calculated. Finally, the airborne DIAL water vapour observations are highly enough vertically resolved to calculate vertical correlation lengths in the tropospheric water vapour field.

Chapter 5 Air mass dependency of scaling exponents and vertical correlation in the water vapour field

The analysed observations in the paper of Fischer et al. (2012) (please refer to Chapter 4) show that the first-order scaling exponents and the intermittency exhibit significant vertical water vapour variability during summertime over Europe. The present chapter provides an analysis based on a much larger data set with a larger geographical extent, including data from a polar region and from a subtropical region. The conclusion of the earlier study, that there exist two distinct scaling regimes, one in air masses where convection is present, and another one in non-convective air masses, where only large-scale advective processes occur, is confirmed. The analysis of the larger data set which includes substantially more weather situations at different geographical regions, i.e., the different weather regimes have different heights for the top of the convective region, strengthens significantly the conclusions made in Chapter 4.

The presence of convection at given heights is determined by means of examination of the cloud tops seen by the lidar. The analysis performed, basically confirms that the average first-order scaling exponent H in convective air masses is lower than that of the non-convective regime (R_{conv}: $H = 0.35 \pm 0.11$ and $R_{non-conv}$: $H = 0.63 \pm 0.10$). Conversely, the intermittency in convective air masses is higher than for the non-convective regime (R_{conv}: $1/\zeta_\infty = 0.30 \pm 0.16$ and $R_{non-conv}$: $1/\zeta_\infty = 0.11 \pm 0.09$). Within the data set considered here, the scaling behaviours within the two regimes appear further to be independent of latitude and height. In general, scaling exponents $H < 0.5$ have a rougher, more space filling appearance, while scaling exponents $H > 0.5$ are smoother and longer range correlated (see Figure 3.8). The observed Hurst exponent, $H \approx \frac{1}{3}$, seems to be a relatively universal characterisation not only for the atmospheric boundary layer (Cho et al., 2000) but also for layers above where the water vapour field is locally influenced by convective clouds and motions.

The physical picture that emerges from these results is that small-scale motions in the boundary layer or in the cumulus convection above introduce localised, small-scale structures into the atmosphere, leading to a rougher, more intermittent moisture field. In contrast to the convective regime, where local variations establish the spatial variability of water vapour, the non-convective regime is dominated by large-scale flows. These passively advected layers exhibit first-order scaling exponents around a value of $H = 0.6$. The intermittency for the non-convective regime is very low, i.e. there is a tendency of water vapour to

exhibit monoscaling in non-convective air masses as expected for a passive tracer advected by a spatially smooth flow (Chertkov et al., 1995; Pierrehumbert, 1994).

The scaling exponents and intermittency values determined in this analysis are, however, not sufficient in order to clearly establish the underlying physical process. In contrast to turbulent cascade processes of kinetic energy where several theories exist, a quantitative theory that predicts the scaling exponents in a convectively influenced air mass is still missing. It is even possible that different physical mechanisms may result in a similar scaling exponent. On the other hand, the different scaling parameters identified here are strong evidence that the two regimes are dominated by different physical processes on spatial scales from 5 km to 100 km.

In summary, the results show that the physically-based classification of the data set into convective and non-convective air masses leads to two scaling exponent regimes. One could hypothesise that more small-scale variability due to convection as well as primarily localised, vertical convective moisture injection, leads to smaller scaling exponents and higher intermittency values than in non-convective air masses. An alternative approach would be to apply thresholds to the scaling exponent values to separate the data into two classes. The scatter plots (Figure 5.5 and Figure 5.6) show, that the difference of the first-order scaling exponents between the two regimes is clear enough, to realise such an approach. However, the determination of thresholds is subjective, and the intermittency value is quite scattered, since it is the result of two fitting procedures. Therefore, this approach is not further pursued in this thesis.

As a final test of the physical picture gained by the structure function analysis vertical correlation lengths have been computed, in the expectation that local convective circulations will produce structures that are more vertically coherent. A comparison of two case studies showed a longer correlation length for a convective situation than for a non-convective one. Averaged over the entire data set, a longer mean correlation length was again found for the convective regime, however the difference proved not to be statistically significant. In order to further test the hypothesis, a larger data set would therefore be required.

Generally, it would be helpful if more water vapour data in convective regimes would be collected in the future, especially within and beneath clouds. While it is impossible for the DIAL system to measure through optically thick clouds, aircraft in-situ measurement could provide such water vapour series within and

beneath clouds. A flight campaign where aircraft in-situ measurements would be combined with airborne DIAL measurements is therefore advisable. In an ideal case, an aircraft with an onboard DIAL would measure the water vapour field from the tropopause down to and in between convective clouds, while another aircraft would fly simultaneously directly through the convective clouds measuring the water concentration within the clouds and beneath. Since deep convection poses extended risks for aviation, the weather situation should then ideally be characterised by scattered, developing moist convection. Such a campaign configuration could help to gain further valuable insights on how the water vapour distribution in the free troposphere is affected by small-scale convective processes.

Chapter 6

Structure function analysis of the high-resolution regional NWP model COSMO-DE

Up to now, this thesis has primarily been focused on the statistical characterisation of the water vapour variability on the basis of observed airborne lidar data. By means of a classification scheme (see Chapter 4), the data set was split up into convective and non-convective air masses for which two significantly different scaling exponent regimes could. As this work was originally motivated by the development and improvement of the assessment of scale dependence statistics in numerical weather and climate models, the present chapter is now to provide a structure function analysis of tropospheric water vapour simulations from the high-resolution regional NWP model COSMO-DE. Thereby, the present chapter is to explore the introductorily posed scientific question, if the structure functions analysis of numerical simulations of the atmospheric water vapour field exhibits power-law behaviour and how accurately the current high-resolution regional NWP model COSMO-DE reproduces the small-scale water vapour variability observed by airborne lidar if quantified by means of scaling exponents (see Chapter 5). In contrast to the lidar observations, the model simulations do not suffer from undersampling problems (e.g., restricted flight length or data gaps due to clouds). Therefore an additional aim of this chapter is to test the sampling limitations in the observations by means of the model simulations.

As for the general procedure, after providing a brief introduction on the significance of the exerted analysis at hand (Section 6.1), the simulated water vapour field of the NWP model COSMO-DE is divided into convective and non-

convective air masses, based on the air mass classification scheme developed in Chapter 4. Subsequently, structure functions up to the fifth order are calculated for the simulated data and power law scaling is detected on horizontal scales from about 10 km to 100 km based on the methodology described in Section 6.2. Subsequently, the scaling exponents as well as the intermittency derived therefrom are compared to the observed statistics (Section 6.3). Furthermore, in Section 6.4, tests are performed in order to explore the sampling limitations of lidar observations, namely undersampling due to the one-dimensional flight path and data gaps caused by clouds.

6.1 Introduction

Recent observation studies of scale-dependent water vapour variability, including water vapour fluctuations in the middle and lower troposphere, have shown a clear deviation from the $\beta = 5/3$ power law (theoretical value of a passive scalar in three-dimensional turbulence) on spatial scales smaller than 100 km (Cho et al., 1999; Cho et al., 2000; Lovejoy et al., 2010; Fischer et al., 2012; Fischer et al., 2013) as well as on spatial scales larger than 100 km (Kahn and Teixeira, 2009; Kahn et al., 2011; Pressel and Collins, 2012). While a quantitative theory of scaling exponents is still missing, the existing of at least two differing scaling regimes, i.e., convective vs. non-convective air masses, has been confirmed. Fischer et al. (2013) (see also Chapter 5) suggested that water vapour distribution is determined in non-convective regions by a downscale cascade of variance by advective mixing, but increasingly influenced in convective regions by local injection of humidity by moist convection. The power laws are found to vary around $\beta = 2.3$ in non-convective air masses and around $\beta = 5/3$ in convectively influenced air masses.

Even though the interactions between atmospheric motions and water vapour and its influence on the observed water vapour power-laws are not yet sufficiently understood, power-law scaling allows for a reality check on NWP models and GCMs. In this chapter, the ability of the non-hydrostatic mesoscale NWP model, COSMO-DE (Baldauf et al., 2011), to reproduce observed water vapour power law statistics, is examined. While this is not a traditional validation measure, a model's ability to reproduce observed multifractal behavior indicates whether or not it reproduces accurate water vapour statistics and, in this sense, if it is reliable

when compared to the dynamics of the observed atmosphere (Skamarock, 2004). In other words, if a model does not reproduce the real atmosphere's multifractal bahaviour appropriately, this might be an indicator for a shortcoming of the model simulation.

In terms of kinetic energy, the evaluation is useful in order to gain valuable insights into the model physics and to determine how accurately the observed scaling regimes are represented (Skamarock, 2004; Hamilton et al., 2008; Bierdel et al., 2012). In terms of water vapour, the study of Kahn et al. (2011) appears to be exclusive with respect to the use of observational benchmarks of scaling exponents for the evaluation of global NWP and climate models. Kahn et al. (2011) show, that the spectral slopes on horizontal scales from 150 km up to 1000 km of NWP and climate models are generally too steep, i.e., they tend to underestimate small-scale variance of water vapour. While cloud and convective processes are often acting on scales smaller than the resolution of global NWP and climate models, regional high-resolution NWP models with a horizontal resolution of a few kilometres tend to resolve these processes for the most part. Therefore, the present study investigates for the first time the water vapour variability of the high-resolution regional NWP model, COSMO-DE, by means of observed benchmarks of scaling exponents.

The COSMO-DE model analysed in the following has a horizontal grid mesh size of 2.8 km which suffices to explicitly resolve deep moist convection and the associated feedback mechanisms to larger scales. Shallow and midlevel convection are however, still required to be parameterised by means of the Tiedtke scheme (Tiedtke, 1989). The parameterisation of the cloud cover is highly affected by small-scale moisture fluctuations. In particular the calculation of fractional cloud cover presumes information of the inhomogeneous humidity distribution. The COSMO-DE model uses a relative humidity based scheme within the radiation scheme and a pdf-based scheme within the turbulence model in order to parameterise boundary layer clouds. I.e., the simulation analysed in this study is based on computations that partly resolve convective motions which allows for the expectation of accurately modeled small-scale motions. The small-scale humidity distribution, in parts however, is still to be parameterised similar to coarser numerical models which impairs the simulation quality.

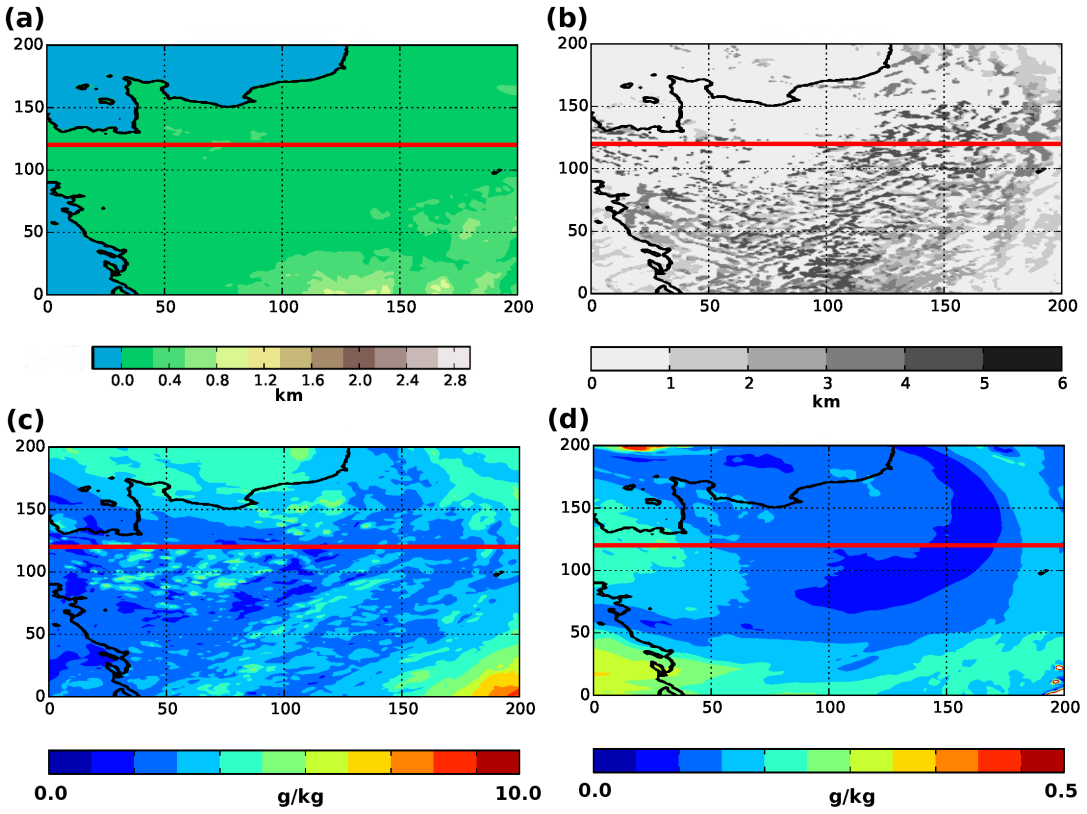

Figure 6.1: (a) COSMO-DE orography; Simulated properties on July 20 at 14 UTC: (b) convective cloud top height, specific humidity field at (c) 2.6 km and (d) 7.6 km height; The solid red line represents the analyzed single slice. The size of the chosen model output is 200 x 200 grid boxes (560 km x 560 km) large.

6.2 Methodology

Based on a simulation from July 20, 2007 at 14 UTC (for further setup information, please refer to Selz and Craig (2013)), the water vapour field of the high-resolution NWP model COSMO-DE is analysed by means of the structure function method similarily applied in Chapters 4 and 5. As the model simulation does not reproduce all clouds precisely at the same position where clouds have been observed by the airborne lidar, a direct comparison of the model 'path' and the real flight path should not be necessary. Further, based on the findings in the observed water vapour field which support the universality of scaling exponents for the particular air masses as well as the independency from latitude, the comparison between observation and simulation is not performed directly by means of

a one by one data reconciliation, i.e., the observed single aircraft overpass is not explicitly separated in the model field. Instead, the analysed simulation area was picked out by laying a priority on the existance of midlevel convective clouds that partly cover the research area (about 30 %, see also Table 6.1) as the observed results are based on partly cloudy or clear sky situations.

A simulation area over flat orography in the northern part of France is chosen, at a date also covered by the COPS/ETReC campaign in July 2007, namely 20 July 2007, was chosen which allows for comparison with the observed air mass dependent scaling statistic.

The horizontal and vertical range of convective clouds, which is important for the application of the classification scheme developed in Chapter 4, is determined by using the COSMO-DE model output field 'convective cloud base height' and 'convective cloud top height'. The simulated data in and beneath clouds is discarded for reasons of comparability with the lidar observations that include no data within and beneath clouds due to the measuring system (see Figure 6.2 (c)). Afterwards the gaps are linearly interpolated just as for small data gaps in the observation field.

After the preparation of the simulated data set, structure functions are calculated up to the fifth order and found to exhibit power-law behaviour. The upper bound of scaling range at 100 km was chosen for a better comparability to the observed scaling range. The lower bound of scaling range at 11 km was given due to the effective resolution criteria of the COSMO-DE model simulation analysed in the study of Bierdel et al. (2012) (see also Chapter 3).

Fur purposes of determining the error due to sampling limitations, two different model statistics are computed, one that includes only the results of a single segment (see Figure 6.1 red line) and another that averages the results of 15 neighbouring segments computed for the same time and showing the same underlying meteorological situation (see Figure 6.5 and Figure 6.6).

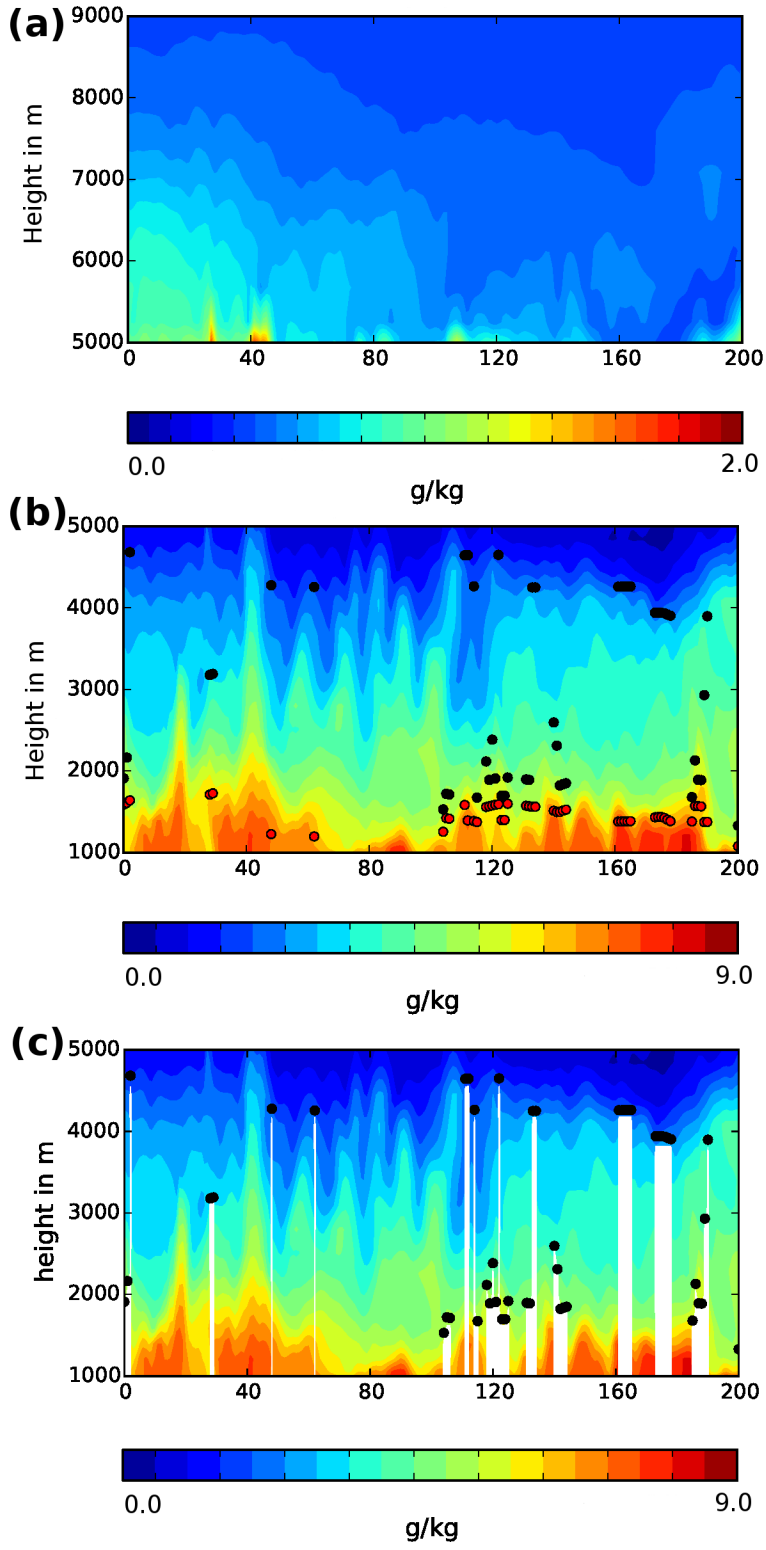

Figure 6.2: Two water vapour cross-sections refering to the solid red line in Figure 6.1. (a) Non-convective regime from 5 km to 9 km height; (b) Convective regime up to a height of about 5 km; (c) Same as (b) but with inserted data gaps beneath convective clouds. Black dots represent the convective cloud top height, red dots the cloud base height.

6.3 Comparison between COSMO-DE simulation and lidar observation

Scaling characteristics observed by airborne lidar

The data set of observations by which the model is evaluated in this chapter has been analysed in a recently published paper of Fischer et al. (2013). They found that the spatial variability of water vapour on scales from about 5 km up to 100 km, expressed by scaling exponents and intermittency, shows two differing scaling regimes dependent on whether convective clouds are occuring or not. Indeed, the convectively influenced water vapour field is characterised by a rough and low-correlative structure interrupted by vertical injections in the form of moist up- and downdrafts resulting in a Hurst exponent of about $H = 0.35$ and high intermittency value $1/\zeta_\infty = 0.3$. In contrast, the water vapour field in regions without convection is smooth and shows a monofractal or monoscaling tendency, i.e., a large Hurst exponent ($H = 0.63$) and small intermittency value $1/\zeta_\infty = 0.11$ characterise the air mass which is dominated by the large-scale circulation. The two scaling regimes are found to be universal on the investigated horizontal spatial scales from 5 km to 100 km.

Based on the restrictions of airborne lidar measurements, i.e., the lack of observation data within and beneath optically thick clouds, the present observational analysis is based on a partly cloudy meteorological situation. Before beginning with the evaluation of the COSMO-DE model, the model's simulated data within and beneath clouds had therefore to be discarded. In a next step, the simulated water vapour field was splitted into the said two regimes by means of the method applied in Chapter 4 and 5, i.e., one regime includes the air mass up to the convective cloud top height and the other regime consists of the air mass above convective clouds.

Scaling characteristics simulated by COSMO-DE

In this study the focus of the examination lies on a 42 km x 560 km area over the northern part of France (see Figure 6.1 (a)), where orographically-induced convection can be excluded due to the absence of mountains. Figure 6.3 shows the satellite picture at 1231 UTC on 20 July 2007 when a developing cyclone moved towards the UK, resulting in a frontal band over southern and eastern

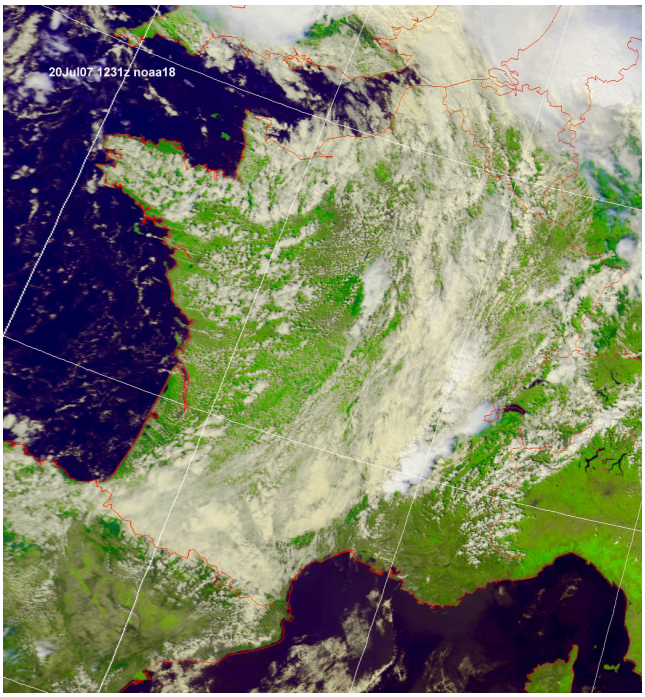

Figure 6.3: Satellite imagery at 1231 UTC on 20 July 2007. Available at: http://www.woksat.info/.

France. In northern and western France cumulus formed in the cold air that followed the cold front. This meteorological situation is generally simulated by the COSMO-DE model. Indeed, at 14 UTC, convection developed up to a height of about 5 km (see Figure 6.1 (b)) leading to two regimes, the convective air masses from about 1.5 km up to 5 km of height and the non-convective regime from about 5.2 km up to about 9 km (see also Figure 6.2).

In Figure 6.1 (c) and (d), the modeled water vapour field at heights of 2.6 km and 7.6 km is shown. While the lower level is dominated by small-scale perturbances, the upper level is characterised by the relatively smooth large-scale circulation. In Figure 6.4, the analysis of two example time series in convective air mass at a height of 2.6 km (left) and non-convective air mass at a height of 7.6 km (right) based on the slice shown in Figure 6.1 by the solid red line, is presented. For illustrating the scaling properties of the COSMO-DE model, Figure 6.4 (middle) also shows the structure functions and the fitted power-laws up to the fifth order and (Figure 6.4 (bottom)) the fitted intermittency value $1/\zeta_\infty$. The plotted time series (Figure 6.4 (top)) clearly show differences in structure (e.g., roughness, jump discontinuities) which are quantified by different power-laws up to the fifth-order structure function (see Figure 6.4 (middle)) and different inter-

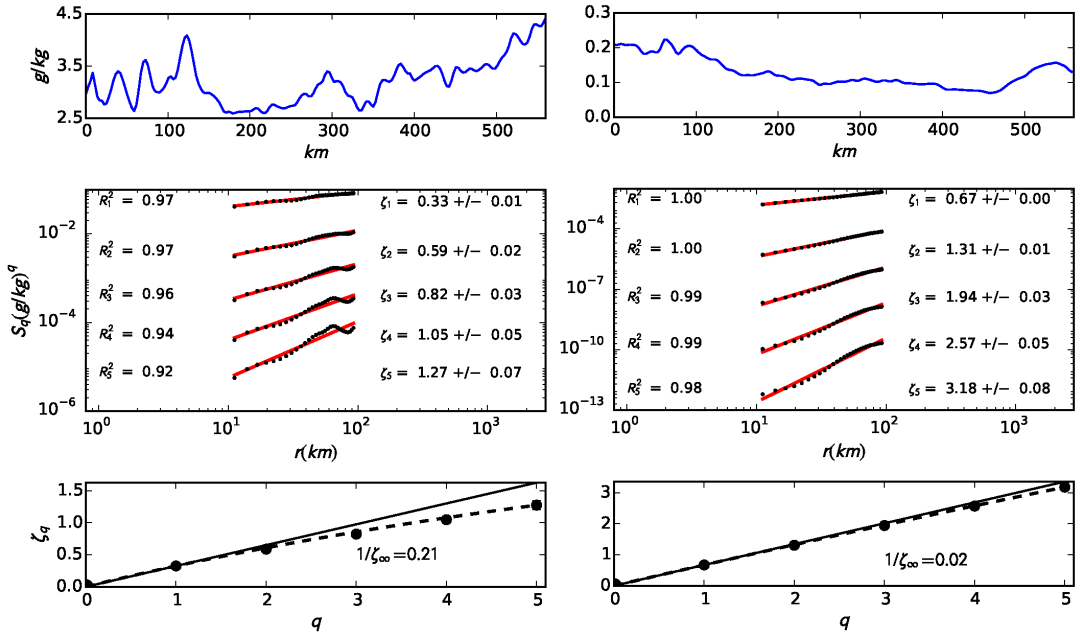

Figure 6.4: Structure function analysis of two simulated time series in the (a) convective and (b) non-convective regime at (a) 2.6 km and (b) 7.6 km height. Representative specific humidity samples (top); Structure functions of the time series up to the fifth order (middle); Average slopes ζ_q versus order q (bottom).

mittency values (see Figure 6.4 (bottom)) quantitatively similar to the observed time series (see Figure 3.8).

The results of the structure function analysis based on 15 neighbouring model segments which are listed in Table 6.1 demonstrate, that the COSMO-DE model simulation reproduces two scaling exponent regimes, dependent on the underlying air mass. Table 6.1 lists the Hurst exponent H, the second-order scaling exponent ζ_2 and the intermittency $1/\zeta_\infty$. $R_{interp.}$ stands for the analysis of the convective regime where data within and beneath clouds is discarded as described in Section 6.2. The averaged Hurst exponent in convective air mass is small, $H = 0.32 \pm 0.08$, in contrast to the value in the non-convective air mass $H = 0.70 \pm 0.09$ suggesting a smooth water vapour field. Intermittency which describes the probability of jump discontinuities, is high in the convectively influenced air mass ($1/\zeta_\infty = 0.46$) and very low, with monofractal tendency, in the upper levels where large-scale advective motions dominate ($1/\zeta_\infty = 0.08$).

Comparison

The analysed statistics of the high-resolution NWP model simulation COSMO-DE are generally consistent with the observed statistics during the COPS campaign which took place over Europe during July 2007 just as the simulated period of the COSMO-DE model, i.e., two air mass dependent scaling regimes qualitatively and quantitatively comparable to the lidar observations, are found in the simulation data. By means of a detailed comparison of the simulation data with the observation study, some small differences can, however, be detected in the non-convective regime where a slightly smoother water vapour field is simulated ($H = 0.70 \pm 0.09$ vs. $H = 0.57 \pm 0.13$). Both the simulation and the observation data set are characterised by a small Hurst exponent, $H = 0.32$, in the convectively influenced air mass. With the exception of intermittency, the deviations of the averaged values are in the range of the small standard deviation of the scaling exponents. The intermittency values in the simulated field are similar to those of the observed data for the convective and the non-convective regime. However, the standard deviation of the intermittency values is high which possibly might be due to the sensitive fitting method adapted from Pierrehumbert (1996). Nevertheless, the clear distinction of averaged intermittency values between the two regimes is significant for the simulated field as well as for the observed data set.

6.4 Impact of sampling-limited airborne DIAL observations on scaling behaviour

In the present section, the impact of the sampling limitation in the lidar observations is to be investigated and quantified. As shown by Fischer et al. (2013), airborne DIAL measurements of water vapour are suitable to describe the water vapour variability on the subgrid scales of current GCMs an as such are highly important in order to improve parameterisations of subgrid-scale cloud processes. As, however, every measuring system suffers from certain restrictions, airborne lidar which covers a two-dimensional water vapour field along the aircraft overpass, is limited especially due to data gaps within and below optically thick clouds. By using the advantage of the high-resolution COSMO-DE model data set which is not affected by neither of these limitations, the influence of the outlined airborne DIAL restrictions on the scaling analysis can be analysed and quantified.

Table 6.1: Scaling properties of one slice and 15 slices simulated by COSMO-DE, the COPS campaign and the 3 campaigns averaged (COPS,T-PARC, T-IPY). ζ_1 or H is the Hurst exponent, ζ_2 the second-order scaling exponent and ζ_∞ the intermittency in convective air mass R_{conv}, convective air mass with data within and beneath clouds discarded $R_{interp.}$ and in non-convective air mass $R_{non-conv}$.

	Segments:	COSMO-DE 1	COSMO-DE 15	COPS 7	3 campaigns 20
ζ_1 (H)	R_{conv}	0.36 ± 0.06	0.30 ± 0.07		
	$R_{interp.}$	0.40 ± 0.06	0.32 ± 0.08	0.32 ± 0.12	0.35 ± 0.11
	$R_{non-conv}$	0.68 ± 0.11	0.70 ± 0.09	0.57 ± 0.13	0.63 ± 0.10
ζ_2	R_{conv}	0.59 ± 0.13	0.47 ± 0.15		
	$R_{interp.}$	0.69 ± 0.14	0.52 ± 0.16	0.61 ± 0.22	0.65 ± 0.20
	$R_{non-conv}$	1.28 ± 0.23	1.29 ± 0.25	1.04 ± 0.25	1.19 ± 0.19
$1/\zeta_\infty$	R_{conv}	0.26 ± 0.14	0.41 ± 0.37		
	$R_{interp.}$	0.17 ± 0.17	0.46 ± 0.40	0.34 ± 0.19	0.30 ± 0.16
	$R_{non-conv}$	0.07 ± 0.05	0.08 ± 0.05	0.12 ± 0.09	0.11 ± 0.09
	Clouds [%]	28 %	30 %		

6.4.1 Observation data set based on single aircraft overpass

Adapted from the structure function analysis of two-dimensional water vapour observations that are divided into convective and non-convective air masses in dependence of the convective cloud top height, one exemplary cross-section of the model simulation on 20 July 2007 at 14 UTC is presently examined. Therefore, one straight path over the northern part of France directed from west to east with a total length of 560 km has been chosen, including convective clouds, i.e., cumulus are active up to a height of 5 km (see red line in Figure 6.1 as well as Figure 6.1 (b) for cloud top height). The height-resolved scaling statistics of the chosen path have then been compared to 15 adjacent straight paths in the same region and at the same time (see Figure 6.5 and Figure 6.6). This data set is suitable for the pursued analysis as it includes both, convective (height < 5 km) and non-convective (height > 5 km) air masses. Further, orographic influences can be excluded in this flat region.

Table 6.1 shows the averaged scaling exponents and intermittency values and explicitly also their standard deviation after calculating the vertically resolved

structure functions up to the fifth order for the single segment and the average values for the 15 segments of the COSMO-DE model simulation data under the same meteorological conditions and at the same time in convective R_{conv} and non-convective $R_{non-conv}$ air masses. For purposes of the present analysis, the standard deviation of the scaling exponents provides a measure that allows for comparing the scattering of scaling exponent values between a single model segment and the 15 averaged model segments. If the standard deviation value of scaling exponents based on a single segment is similar to the standard deviation calculated for the average of 15 segments under the same meteorological situation, it can be concluded that a single segment is sufficient for an adequate representation of a specific air mass. It would further strengthen the reliability of lidar observations that are based on single flight path measurements.

Presently, the standard deviation of the Hurst exponent H of the analysed one model segment shows small deviation from averaged value for the 15 model segments in the averaged value and its standard deviation (R_{conv}: 0.06 vs. 0.07; $R_{non-conv}$: 0.11 vs. 0.09). A similar behaviour is found for the second-order scaling exponent (see Table 6.1). While the standard deviation of the intermittency value shows a larger deviation for the 15 model segments compared to the single model segment within the convective regime, it produces the same value for the non-convective simulation regime (R_{conv}: 0.14 vs. 0.37; $R_{non-conv}$: 0.05 vs. 0.05). I.e., it can generally be summarised that the standard deviation values are quite similar for the single model segment and the 15 averaged model segments for the predefined partly cloudy meteorological situations. Therefore, one segment should allow for a characterisation of convective and non-convective regimes via the structure function method, but the sensible intermittency value gained from higher-order scaling exponents seems to be less robust when several segments are averaged, especially in convectively influenced air mass. Nevertheless, the height-resolved observations of an airborne DIAL along one flight path should be adequate in order to characterise the spatial variability of water vapour throughout the troposphere. At least on first-order moment statistics, undersampling problems seem not to be significant.

6.4.2 Observation data set with gaps within and beneath optically thick clouds

In a second step the influence of clouds on the water vapour field, specifically the data gaps of lidar observations due to optically thick clouds, is analysed by quantifying its relevance on the structure function method. In contrast to the airborne DIAL data for which small gaps due to clouds have to be interpolated, the model simulations include precise water vapour simulation data in and beneath clouds. Based on this fact, we computed structure functions of the simulated data in the convective regime twice. In a first step, data in and beneath clouds has been removed and afterwards interpolated ($R_{interp.}$) in order to make the modeled data set comparable to the observation (see Figure 6.2 (c)). In a second step, structure functions were computed based on the model output of water vapour including values beneath clouds (see Figure 6.2 (b)).

Table 6.1 demonstrates the differences between the scaling exponents from modeled data with true water vapour field R_{conv} and interpolated field $R_{interp.}$. The Hurst exponent and the second-order scaling exponent of the 15 segments from COSMO-DE are both steeper in the interpolated data set ($H = 0.32$ vs. $H = 0.30$; $\zeta_2 = 0.52$ vs. $\zeta_2 = 0.47$), i.e., the interpolation of water vapour within and benath convective clouds leads to a smoother water vapour field with less small-scale variability. As a consequence, it can be assumed that the lidar observations without measurements in and beneath clouds show a lack of small-scale water vapour variance in the data. However, the influence resulting therefrom on the scaling exponents is rather small in comparison to the different values found for the two regimes. Concerning the intermittency, the difference between values in R_{conv} and $R_{interp.}$ is not significant because of the large standard deviation.

6.5 Summary and discussion

Horizontal structure function analysis is performed using water vapour data from the COSMO-DE model simulation with a grid mesh size of 2.8 km. Power-laws are identified up to the fifth order over spatial scales from about 10 km to 100 km. Based on a simulation during the COPS campaign on July 20 in 2007, where cumulus clouds were active up to a height of about 5 km, the data set has been splitted into two air masses, i.e., convective and non-convective. The two regimes can be characterised by significantly different scaling exponents and

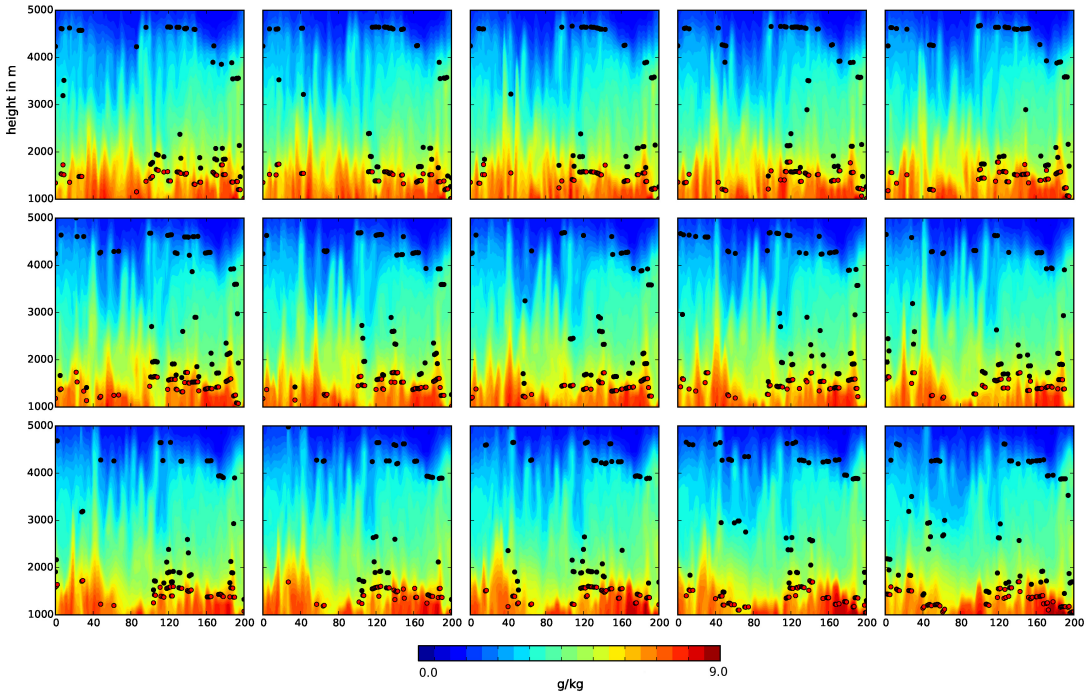

Figure 6.5: 15 water vapour cross-sections from a convective regime from about 1 km to 5 km height covering a horizontal area of 42 km x 560 km. Black dots represent the convective cloud top height, red dots the cloud base height.

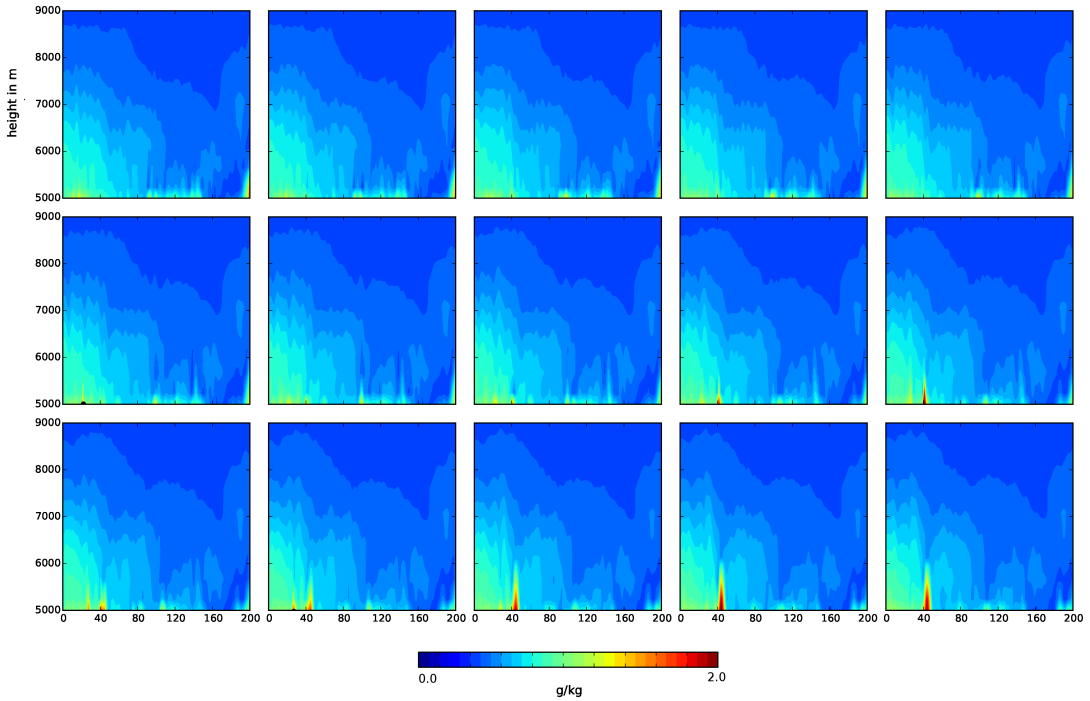

Figure 6.6: 15 water vapour cross-sections from a non-convective regime from 5 km to 9 km height covering a horizontal area of 42 km x 560 km.

intermittency values, with rough ($H = 0.32$) and highly intermittent structures ($1/\zeta_\infty = 0.46$) in the convective air mass, as well as smooth ($H = 0.70$) and monofractal ($1/\zeta_\infty = 0.08$) behaviour in the non-convective air mass.

Further, a comparison of the scaling statistics based on the COSMO-DE simulation with the observational results from the COPS campaign is performed. It reveals that COSMO-DE reproduces the observed scaling characteristics quite well, indicating that the small-scale water vapour variability is modeled quite accurately by the high-resolution, regional NWP model COSMO-DE. This result is in contrast to the study of Kahn et al. (2011), where global NWP models were tested by observed scaling benchmarks from AIRS and found to be underestimating the variability on small scales. However, the spatial scales considered in the study of Kahn et al. (2011) are much larger, starting from about 150 km up to 1000 km.

The presently confirmed consistency of the lidar observation and the model simulation data allows for testing the influence of sampling limitations in the lidar observations on the basis of the COSMO-DE model data set. As comparing a single model cross-section to 15 adjacent model cross-sections shows only small differences in the scaling statistics, i.e., the difference in the standard deviation values of the scaling exponents was found to be quite small, it can be concluded that the undersampling problem of airborne lidar observations is not significant, at least for the lower-order statistics. Furthermore, it has been demonstrated that the influence of missing data within and beneath clouds is small, i.e., the scaling exponents differ only in the range of the standard deviation.

As such this chapter successfully demonstrates that statistical scale invariance, i.e., power-law scaling, of the water vapour field can be used to assess weather simulations with regard to their small-scale variance. Further, two main shortcomings of the lidar observations were investigated and could be quantified as beeing insignificant on the basis of the model simulations. The consistency between the scaling exponents determined for observed data and model simulations may provide a basis for a further model analysis (e.g., in the boundary layer) that might provide for further insights into the physical processes responsible for the transport and mixing of water vapour.

Chapter 7

Conclusion

This thesis was primarily set out to explore the variability of tropospheric water vapour by focusing on small-scale currents in convectively influenced air masses. In an effort to achieve this objective, the quality of an empirical water vapour data set collected by an airborne lidar has been tested in terms of accuracy and signal noise, and has been identified to be suitable for developing a height-resolved statistical characterisation of the tropospheric water vapour field. Without any doubt, an accurate description of the small-scale inhomogeneities of the water vapour field is essential for improving the parameterisation of subgrid-scale processes in NWP models and GCMs. Cloud parameterisations, in particular, depend directly on the inhomogeneous distribution of humidity on subgrid-scale. A lack of knowledge concerning these inhomogeneities increases the model bias of current NWP models and GCMs not only with regard to cloud forming processes but also concerning precipitation and radiation effects. Aside from empirically analysing the tropospheric water vapour variability, this study has further been intended to analyse by means of the observed data and the insights obtained therefrom whether the current high-resolution, regional NWP model COSMO-DE of the DWD displays the observed small-scale variability correctly.

As outlined in the introductory parts of this thesis, the general empirical literature on these issues is inconclusive with regard to several intrinsic questions. While the main empirical findings of this thesis were summarised within the respective Chapters 4 and 5, and the evaluation of the NWP model simulation was described in Chapter 6, this section will synthesise the whole findings in order to provide an answer to the three major research questions underlying this thesis that have been established in Chapter 1, namely:

1 Does the data set of water vapour observations, collected by an unique airborne DIAL, allow for an improvement of the characterisation of small-scale water vapour variability required for improving parameterisations in numerical weather and climate models?

2 Does the analysis of height-resolved airborne DIAL data provide any new theoretical insights into the physical mechanisms, responsible for the observed variability of water vapour throughout the troposphere?

3 Does the high-resolution regional NWP model COSMO-DE capture the observed small-scale variability?

Restatement of primary research results

As regards research object **1**, a height-resolved statistical characterisation of the instantaneous, tropospheric water vapour variability on small spatial scales (5 km - 100 km) has been developed in this study by applying structure functions to a unique airborne water vapour lidar data set for the first time. Thereby, the analysis performed, revealed that structure functions of different orders, i.e., the power-law scaling exponents derived therefrom, allow to distinguish between different physical processes responsible for water vapour variability. By means of an applied objective classification scheme, the water vapour field was split into two regimes, i.e., convective and non-convective air masses, dependent on whether cumulus clouds were observed or not. For these two regimes, different scaling exponent behaviour could be distinguished:

1. **Convective regime**
   Convection is found to be a local small-scale source of water vapour variability that leads to a rather rough ($H = 0.35$), more intermittent ($1/\zeta_\infty = 0.30$) moisture field.

2. **Non-convective regime**
   Water vapour layers that are passively advected by the large-scale flow tend to be smooth ($H = 0.63$) and exhibit low intermittency ($1/\zeta_\infty = 0.11$).

In respect of research object **2**, by means of the analysis performed, the different scaling parameters determined provide strong evidence that the two regimes are

dominated by different physical processes on spatial scales from 5 km to 100 km. Yet, a quantitative theory that reliably predicts the scaling exponents in convectively influenced air masses is still missing.

The findings relating to research object **3** have consequently been based on the observed statistics, i.e., power-law scaling was proposed as a way of comparing the small-scale water vapour variability in the high resolution NWP model COSMO-DE with the observed measurement data. The results obtained therefrom, let conclude that the COSMO-DE simulation reproduces the two observed scaling regimes for the most part sufficiently, and can as such reversely serve as an adequate testbed for sampling limitations of the lidar observations.

Critical analysis of the present work

The improvement of subgrid-scale cloud parameterisations highly depends on an accurate characterisation of the water vapour field on small spatial scales. The observational data that such a newly to be established characterisation should be based on, would ideally provide both, global coverage and cloud scale resolution. The presently analysed airborne lidar observations, however, are based on water vapour profiles along a flight path which substantially limits the variety of observed meteorological situations. As by means of reversely using the model simulations for testing sampling limitations of the observed lidar data, the reduced coverage of the airborne lidar profiles underlying this study was estimated to be relatively small, the error resulting thereof with respect to the structure function analysis due to the limited flight length could not be carved out. The upper bound of the horizontal scaling range therefor depends on the length limitations of the aircraft observations. The lower bound is influenced by instrumental noise, that predominates atmospheric signals on scales smaller than about 1-5 km.

The quality of the underlying data set is further limited by gaps due to optically thick clouds, i.e., water vapour observations within and beneath clouds have been missing. Therefore, flights over regions with large cloud fraction have been avoided, even though it might produce interesting results to investigate e.g., the scaling behaviour of a cross section through the centre of a cyclone which is not yet known. Nevertheless, the influence of a biased water vapour field due to small clouds on the structure function analysis, has been tested and evaluated in this study by using the model simulations and was found to be rather low.

Chapter 7 Conclusion

This study underscores the existence of two differing scale dependence regimes. The classification of these two regimes is based on determining the cloud top height by means of the lidar backscatter field. Considering the above outlined sampling limitations, radar observations and further convective measures (e.g. CAPE and CIN) might have to be considered to further confirm and strengthen the presently defined differentiation scheme for air masses.

Advances compared to previous work

In view of the existing research work on water vapour variability described by means of power-laws (Nastrom et al., 1986; Mannes and Stanford, 1990; Tjemkes and Visser, 1994; Cho et al., 1999 and 2000; Kahn and Teixeira, 2009; Kahn et al., 2011; Lovejoy, 2010; Pressel and Collins, 2012), it becomes clear that measuring free tropospheric water vapour with a high vertical and horizontal resolution is still a challenging issue. While in all these satellite or insitu-aircraft studies, the structure function method or power spectrum method was succesfully applied to the respective underlying data set, the conclusions gained are rather limited due to bad spatial resolution of the instantaneous water vapour field. In contrary, the airborne lidar data set underlying this study provides a unique scale dependence statistic with outstanding high vertical resolution (< 200 m), that makes investigations on cloud scale possible. The high horizontal resolution (< 3 km) further leads to a water vapour data set that includes even small-scale convective fluctuations. Therefore, this study is able to reveal the influence of convective motions on the water vapour field on horizontal spatial scales from 5 km to 100 km by means of the structure functions.

I.e., the studies mentioned above show highly variable scaling exponents over a wide range of spatial scales but the conclusions gained therefrom are contradictory, including universality assumptions of the scaling exponents based on the theory of a passive tracer (Nastrom et al., 1986; Cho et al., 1999), increasing exponents with height (Tjemkes and Visser, 1994; Kahn et al., 2011), boundary layer vs. free troposphere (Cho et al., 2000; Pressel and Collins, 2012) or even no assumptions on physical mechanisms (Lovejoy, 2010). Unlike this, the data set analysed in this thesis (Fischer et al., 2012 and 2013) allows for a distinction between the scaling behaviour applicable for air masses dominated by small-scale convective currents and for air masses dominated by large-scale advection processes.

As outlined before, the present study additionally demonstrates by using model simulations from the high-resolution NWP model COSMO-DE, that the limitations of the underlying lidar observations are rather small which strengthens the reliability of the observed scale dependence results.

Recommendations for future research

At present, the outlined limitations of this work might possibly reduce the profit gained from the successful application of the scale dependence analysis to the unique airborne lidar data set underlying this thesis. Therefore, in view of future research projects, the said limitations, i.e., undersampled lidar observations due to the low number of flights and due to data gaps caused by clouds, should be further minimised by combining airborne lidar and aircraft insitu measuring systems in future campaigns.

At present and presumably in the near future also, the available observing systems are not expected to provide both, global coverage as well as horizontal and vertical cloud-scale measurements throughout the troposphere of the water vapour field which allow for an accurate description of subgrid-scale variability required for improving cloud parameterisations. According to the findings of this thesis, the simulation of the high-resolution NWP model COSMO-DE showed qualitative similarities to the lidar observations. Kahn et al. (2011) however found that current global models underestimate the variability on small scales. Future generations of GCMs with a horizontal resolution smaller than 1 km are already being developed (e.g., Stevens et al., 2011) and should then be evaluated by using scale-dependence methods. They can possibly provide more accurate estimates of small-scale water vapour variations.

If by using model data, tests would be performed that allow for a further investigation of the physical processes responsible for different types of cascades, subsequently leading to a quantitative scaling exponent theory, a major milestone would have been reached for a substantial improvement of understanding the complex interactions between atmospheric motions and water vapour on various spatial scales.

Application recommendations

The research findings of this thesis provide for three major links to the practical application field:

1. Observation
2. Theory
3. Model

As regards point 1., realisations of subgrid moisture pdf's can be constructed based on the observed scaling exponent statistics. Further, different environmental humidity values can be randomly assigned to the plumes in a stochastic convection scheme. Analogous methods are already in use for down-scaling precipitation forecasts based on spectral information (Rebora et al., 2006), and could easily be extended to multifractal descriptions using techniques such as bounded cascade models (Cahalan, 1994). Based on the existence of clear scaling behaviour, Schemann et al. (2013) emphasise the necessity to include a scale dependency in future cloud process parameterisations. The methodology developed for computing structure functions can also be applied to other atmospheric trace gases observed by lidar systems and could therefore provide further fundamental insights into the transport and mixing of quantities. The success of the present scale dependence study underscores the clear utility of future airborne lidar campaigns, providing vertically resolved measurements of atmospheric consituents.

The application of the present thesis results for building up a theoretical explanation are rather marginal. At present, there is no theoretical explanation for the two differing scaling exponent regimes of water vapour structure functions that have been observed at scales from about 5 km to 100 km. The convective regime shows a scaling exponent of $H \approx 1/3$ and high intermittency. There is a striking agreement to the observed scale dependence in the boundary layer even if the mechanisms responsible for the observed variability are quite different. This thesis provides strong evidence, that small-scale convective motions and further vertical moisture injections lead to a rough and highly intermittent horizontal water vapour field in the free troposphere. The results for the non-convective regime with a scaling exponent of $H \approx 0.6$ and a tendency of monoscaling are quite consistent with results of Pressel and Collins, (2012). They argued that the water vapour distribution in the midlevel troposphere is controlled by the

influence of twodimensionality of the velocity field. The explanations of the predominant mechanism in the non-convective regime made in the present thesis refer to water vapour layers that are passively advected by the large-scale flow and therefore expected to exhibit no intermittency. However, the observed scaling exponents are significantly steeper than the theoretical value predicted by the Batchelor tracer spectrum for two-dimensional turbulence ($\beta = 1$), which may indicate that vertical shear plays a role in removing small-scale variability. Further theoretical work, including numerical studies may provide insight into mixing and transport processes on small spatial scales and hopefully lead to a quantitative scaling exponent theory.

Refering to point 3., the scaling of atmospheric spectra has been used to assess climate simulations concerning kinetic energy, temperature and atmospheric tracers (Skamarock, 2004; Hamilton et al., 2008; Kahn et al., 2011). However, so far only one study exists that evaluated GCMs with regard to their small-scale water vapour variance (Kahn et al., 2011). By using observed scaling benchmarks, Kahn et al. (2011) showed that GCMs underestimate the small-scale water vapour variability. In contrast, this thesis provides for an evaluation of the high resolution NWP model COSMO-DE, which is found to capture the small-scale variability quite well in partly cloudy and clear sky troposphere.

Abbreviations

AIRS ..... Atmospheric Infrared Sounder

AMSU ..... Advanced Microwave Sounding Unit

COPS ..... Convective and Orographically-induced Precipitation Study

COSMO ..... Consortium for Small-scale Modeling

COSMO-DE .. COSMO Deutschland

COSMO-EU .. COSMO Europa

DFG ..... Deutsche Forschungsgemeinschaft

DIAL ..... Differential Absorption Lidar

DLR ..... Deutsches Zentrum für Luft- und Raumfahrt

DWD ..... Deutscher Wetterdienst

ECMWF ..... European Centre for Medium-Range Weather Forecasts

ETReC ..... European THORPEX Regional Campaign

GCM ..... Global Climate Model

GPS ..... Global Positioning System

HALO ..... High Altitude and Long Range Research Aircraft

HIRS ..... High Infrared Resolution Sounder

IFS ..... Integrated Forecast System

IPY ..... International Polar Year

NWP ..... Numerical Weather Prediction

OLR ..... Outgoing longwave radiation

OPO ..... Optical Parametric Oscillator

pdf ..... Probability density function

SNR ..... Signal-to-noise-ratio

SPP ..... Schwerpunktprogramm

SSMI ..... Special Sensor Microwave Imager

T-PARC ..... THORPEX-Pacific Asian Regional Campaign

THIR ..... Temperature-Humidity Infrared Radiometer

THORPEX ... The Observing System Research and Predictability Campaign

TOVS ..... TIROS-N Operational Vertical Sounder

WALES ..... Water Vapor Lidar Experiment in Space

Bibliography

Andersson E., et al. (2005), Assimilation and modeling of the atmospheric hydrological cycle in the ECMWF forecasting system, *Bull. Am. Meteorol. Soc., 86*, 387–402.

Andersson E., E. Holm, P. Bauer, A. Beljaars, G. A. Kelly, A. P. McNally, A. J. Simmons, J-N- Thepaut, and A. M. Tompkins (2007), Analysis and forecast of the main humidity observing systems, *Q. J. R. Meteorol. Soc., 133*, 1473–1485.

Arakawa A., and W. H. Schubert (1974), Interaction of a cumulus coud ensemble with the large-scale environment. Part I, *J. Atmos. Sci., 31*, 674–701.

Aumann H. H., et al. (2003), AIRS/AMSU/HSB on the Aqua mission: Design, science objectives, data products, and processing systems, *IEEE Trans. Geosci. Remote Sens., 41*, 253–264.

Baldauf, M., J. Förster, S. Klink, T. Reinhardt, C. Schraff, A. Seifert, and K. Stephan (2011), Kurze Beschreibung des Lokal-Modells Kürzestfrist COSMO-DE (LMK) und seiner Datenbanken auf dem Datenserver des DWD, *Deutscher Wetterdienst (DWD), Offenbach, Germany,* 72 pp.

Baumgardner, D., L. Avallone, A. Bansemer, S. Borrmann, P. Brown, U. Bundke, P. Y. Chuang, D. Cziczo, P. Field, M. Gallagher, J. Gayet, A. Heymsfield, A. Korolev, M. Krämer, G. McFarquhar, S. Mertes, O. Möhler, S. Lance, P. Lawson, M. D. Petters, K. Pratt, G. Roberts, D. Rogers, O. Stetzer, J. Stith, W. Strapp, C. Twohy, and M. Wendisch (2012), In situ, airborne instrumentation: addressing and solving measurement problems in ice clouds, *Bull. Am. Meteorol. Soc.,*, *93*, ES29-ES34, doi:10.1175/BAMS-D-11-00123.1.

Bengtsson, L., K. I. Hodges, and S. Hagemann (2004), Sensitivity of large-scale atmospheric analyses to humidity observations and its impact on the global water cycle and tropical and extratropical weather systems in ERA40, *Tellus, Ser. A, 56*, 202–217.

Bibliography

Bhawar, R., P. Di Girolamo, D. Summa, C. Flamant, D. Althausen, A. Behrendt, C. Kiemle, P. Bosser, C. Cacciani, C. Champollion, T. Di Iorio, R. Engelmann, C. Herold, S. Pal, M. Wirth and V. Wulfmeyer (2010), The water vapour intercomparison effort in the framework of the Convective and Orographically-induced Precipitation Study: Airborne-to-ground-based and airborne-to-airborne lidar systems, *Q. J. R. Meteorol. Soc., 137*, 325–348, DOI:10.1002/qj.697.

Bierdel, L., P. Friedrichs, and S. Bentzien (2012), Spatial kinetic energy spectra in the convection-permitting limited-area NWP model COSMO-DE, *Meteorol. Zeitschrift., 21*, 245–258, doi:10.1127/0941-2948/2012/0319.

Bretherton, C. S., M. E. Peters, and L. E. Back (2004), Relationships between water vapor path and precipitation over the tropical oceans, *J. Climate,*, *17*, 1517–1528.

Browell, E. V. (1983), Remote sensing of tropospheric gases and aerosols with airborne DIAL system, in D. K. Killinger and A. Moordian (eds.), *Optical Laser and Remote Sensing,* Springer-Verlag, New-York, 138–147.

Brown, R. G., and C. Zhang (1997), Variability of midtropospheric moisture and its effect on cloud-top height distribution during TOGA COARE, *J. Atmos. Sci., 54*, 2760–2774.

Bryan, G. H, J. C. Wyngaard, and J. M. Fritsch (2003), Resolution requirements for the simulation of deep moist convection, *Mon. Wea. Rev., 131*, 2394–2416.

Buban M. S., C. L. Ziegler, E. N. Rasmusen, and Y. P. Richardson (2007), The dryline on 22 May 2002 during IHOP: Ground-radar and in situ data analyses of the dryline and boundary layer evolution, *Mon. Weather Rev., 135*, 2473–2505.

Buizza, R., M. Miller, and T. N. Palmer (1999), Stochastic representation of model uncertainties in the ECMWF ensemble prediction scheme, *Q. J. R. Meteorol. Soc., 125*, 2887–2908.

Cahalan, R. F., (1994), Bounded cascade clouds: albedo and effective thickness, *Nonlinear Proc. Geophys., 1*, 156–176.

Bibliography

Calif, R., and F. G. Schmitt (2012), Modeling of atmospheric wind speed sequence using a lognormal continuous stochastic equation, *J. Wind Eng. Ind. Aerodyn., 109*, 1–8.

Chahine, M. T. (1992), The hydrological cycle and its influence on climate, *Nature, 359*, 373–380.

Chertkov, M., G. Falkovich, I. Kolokolov, and I. Lebedev (1995), Statistics of a passive scalar advected by a large-scale two-dimensional velocity field: Analytic solution, *Phys. Rev., E51*, 5609–5627.

Cho, J. Y. N., Y. Zhu, R. E. Newell, B. E. Anderson, J.D. Barrick, G. L. Gregory, G. W. Sachse, M. A. Carroll, and G. M. Albercook (1999), Horizontal wavenumber spectra of winds, temperature, and trace gases during the Pacific Exploratory Missions: 1. Climatology, *J. Geophys. Res., 104*, 5697–5716.

Cho, J. Y. N., R. E. Newell, and G.W. Sachse (2000), Anomalous scaling of mesoscale tropospheric humidity fluctuations, *Geophys. Res. Lett., 27*, 377–380.

Cho, J. Y. N., R. E. Newell, B. E. Anderson, J. D. W. Barrick, and K. L. Thornhill (2003), Characterizations of tropospheric turbulence and stability layers from aircraft observations, *J. Geophys. Res., 108(D20)*, 8784, doi:10.1029/2002JD002820.

Coeurjolly, J. F. (2001), Simulation and identification of the fractional Brownian motion: a bibliographic and comparative study, *J. Stat. Softw., 5*, 1–53.

Corrsin, S. (1951), On the spectrum of isotropic temperature fluctuations in an isotropic turbulence, *J. Appl. Phys., 22*, 469–473.

Craig, G. C., and B. G. Cohen (2006), Fluctuations in an equilibrium convective ensemble. Part I: Theoretical formulation, *J. Atmos. Sci., 63*, 1996–2004.

Crook N. (1996), Sensitivity of moist convection forced by boundary layer processes to low-level thermodynamic fields, *Mon. Weather Rev., 124*, 1767–1785.

Cusack, S., J. M. Edwards, and R. Kershaw (1999), Estimating the subgrid variance, and its parameterization for use in a GCM cloud scheme, *Q. J. R. Meteorol. Soc., 125*, 3057–3076.

Bibliography

Davis, A., A. Marshak, W. Wiscombe, and R. Cahalan (1994), Multifractal characterizations of nonstationarity and intermittency in geophysical fields: Observed, retrieved, or simulated, *J. Geophys. Res., 99*, 8055–8072.

Deschamps, P. Y., R. Frouin, and L. Wald (1981), Satellite determination of the mesoscale variability of the sea surface temperature, *J. Phys. Oceanogr., 11*, 864–870.

Do, T., A. M. Ghez, M. R. Morris, S. Yelda, L. Meyer, R. R. Lu, S. D. Hornstein, and K. Matthews (2009), A near-infrared variability study of the galactic black hole: a red noise source with no detected periodicity, *Astrophys. J., 691*, doi:10.1088/0004-637X/691/2/1021.

Doms, G., J. Förster, E. Heise, H.-J. Herzog, D. Mironov, M. Raschendorfer, T. Reinhardt, B. Ritter, R. Schrodin, J.-P. Schulz, and G. Vogel (2011), A description of the nonhydrostatic regional COSMO model. Part II: Physical parameterization, *available online at http://www.cosmo-model.org, Deutscher Wetterdienst (DWD), Offenbach, Germany.*

Dotzek, N., and K. Gierens (2008), Instantaneous fluctuations of temperature and moisture in the upper troposphere and tropopause region. Part 2: Structure functions and intermittency, *Meteor. Z., 17*, 323–337.

Ebert, E., U. Damrath, W. Wergen, and M. Baldwin (2003), The WGNE assessment of short-term quantitative precipitation forecasts, *Bull. Amer. Meteorol. Soc., 84*, 481–492.

Ehret, G., C. Kiemle, W. Renger, and G. Simmet (1993), Airborne remote sensing of tropospheric water vapor with a near-infrared differential absorption lidar system, *Appl. Opt., 32*, 4534–4551.

Elliott, W. P. (1995), On detecting long-term changes in atmospheric moisture, *Climatic Change, 31*, 349–367.

Elliott, W. P., and D. J. Gaffen (1991), On the utility of radiosonde humidity archives for climate studies, *Bull. Am. Meteorol. Soc., 72*, 1507–1520.

Elliott, W. P., and D. J. Gaffen (1995), Chapman conference probes water vapor in the climate system, *Eos. Trans. Amer. Geophys. Union, 76*, 67.

Bibliography

Emanuel, K. A., and R. T. Pierrehumbert (1996), Microphysical and dynamical control of tropospheric water vapor, in *Cloud Chemistry and Climate, NATO ASI Ser., Ser. I,* vol. 35, edited by P. J. Crutzen and V. Ramanathan. Springer, Berlin, 272pp.

Ferrare, R., et al. (2006), Evaluation of daytime measurements of aerosols and water vapor made by an operational Raman lidar over the Southern Great Plains, *G. Geophys. Res., 111*, D05S08 doi:10.1029/2005JD005836.

Fischer, L., C. Kiemle, and G. C. Craig (2012), Height-resolved variability of midlatitude tropospheric water vapor measured by airborne lidar, *G. Res. Lett., 39*, doi:10.1029/2011GL050621.

Fischer, L., G. C. Craig, and C. Kiemle (2013), Horizontal structure function and vertical correlation analysis of mesoscale water vapor variability observed by airborne lidar, *J. Geophys. Res. Atmos., 118*, doi:10.1002/jgrd.50588.

Garand, L., E. Gerard, P. di Girolamo, D. Tan, V. Wulfmeyer, K. Gierens, B. Mayer, C. Kiemle and G. Ehret (2002), Expected benefit of observations provided by a water vapour DIAL on atmospheric data analysis, Final report, ESA Contract 15407/01/NL/SF.

Hagedorn, R. (2010), Operational and research activities at ECMWF. ECMWF Training Course: *Data assimilation and use of satellite data,* www.ecmwf.int/newsevents/training/meteorological_presentations/MET_DA.html

Hamilton, K., Y. O. Takahashi, and W. Ohfuchi (2008), Mesoscale spectrum of atmospheric motions investigated in a very fine resolution global general circulation model, *J. Geophys. Res., 113*, D18110, doi:10.1029/2008JD009785.

Harnisch, F., M. Weissmann, C. Cardinali, and M. Wirth (2011), Experimental assimiliation of DIAL water vapour observations in the ECMWF global model, *Q. J. R. Meteorol. Soc., 137*, 1532–1546, DOI:10.1002/gj.851.

Harris, D., E. Foufoula-Georgiou, K. K. Droegemeier, and J. Levit (2001), Multiscale statistical properties of a high-resolution precipitation forecast, *J. Hydromet., 2*, 406–418.

Healy, S., and J. Thepaut (2006), Assimilation experiments with CHAMP GPS radio occultation measurements, *Quart. J. Roy. Meteor. Soc., 132*, 605–623.

Bibliography

Held, I. M., and B. J. Soden (2000), Water vapor feedback and global warming, *Ann. Rev. Energy Env., 25*, 441–475.

Hocke, K., and N. Kämpfer (2009), Gap filling and noise reduction of unevenly sampled data by means of the Lomb-Scargle periodogram, *Atmos. Chem. Phys., 9*, 4197–4206, doi:10.5194/acp-9-4197-2009.

Hogan, R. J., and A. J. Illingworth (2002), Parameterizing ice cloud inhomogenity and the overlap of inhomogenities using cloud radar data, *J. Atmos. Sci., 60*, 756–767.

Hsu, H.-m., C.-Y. Lin, A. Guenther, J.J. Tribbia, and S. C. Liu (2011), Air-chemistry 'turbulence': power-law scaling and statistical regularity, *Atmos. Chem. Phys. Discuss., 11*, 9 635–9 672, doi:10.5194/acpd-11-9635-2011.

Hurst, H. E. (1956), Methods of using long-term storage in reservoirs, *ICE Proc., 5*, 519–543.

IPCC (2007), Climate Change 2007: The Scientific Basis, *Cambridge University Press,* 940 pp.

John V. O., S. A. Buehler, and N. Courcoux (2006), A cautionary note on the use of Gaussian statistics in satellite-based UTH climatologies, *IEEE Geosci. Remote Sens. Lett., 3*, 130–134.

Kaercher, B., and U. Burkhardt (2008), A cirrus cloud scheme for general circulation models, *Q. J. R. Meteorol. Soc., 134*, 1439–1461.

Kahn, B. H., and J. Teixeira (2009), A global climatology of temperature and water vapor variance scaling from the Atmospheric Infrared Sounder, *J. Climate, 22*, 5558–5576.

Kahn, B. H., J. Teixeira, E. J. Fetzer, A. Gettelmann, S. M. Hristova-Veleva, X. Huang, A. K. Kochanski, M. Köhler, S. K. Krueger, R. Wood, and M. Zhao (2011), Temperature and water vapor variance scaling in global models: Comparisons to satellite and aircraft data, *J. Atmos. Sci, 68*, 2156–2168.

Keil, C., A. Röpnack, G. C. Craig, and U. Schumann (2008), Sensitivity of quantitative precipitation forecast to height dependent changes in humidity, *Geophys. Res. Lett., 35*, L09812, doi:10.1029/2008GL033657.

Bibliography

Kiemle, C., G. Ehret, A. Giez, K. J. Davis, D. H. Lenschow, and S. P. Oncley (1997), Estimation of boundary layer humidity fluxes and statistics from airborne differential absorption lidar (DIAL), *J. Geophys. Res., 102*, 29 189–29 203.

Kiemle, C. (2008), Airborne water vapor lidar measurements, *DLR-Forschungsbericht 2008-19,* DLR Oberpfaffenhofen, Germany, 94pp.

Kiemle, C., M. Wirth, A. Fix, S. Rahm, U. Corsmeier, and P. Di Girolamo (2011), Latent heat flux measurements over complex terrain by airborne water vapour and wind lidars, *Q. J. R. Meteorol. Soc., 137*, 190–203.

Kottmeier, C., N. Kalthoff, U. Corsmeier, C. Barthlott, J. Van Baelen, A. Behrendt, R. Behrendt, A. Blyth, R. Coulter, S. Crewell, P. Di Girolamo, M. Dorninger, C. Flamant, T. Foken, M. Hagen, C. Hauck, H. Hoeller, H. Konow, M. Kunz, H. Mahlke, S. D. Mobbs, E. Richard, R. Steinacker, T. Weckwerth, A. Wieser, and V. Wulfmeyer (2008), Mechanisms initiating deep convection over complex terrain during COPS. Special issue on quantitative precipitation forecasting, *Meteorol. Z., 17*, 931–948.

Kristjansson, J. E., I. Barstad, T. Aspelien, I. Fore, O. Godoy, O. Hov, E. Irvine, T. Iversen, E. Kolstad, T. E. Nordeng, H. McInnes, R. Randriamampianina, J. Reuder, O. Saetra, M. Shapiro, T. Spengler and H. Olafsson (2011), The Norwegian IPY-THORPEX: Polar lows and arctic fronts during the 2008 Andoya campaign, *Bull. Am. Meteorol. Soc., 92*, DOI:10.1175/2011BAMS2901.1.

Leblanc T., I. S. McDermid, and T. D. Walsh (2012), Ground-based water vapor raman lidar measurements up to the upper troposphere and lower stratosphere for long-term monitoring, *Atmos. Meas. Tech., 5*, doi:10.5194/amt-5-17-2012.

Lenschow D. H., V. Wulfmeyer, and C. Senff (2000), Measuring second- through fourth-order moments in noisy data, *J. Atmos. Ocean. Technol., 17*, 1330–1347.

Lewis, G. M., P. H. Austin, and M. Szczodrak (2004), Spatial statistics of marine boundary layer clouds, *J. Geophys. Res., 109*, D04104, doi:10.129/2003JD003742.

Lin, J. W.-B., and J. D. Neelin (2002), Considerations for stochastic convective parameterization, *J. Atmos. Sci., 59*, 959–975.

Bibliography

Linfield, R. P., M. M. Colavita, and B. F. Lane (2001), Atmospheric turbulence measurements with the Palomar testbed interferometer, *ApJ., 554*, doi:10.1086/321372.

Lohmann, U., N. McFarlane, L. Levkov, K. Abdella, and F. Albers (1999), Comparing different cloud schemes of a single column model by using mesoscale forcing and nudging technique, *J. Climate, 12*, 438–461.

Lomb, N. R. (1976), Least-squares frequency analysis of unequally spaced data, *Astrophys. Space Sci., 39*, 447–462.

Lovejoy, S., A. Tuck, and D. Schertzer (2010), Horizontal cascade structure of atmospheric fields determined from aircraft data, *J. Geophys. Res., 115*, D13105.

Lu, C., and S. E. Koch (2008), Interaction of upper-tropospheric turbulence and gravity waves as obtained from spectral and structure function analyses, *J. Atm. Sci., 65*, 2676–2690.

Maddy, E., and C. Barnet (2008), Vertical resolution estimates in version 5 of AIRS operational retrievals, *IEEE Trans. Geosci. Remote Sens., 46*, 2375–2384.

Maiman, T. H. (1960), Stimulated optical radiation in ruby, *Nature, 187*, 493–494.

Malkus, J. S. (1954), Some results of a trade-cumulus cloud investigation, *J. Meteorol., 11*, 220–237.

Manney, G. L., and J. L. Stanford (1990), Wavenumber spectra from temperature-humidity infrared radiometer 6.7 μm water vapor data, *J. Geophys. Res., 95*, 909–913.

Marenco, A., et al. (1998), Measurement of ozone and water vapor by Airbus in-service aircraft: The MOZAIC airborne program, An overview, *J. Geophys. Res., 103*, 25 631–25 642.

Marshak, A., A. Davis, W. Wiscombe, and R. Cahalan (1997), Scale invariance in liquid water distributions in marine stratocumulus. Part II: Multifractal properties and intermittency issues, *J. Atm. Sci., 54*, 1423–1444.

Maurellis, A., and J. Tennyson (2003), The climatic effects of water vapor, *Physics World, May 2003,* Available at http://physicsworld.com/cws/article/print/17402.

Bibliography

Murphy, D. M. (1989), Time offsets and power spectra of the ER-2 data set from the 1987 airborne Antarctic ozone experiment, *J. Gephys. Res., 94*, 16 737–16 748.

Musial, J. P., M. M. Verstraete, and N. Gobron (2011), Comparing the effectiveness of recent algorithms to fill and smooth incomplete and noisy time series, *Atmos. Chem. Phys. Discuss., 11*, 14 259–14 308, doi:10.5194/acpd.-11-14259-2011.

Nastrom, G. D., and K. S. Gage (1985), A climatology of atmospheric wavenumber spectra of wind and temperature observed by commercial aircraft, *J. Atmos. Sci., 42*, 950–960.

Nastrom, G. D., W. H. Jasperson, and K. S. Gage (1986), Horizontal spectra of atmospheric tracers measured during the global atmospheric sampling program, *J. Geophys. Res., 91*, 13 201–13 209.

Pierrehumbert, R. T. (1994), On tracer microstructure in the large-eddy dominated regime, *Chaos, Solitons and Fractals, 4*, 1091–1110.

Pierrehumbert, R. T. (1996), Anomalous scaling of high cloud variability in the tropical Pacific, *G. Phys. Res. Lett., 23*, 1095–1098.

Pierrehumbert, R. T. (1999), Subtropical water vapor as a mediator of rapid global climate change, *Mechanisms of global change at millennial time scales.,* edited by P. U. Clark, R. S. Webb and L. D. Keigwin, AGU, Washington, DC, 339–362.

Pierrehumbert, R. T., H. Brogniez, and R. Roca (2007), On the relative humidity of the atmosphere, *The Global Circulation of the Atmosphere,* T. Schneider and A. Sobel, Princeton Univ. Press, 143–185.

Plant, R. S., and G. C. Craig (2008), Parameterization for deep convetion based on equilibrium statistics, *J. Atmos. Sci., 65*, 87-105.

Poli, P., P. Moll, F. Rabier, G. Desroziers, B. Chapnik, L. Berre, S. Healy, E. Andersson, and F. El Guelai (2007), Forecast impact studies of zenith total delay data from European near real-time GPS stations in Meteo France 4DVAR, *J. Geophys, Res.,, 112*, D06114, doi:10.1029/2006JD007430.

Bibliography

Press, W. H., S. A. Teukolsky, W. T. Vetterling, and B. P. Flanery (2007), Numerical Recipes, *Third Edition,* 726–729.

Pressel, K. G., W. D. Collins, and A. R. Desai (2010), Variance scaling in water vapor measurements from a tall tower, *Extended Abstracts, 13th Conf. on Cloud Physics.*

Pressel, K. G., and W. D. Collins (2012), First-order structure function analysis of statistical scale invariance in the AIRS-observed water vapor field, *J. Climate, 25*, 5538–5555.

Raymond D. J., and D. J. Torres (1998), Fundamental moist modes of the equatorial troposphere, *J. Atmos. Sci., 55*, 1771–1790.

Rebora, N., L. Ferraris, J. von Hardenberg, and A. Provenzale (2006), RainFARM: Rainfall downscaling by a filtered autoregressive model, *J. Hydromet., 7*, 724–738.

Roberts R. D., et al. (2008), REFRACTT 2006: Real-time retrieval of high-resolution, low-level moisture fields from operational NEXRAD and research radars, *Bull. Am. Meteorol. Soc., 89*, 1535–1548.

Scargle, J. D. (1982), Studies in astronomical time series analysis. II. Statistical aspects of spectral analysis of unevenly spaced data, *Astrophys. J., 263* 835–853.

Scargle, J. D. (1989), Studies in astronomical time series analysis. III. Fourier transforms, autocorrelation functions, and cross-correlation functions of unevenly spaced data, *Astrophys. J., 343* 874–887.

Schäfler, A., A. Doernbrack, C. Kiemle, S. Rahm, and M. Wirth (2010), Tropospheric water vapor transport as determined from airborne lidar measurements, *J. Atmos. Oceanic Technol., 27*, 2017–2030.

Schäfler, A. (2011), Investigation of the warm conveyor belt inflow - a combined approach using airborne lidar observations and ECMWF model simulations, Dissertation, LMU München.

Schemann, V., B. Stevens, V. Grützun, and J. Quaas (2013), Scale dependency of total water variance, and its implication for cloud parameterizations, *J. Atmos. Sci.,* doi:10.1175/JAS-D-13-09.1, in press.

Bibliography

Schneider, T., K. L. Smith, P. A. O'Gorman, and C. C. Walker (2006), A climatology of tropospheric zonal-mean water vapor fields and fluxes in isentropic coordinates, *J. Clim., 19*, 5918–5933.

Schneider, T., P. A. O'Gorman, and X. J. Levine (2010), Water vapor and the dynamics of climate changes, *Rev. Geophys., 48*, RG3001, doi:10.1029/2009RG000302.

Schotland, R. M. (1966), Some observations of the vertical profile of water vapor by a laser optical radar, *Proc. 4th Symposium on Remote Sensing of Environment,* 12-14 April 1966, University of Michigan, Ann Arbor, 273–283.

Schotland, R. M. (1974), Errors in the lidar measurement of atmospheric gases by differential absorption, *J. Appl. Meteorol., 13*, 315–331.

Selz, T., and G. C. Craig (2013), Error growth experiments with the COSMO model, *in prep.*

Sherwood, S. C. (1996), Maintenance of the free-tropospheric tropical water vapor distribution, part I, Clear regime budget, *J. Clim., 9*, 2903–2918.

Sherwood, S. C. (1999), Convective precursors and predictability in the tropical western Pacific, *Mon. Wea. Rev., 127*, 2977–2991.

Sherwood, S. C., R. Roca, T. M. Weckwerth, and N. G. Andronova (2010), Tropospheric water vapor convection and climate, *Rev. Geophys., 48*, doi:10.1029/2009RG000301.

Shraiman, B. I., and E. D. Siggia (2000), Scalar turbulence, *Nature, 405*, 639–646.

Skamarock, W. C. (2004), Evaluating mesoscale NWP models using kinetic energy spectra, *Mon. Wea. Rev., 132*, 3019–3032.

Soden, B. J., and I. M. Held (2006), An assessment of climate feedbacks in coupled ocean-atmosphere models, *J. Clim., 19*, 3354–3360.

Stensrud, D. J. (2007), Parameterization Schemes: Keys to Understanding Numerical Weather Prediction Models, *Cambridge University Press,* Cambridge, UK.

Bibliography

Stevens, B., J. Biercamp, U. Burkhardt, S. Crewell, S. Jones, A. Macke, A. Seifert and C. Simmer (2011), HD(CP)^2: High definition clouds and precipitation for advancing climate prediction, Proposal November 7, 2011.

Stevens, B., and S. Bony (2013a), What are climate models missing?, *Science, 340*, 1053–1054, DOI:10.1126/science.1237554.

Stevens, B., and S. Bony (2013b), Water in the atmosphere, *Physics Today, 66*, 29–34, doi:10.1063/PT.3.2009.

Taylor, G. I., 1938: Statistical theory of turbulence. *Proc. Roy. Soc. London, 164*, 476–490.

Thurai, M., V. N. Bringi, Y. H. Lee, L. S. Kumar, J. D. Eastment, and D. Ladd (2011), Height-correlation analysis of data from an S-band zenith-pointing radar in Singapore, *https://ams.confex.com/ams/35Radar/webprogram/Paper191243.html*.

Tiedtke, M. (1989), A comprehensive mass flux scheme for cumulus parameterization in large-scale models, *Mon. Wea. Rev., 117*, 1779–1800.

Tjemkes, S., and M. Visser (1994), Horizontal variability of temperature, specific humidity, and cloud liquid water as derived from spaceborne observations. *J. Geophys. Res., 99*, 23 089–23 105.

Tompkins, A. M. (2002), A prognostic parameterization for the subgrid-scale variability of water vapor and clouds in large-scale models and its use to diagnose cloud cover. *J. Atmos. Sci., 59*, 1917–1942.

Tompkins, A. M. and J. Berner (2008), A stochastic convective approach to account for model uncertainty due to unresolved humidity variability. *J. Geophys. Res., 113*, D18101, doi:10.1029/2007JD009284.

Trenberth, K. E., J. Fasullo, and L. Smith (2005), Trends and variability in column-integrated atmospheric water vapor, *Climate Dynamics, 24*, 741–758.

Tuck, A. F., S. J. Hovde, E. C. Richard, D. W. Fahey, R. S. Gao, and T. P. Boy (2003), A scaling of ER-2 data in the inner Arctic vortex during January-March 2000, *J. Geophys. Res., 108*, doi:10.1029/2001JD000879.

Bibliography

Vallis, G. K., G. J. Shutts, and M. E. B. Gray (1996), Balanced mesoscale motion and stratified turbulence forced by convection, *Q. J. R. Meteorol. Soc., 123*, 1621–1652.

Wagner, J. S., A. Gohm, A. Dörnbrack, and A. Schäfler (2011), The mesoscale structure of a polar low: airborne lidar measurements and simulations, *Q. J. R. Meteorol. Soc., 137*, 1516–1531, DOI:10.1002/gj.857.

Waite, M. L., and C. Snyder (2012), Mesoscale energy spectra of moist baroclinic waves , *J. Atmos. Sci.,*, doi:10.1175/JAS-D-11-0347.1, in press.

Wakimoto R. M., and H. V. Murphey (2008), Airborne doppler radar and sounding analysis of an oceanic cold front, *Mon. Weather Rev., 136*, 1475–1491.

Wang, H., G. Feingold, R. Wood, and J. Kazil (2010), Modelling microphysical and meteorological controls on precipitation and cloud cellular structures in southeast Pacific stratocumulus. *Atmos. Chem. Phys., 10*, 6347–6362.

Warner, T. T. (2011), Numerical weather and climate prediction. *Cambridge University Press,* NEW YORK, NY, 526pp.

Webb M. J., et al. (2006), On the contribution of local feedback mechanisms to the range of climate sensitivity in two GCM ensembles, *Clim. Dyn., 27*, 17–38.

Weckwerth T. M. (2000), The effect of small-scale moisture variability on thunderstorm initiation, *Mon. Weather Rev., 128*, 4017–4030.

Werner, C. and H. Herrmann (1981), Lidar measurements of the vertical absolute humidity distribution in the boundary layer, *J. Appl. Meteorol., 20*, 476–481.

Wirth, M., A. Fix, P. Mahnke, H. Schwarzer, F. Schrandt and G. Ehret (2009), The airborne multi-wavelength water vapor differential absorption lidar WALES: System design and performance, *Appl. Phys., 96*, 201–213.

Wood, A. T. A., and G. Chan (1994), Simulation of stationary Gaussian processes in $[0,1]^d$, *J. Comp. Graph. Stat., 3*, 409–432.

Wulfmeyer, V., et al. (2011), The Convective and Orographically-induced Precipitation Study (COPS): The scientific strategy, the field phase, and research highlights, *Q. J. R. Meteorol. Soc., 137*, DOI:10.1002/qj.752.

Bibliography

Xu, Y., L. L. Fu, and R. Tulloch (2011), The global characteristics of the wavenumber spectrum of ocean surface wind, *J. Phys. Ocean., 41*, 1576–1582.

Yang, H., and R. T. Pierrehumbert (1994), Production of dry air by isentropic mixing, *Mon. Weather Rev., 134*, 209–230.

Yokohata, T., et al. (2005), Climate response to volcanic forcing: Validation of climate sensitivity of a coupled atmosphere-ocean general circulation model, *Geophys. Res. Lett., 32*, L21710, doi:10.1029/2005GL023542.

Zelinka, M. D., and D. L. Hartmann (2009), Response of humidity and clouds to tropical deep convection, *J. Clim., 22*, 2389–2404.

Zhan, Q., A. H. Manson, and C. E. Meek (1996), The impact of gaps and spectral methods on the spectral slope of the middle atmospheric wind, *J. Atmos. Terr. Phys., 58*, 1329–1336.

Zhang, G. J., and N. A. McFarlane (1995), Sensitivity of climate simulations to the parameterization of cumulus convection in the Canadian Climate Center general circulation model, *Atmos. Ocean, 33*, 407–446.

Zhang, F., C. Snyder, and R. Rotunno (2003), Effects of moist convection on mesoscale predictability, *J. Atmos. Sci., 60*, 1173–1185.

Zhang, M. (2004), Cloud-climate feedback: how much do we know?, *Observation, Theory, and Modeling of Atmospheric Variability, World Scientific Series on Meteorology of East Asia, 3*, World Scientific Publishing Co., Singapore, 632 pp.

Zhang Y., S. A. Klein, C. Liu, B. Tian, R. T. Marchand, J. M. Haynes, R. B. McCoy, Y. Zhang, and T. P. Ackerman (2008), On the diurnal cycle of deep convection, high-level cloud, and upper troposphere water vapor in the Multiscale Modeling Framework, *J. Geophys. Res., 113*, D16105, doi:10.1029/2008JD009905.

Zus F., M. Grzeschik, H. Bauer, V. Wulfmeyer, G. Dick, and M. Bender (2008), Development and optimization of the IPM MM5 GPS slant path 4DVAR system, *Meteorol. Z., 17*, 867–885.

Acknowledgement

I would like to express my deepest appreciation for Professor Dr. George C. Craig who has the attitude and the substance of a genius: he continually and convincingly conveyed a spirit of adventure in regard to research that caught up with me. My thanks are further extended to Dr. Christoph Kiemle who continously and devotedly guided me throughout the past three years in which the thesis has been developed, always encouraging me to pursue my own way and to develop my own ideas. Without the data set provided by him, this work would never have been possible. I profited largely from the situation of having two supervisors responsible with such a remarkable research experience. Both, George and Christoph, were always open for questions and spent a lot of time in discussions with me. The successful publishing of two papers during my PhD study would further have never been possible without the fervent and devoted effort by my two supervisors.

The work of this thesis was performed within the DFG research project HALO and I am thankful for the funds made available for this research project. I profited a lot from the various meetings and international scientific conferences I was enabled to participate in, specifically the exciting journey to the AGU Fall Meeting in San Francisco which was also funded by the DFG aid money.

I am also thankful to the research team working in the group of Professor George C. Craig at the Ludwig-Maximilians University in Munich, especially for the various discussions on my work during weekly group meetings and the valuable advice provided.

This work would also not yet have been finished without the support of my family. Wholehartedly, I'm thankful to my lovely wife who motivated me to continue with my research studies in times when my motivation was low. Her frequent and always well-intended encouragement to keep going and bring this to an end, has helped me to follow through.

Last but not least, I would like to thank God the creator of heaven and earth, in whom I strongly believe for seeing me through. Honour to whom honour is due.

Genesis 8, 1:

"But God remembered Noah and all the beasts and all the livestock that were with him in the ark. And God made a wind blow over the earth, and the waters subsided."